
Draft Manuscript for Review

# The interplay between melting, refertilisation and carbonatite metasomatism in off-cratonic lithospheric mantle under Zealandia: An integrated major, trace and platinum group element study

| | |
|---|---|
| Journal: | *Journal of Petrology* |
| Manuscript ID: | JPET-Aug-14-0109.R1 |
| Manuscript Type: | Original Manuscript |
| Date Submitted by the Author: | 03-Feb-2015 |
| Complete List of Authors: | McCoy-West, Alexander; Durham University, Department of Earth Sciences<br>Bennett, Victoria; The Australian National University,<br>O'Neill, Hugh; Australian National University, Research School of Earth Sciences<br>Hermann, Jörg; Research School of Earth Sciences, The Australian National University<br>Puchtel, Igor; University of Maryland, Department of Geology |
| Keyword: | mantle xenoliths, subsolidus re-equilibration, partial melting, carbonatite metasomatism, platinum group elements, New Zealand |
| | |

# The interplay between melting, refertilisation and carbonatite metasomatism in off-cratonic lithospheric mantle under Zealandia: An integrated major, trace and platinum group element study

Alex J. McCoy-West[1*], Vickie C. Bennett[1], Hugh St. C. O'Neill[1], Jörg Hermann[1] and Igor S. Puchtel[2]

[1]Research School of Earth Sciences, Australian National University, Canberra, 0200, Australia

[2]Department of Geology, University of Maryland, College Park, Maryland, 20742, USA

[*]Present address: Department of Earth Sciences, Durham University, Science Laboratories, Durham, DH1 3LE, UK

| | |
|---|---|
| Number of words: | 11,652 |
| Number of references: | 167 |
| Number of figures: | 18 |
| Number of tables: | 4 |

Corresponding author: Alex McCoy-West (a.j.mccoy-west@durham.ac.uk).

## ABSTRACT

It is widely accepted that stabilisation of the continental crust requires the presence of sub-continental lithospheric mantle. However, the degree of melt depletion required to stabilise the lithosphere and whether widespread refertilisation is a significant process remain unresolved. Here, major and trace element, including platinum group elements (PGE) characterisation of 40 mantle xenoliths from 13 localities is used to constrain the melt depletion, refertilisation and metasomatic history of lithospheric mantle underneath the micro-continent Zealandia. Our previously published Re-Os isotopic data from a subset of these xenoliths provide Phanerozoic to Paleoproterozoic ages and, reinterpreted with the new major and trace element data presented here, demonstrate that a large volume (>2 million $km^3$) of lithospheric mantle with an age of 1.99 ± 0.21 Ga is present below the much younger crust of Zealandia. A classical peritectic melting model using moderately incompatible trace elements in bulk rocks (e.g. Yb) demonstrates that these peridotites experienced a significant range of degrees of partial melting, between 3-28 %. During subsolidus equilibration clinopyroxene gains significant rare earth elements (REE) , which then leads to the underestimation of the degree of partial melting by ≤12 % in fertile xenoliths. A new approach taking into account the effects of subsolidus re-equilibration on clinopyroxene composition effectively removes discrepancies in the calculated proportion of melting and provides consistent estimates of the degree of melting between 4 % and 29 %. The estimated amount of melting is independent of the Re-Os model ages of the samples. The PGE patterns record simple melt depletion histories and the retention of primary base metal sulfides in the majority of xenoliths. A rapid decrease in $Pt/Ir_N$ observed at ca. 1.0 wt% $Al_2O_3$ is a direct result of the exhaustion of sulfide in the mantle residue at ca. 20-25% partial melting and the inability of Pt to form a stable alloy phase. Major elements preserve evidence for refertilisation by a basaltic component that resulted in the formation of secondary clinopyroxene and low-forsterite olivine. The majority of xenoliths show effects of cryptic metasomatic overprinting, ranging from minor to strong light REE enrichments in bulk rocks ($La/Yb_N$ = 0.16-15.9). Metasomatism is heterogeneous, with samples varying from those with weak REE enrichment and notable positive Sr and U-Th anomalies and negative Nb-Ta

anomalies in clinopyroxene to those that have extremely high concentrations of REE, Th-U and Nb. Chemical compositions are consistent with a carbonatitic component contributing to the metasomatism of the lithosphere under Zealandia. Notably, the intense metasomatism of the samples did not affect the PGE budget of the peridotites as this was controlled by residual sulfides.

Keywords: mantle xenoliths; partial melting; subsolidus re-equilibration; carbonatite metasomatism; platinum group elements; New Zealand.

## INTRODUCTION

The composition of newly created sub-continental lithospheric mantle (SCLM) has become progressively more fertile throughout Earth's history. This progressive reduction in the degree of melt depletion, in terms of $Al_2O_3$ contents and Mg#, is coupled with a gradual increase in the density of newly formed SCLM from the Archean (Mg# = 92.7; $\rho$ = 3.31 $Mgm^{-3}$), through to the Proterozoic (Mg# = 90.6; $\rho$ = 3.35 $Mgm^{-3}$) and Phanerozoic (Mg# = 89.9; $\rho$ = 3.36 $Mgm^{-3}$) times (Griffin *et al.*, 1998, Poudjom Djomani *et al.*, 2001). The lower density of highly refractory Archean SCLM has resulted in it being more buoyant and longer-lived, whereas younger regions of SCLM have a smaller density contrast with the convecting mantle ($\rho$ = 3.39 $Mgm^{-3}$) and are therefore more susceptible to thermal erosion and destruction (Lee *et al.*, 2011). Furthermore it has been suggested that much of the preserved SCLM is actually Archean in age, based on individual sulfide Re-Os ages (Griffin *et al.*, 2011, 2014, 2003), and that continents require this ancient SCLM to stabilise and remain buoyant (i.e. continental life raft; Carlson, 1995), with refertilisation responsible for the more fertile regions. Numerous studies of the SCLM have focussed on the ancient keels of Archean cratons (e.g. southern

Africa, Siberia; Aulbach *et al.*, 2004, Boyd *et al.*, 1997, Griffin *et al.*, 2004, Janney *et al.*, 2010, Pearson *et al.*, 2002, Pearson & Nowell, 2004, Pearson *et al.*, 1995, Walker *et al.*, 1989), whereas, the off-cratonic mantle remains more poorly studied (e.g. Handler *et al.*, 2005, Handler *et al.*, 1997, Luhr & Aranda-Gómez, 1997, Peslier *et al.*, 2002, Peslier *et al.*, 2000). The interplay between partial melting and secondary metasomatic events in these more fertile regions can provide insights into the processes that have resulted in the stabilisation of the SCLM through to the present day.

In the southwest Pacific the largely submerged continental fragment Zealandia (i.e. the broader micro-continent of New Zealand) is currently isolated from other major continental landmasses. Zealandia was conventionally considered to have been a very young region of crust, formed by multiple episodes of terrane accretion at the eastern margin of Gondwana during the Phanerozoic (ca. 520-100 Ma; Mortimer, 2004). However, Re-Os data from a regional collection of mantle xenoliths have shown that the SCLM underlying Zealandia has a complex distribution of lithosphere stabilisation ages (Re-depletion model ages range between 0 and 2.3 Ga; McCoy-West *et al.*, 2013).. In this study, we further investigate this region of Paleoproterozoic to Phanerozoic off-cratonic SCLM through a comprehensive major, trace and platinum group element (PGE) study of mantle xenoliths from 13 localities from throughout New Zealand. These data are used to discuss the thermal, melt extraction and metasomatic history of the SCLM under Zealandia, and test whether the Paleoproterozoic mantle has undergone extensive (ca. 25 %) melt depletion with subsequent refertilisation, or whether the xenoliths preserve variable amounts of primary melt depletion.

## GEOLOGICAL SETTING

Zealandia is a largely submerged (ca. 90 %), continental fragment in the southwest Pacific that covers an area of >4.5 million km$^2$(Mortimer & Campbell, 2014). New Zealand represents the major emergent part of Zealandia and is formed from a complex collage of geological terranes. Its basement geology can be divided into two major provinces (Western and Eastern; Fig. A1.1), that comprise a series of middle Cambrian-Early Cretaceous terranes that are volumetrically dominated by terrigenous sediments (Cooper & Tulloch, 1992, Mortimer, 2004). Separating the rocks of the Western and Eastern Provinces is the Median Batholith, a Carboniferous-Early Cretaceous subduction-related calc-alkaline plutonic complex that is the exposed remnants of a long-lived subduction zone at the eastern margin of Gondwana (Kimbrough *et al.*, 1994, Mortimer *et al.*, 1999).

The separation of Zealandia from Marie Byrd Land, West Antarctica, began at the tip of the Chatham Rise at ca. 84 Ma (Eagles *et al.*, 2004, Larter *et al.*, 2002), with complete separation following the opening of the Tasman Sea (ca. 85-55 Ma; Sutherland, 1995, 1999). It has subsequently drifted ca. 6000 km northwest to its present location, undergoing a significant tectonic reorganisation with the Australian-Pacific plate boundary now propagating through the centre of New Zealand. Alkaline basaltic magmatism has occurred sporadically throughout New Zealand over the last 100 Myr. The volcanic rocks are widely distributed with major volcanic centres including the Chatham Islands (85-82 Ma, 41-36 Ma, 5-0 Ma; Grindley *et al.*, 1977, Morris, 1985a, 1985b, Panter *et al.*, 2006), Dunedin harbour (13-10 Ma; Coombs *et al.*, 2008, Price *et*

*al.*, 2003, Timm *et al.*, 2010) and Banks Peninsula (11-5.8 Ma; Sewell, 1988, Sewell *et al.*, 1992, Timm *et al.*, 2009).

Until recently, studies on New Zealand mantle xenoliths focussed largely on petrography and mineral characterisation (Reay & Sipiera, 1987). In the North Island, mantle xenoliths are scarce with some reported in the young basaltic volcanoes (<2.5 Ma) of the South Auckland, Ngatutura and Alexandra Volcanic Fields (Brothers & Rodgers, 1969, Rafferty & Heming, 1979, Rodgers & Brothers, 1969, Rodgers *et al.*, 1975) and in a Miocene dyke in the Northland Volcanic Province (Black & Brothers, 1965). Peridotite xenoliths are more abundant in the South Island providing direct samples of the SCLM from basalts erupted over the past ca. 90 Myr. In the northern half of the island, isolated occurrences are found within the Cookson Volcanics in Marlborough (Reay, 1993) and sporadic dykes in Westland (Tulloch & Nathan, 1990). Further south, mantle xenoliths are more common, having been entrained in a range of small scale basaltic volcanic edifices, including the Akaoroa Volcano (McCoy-West *et al.*, 2013, Sewell *et al.*, 1993), Deborah Volcanics (Reay *et al.*, 2002), Waipiata Volcanics (Price & Green, 1972, Rae, 1990, Reay *et al.*, 1991, Scott *et al.*, 2014a, Wright, 1966), and Dunedin Volcano (Hoke *et al.*, 2000, Price *et al.*, 2003). Additionally, mantle xenoliths are also observed in the Alpine Dyke Swarm (Cooper *et al.*, 1987, Scott *et al.*, 2014b, Wallace, 1975). The South Island is underlain by a large region of SCLM that on the basis of coherent Re-Os isotope geochronology, underwent widespread melt depletion in the Paleoproterozoic (ca. 1.8-2.0 Ga; McCoy-West *et al.*, 2013; hereafter the Waitaha domain). Comprehensive characterisation of this SCLM (Scott *et al.*, 2014b) has shown regional variations in fertility, with an ultra-refractory craton-like mantle preserved beneath West Otago,

adjacent to the moderately fertile regions that comprise the Waitaha domain. All of these regions are considered to be decoupled from the younger overlying continental crust (McCoy-West et al., 2013, Scott et al., 2014b). Secondary enrichment of trace element signatures has been attributed to a carbonatitic metasomatic agent interacting with the SCLM (Scott *et al.*, 2014a, 2014b). On the offshore islands of New Zealand peridotite xenoliths have previously been reported on the Chatham (Gamble *et al.*, 1986, McCoy-West *et al.*, 2013) and Auckland Islands (Scott *et al.*, 2014b, Wright, 1968).

## XENOLITH PETROGRAPHY

### Petrography

Forty mantle xenoliths from throughout Zealandia including samples from the North, South and Chatham Islands of New Zealand (Fig. A1.1) have been characterised. All of the xenoliths were equilibrated within the spinel stability field, and were extracted from the sporadic intraplate basalts that have been erupted around Zealandia since the mid-Cretaceous (Table A1.7). Xenoliths from the Waitaha domain dominate the samples analysed here ($n$ = 27/40; Table 1); these samples are predominantly clinopyroxene (cpx)-poor lherzolites or harzburgites (ca. 6-14 cm long; Fig. 1a). Protogranular textures are dominant (e.g. Fig. 1d) with abundant large (hereafter considered to be ca. 5-8 mm) olivine (ol) and orthopyroxene (opx), variable amounts (ca. 2-11 %) of smaller interstitial cpx (1-3 mm) and rare (≤1.5 %) generally tan-light brown spinel (sp) blebs, although some large vermicular sp are observed (i.e. Fig. 1h). Subordinate xenoliths contain domains of recrystallised equigranular ol (ca. 0.5-1 mm) grains/subgrains with minor large relict pyroxenes (e.g. WFP-11; Fig. 1e). Weak kink-banding is observed in

xenoliths with large ol, and exsolution lamellae are generally thin and weak. Xenoliths from the Chatham Islands (ca. 5-8 cm across) are predominantly cpx-poor harzburgites with abundant large ol and opx, and minimal cpx (≤2-5 %). Spinels are generally red-brown blebs although rare Cr-symplectites are observed (e.g. P80180; Fig. 1g). Xenoliths from other localities are generally very small (ca. 2-4 cm) comprising either refractory cpx-devoid harzburgites dominated by large ol and opx crystals, or equigranular dunites comprising abundant ol crystals (≤2 mm) and disseminated idiomorphic spinels (i.e. Ngataura Point; Fig. 1c).

Alteration in the majority of the Zealandian xenoliths is generally very weak, with minor iron-oxyhydroxide formation along ol grain boundaries. In rare cases primary minerals have been partially replaced by talc or serpentine and magnetite (e.g. P45280). The exception are xenoliths from the Pilot Point locality that are moderately to strongly altered (e.g. Fig. 1f) due to their collection below the high-tide mark. Olivine is intensely altered to iron-oxyhydroxides ± calcite ± talc with rare fresh domains; pyroxenes and spinels are generally unaltered. Calcite crystals up to 2 cm long were observed in vugs around the edges of some xenoliths (e.g. DPP-1).

**Sulfides**

Sulfides are observed in the majority of Zealandian xenoliths; estimates of their abundances are provided in Table 2. Sulfides were absent in 13 out of 35 thin-sections although this could be purely a sampling bias, with a further 10 samples considered sulfide-poor with <20 discrete grains (≥3 μm). Distinguishing primary magmatic sulfides is difficult due to widespread cracks in ol and the rarity of sulfides enclosed within Cr-spinel. Ten samples include at least one large (≥40 μm) subhedral to euhedral sulfide

grain and several contain numerous large sulfides 60-100 μm across (e.g. WTL-1 & 3 and WFP-2 & 8), which are composed predominantly of pentlandite but may also contain chalcopyrite and/or pyrrhotite, that are possibly of primary origin (e.g. Fig. 2a). However, the majority of sulfides are secondary and occur as groups of small (<20 μm) subhedral blebs that are aligned in fractures, veinlets or recrystallised cracks (Fig. 2b). Two samples contain abundant secondary sulfides (>500 grains; Table 2), sample MSI79C contains large domains of recrystallised olivine which are sulfide-rich (Fig. 2c), while sample P43153b contains abundant fine <10 μm sulfides associated with chlorite altered cracks within the olivine matrix (Fig. 2d).

**Chemical Classification**

Based on the classification system of Le Bas & Streckeisen (1991) and using the calculated modal compositions supplemented with petrographic observations (Table 1), the 40 New Zealand mantle xenoliths studied here can be classified as: harzburgite ($n$ = 23); lherzolite ($n$ =12); dunite ($n$ = 2); olivine websterite ($n$ = 2); and wehrlite ($n$ = 1) (Fig. A1.2). The majority of Zealandian xenoliths are significantly depleted in clinopyroxene compared with the inferred composition of the fertile mantle (i.e. Ionov, 2007). The olivine websterites (MSI79C & DPP-6) are small xenoliths and their modal compositions are not consistent with standard melting processes in the lithospheric mantle, thus they will be distinguished henceforth. Variability within the samples is correlated with their location. Samples from the North Island ($n$ = 2) are highly refractory ol dominated xenoliths (Figs. 1c & A1.2), while those from the Chatham Islands are predominantly harzburgites ($n$ = 5/6). The Waitaha domain preserves the largest

compositional variability and is the only region where relatively fertile ($Al_2O_3$ >2 wt %) samples are observed.

## MINERAL CHEMISTRY

Due to the homogeneity of phases within mantle xenoliths (i.e. generally no zoning and limited variability between crystals), mineral compositions are reported as averages of typically 8-14 core analyses of individual minerals ($n$ = 40; Table 1).

### Major and minor element variability

*Olivine and Spinel*

Electron probe micro-analysis (EPMA) data indicate that ol is homogeneous in the majority of New Zealand mantle xenoliths with variations in forsterite [Fo = 100 x atomic Mg/(Mg +Fe)] content in multiple analyses of the different grains often less than the long-term standard reproducibility (San Carlos olivine: Fo = ± 0.08 %; 1σ). Based on this reproducibility, ol is here considered heterogeneous on >10 grains when Fo variation is >± 0.15 %, as seen in 14 out of 40 Zealandian xenoliths (Table 1; Fig. 3b). However, within the larger xenoliths of the Waitaha domain ol compositions are generally homogeneous ($n$ = 22/27; i.e. only ca. 18 % of samples have heterogeneous ol). Forsterite content in ol in the majority of xenoliths is negatively correlated with MnO (Fo = 89.4-92.2; MnO = 0.146-0.108 wt %; Fig. 3c) and positively correlated with NiO (not shown).

The Cr# [Cr# = atomic Cr/(Cr +Al)] of sp ranges from 0.11 in the most fertile xenoliths to 0.82 in the most refractory dunites and is positively correlated with Fo (Fig. 3a), consistent with partial melting relationships in residual peridotites (e.g. Dick & Bullen, 1984, Hellebrand *et al.*, 2001). New Zealand xenoliths plot exclusively in the off-

craton peridotite field (Ionov, 2005), with lower Fo at a given Cr# than samples from the cratonic mantle and overlap the variability observed in abyssal peridotites (Fig. 3a). Although, within an individual xenolith, Cr# can vary significantly with 7 samples having highly variable (>± 0.05) Cr# (i.e. Fig. 3b; Table 1) and a further 9 are considered to be heterogeneous (i.e. Cr# variation >± 0.03). Mantle sp typically contains <0.2 wt % $TiO_2$, but in almost all cases have <0.5 wt % $TiO_2$, and are expected to have lower $TiO_2$ and higher $Fe^{3+}$contents than their basaltic equivalents (e.g. Kamenetsky *et al.*, 2001). All samples from the Waitaha domain contain mantle sp with low $TiO_2$ (i.e. <0.25 wt %; Table 2). However, some spinels analysed herein contain up to 2-7.8 wt % $TiO_2$, with 6 samples (4 Chatham Islands and 2 Cookson xenoliths) containing spinel with >0.5 wt % $TiO_2$. An example, sample P80354a contains two types of spinel: (1) low-Ti mantle spinel (Cr# = 45; $TiO_2$ = 0.1 wt % and $Fe^{3+}/\sum Fe$ = 0.16) and (2) high-Ti spinel (Cr# = 55-60; $TiO_2$ = 0.8-2.3wt % and $Fe^{3+}/\sum Fe$ = 0.26-0.30). High $TiO_2$ grains generally comprise <50 % of the analysed spinels and are not considered representative of the mantle so are excluded from average compositions. These variable $TiO_2$ contents are considered an artefact of magnetite alteration (consistent with the petrography) either at the surface or through basalt infiltration, as Ti has been shown to partition more strongly into spinels with higher magnetite contents (Barnes & Roeder, 2001). Several Chatham Islands samples still have a significant range in Cr# at a near constant $TiO_2$ (e.g. P80354c: Cr# = 0.28-0.61; $TiO_2$ = 0.24-0.37wt %) and these samples also possess heterogeneous ol compositions.

*Clinopyroxene and Orthopyroxene*

The $Al_2O_3$ content of cpx in Zealandian xenoliths ranges from 1.8-7.2 wt %, and is negatively correlated with Fo (Fig. 3d), except for two samples (NGB-3 & WRR-6) with low Fo <90 % and extremely low $Al_2O_3$ <0.7 wt % that diverge from this trend. All cpx in Zealandian xenoliths can be considered low $Na_2O$ (<2 wt %; Fig. 4) and within the range of abyssal peridotites consistent with the majority of mantle xenoliths worldwide. The majority of samples are consistent with a simple melt depletion trend (i.e. Hellebrand *et al.*, 2001), with $Na_2O$ decreasing from 1.8-0.2 wt % as $TiO_2$ reduces from 0.54-0.01wt % and $Cr_2O_3$ (0.5-1.3 wt %) remains within the range of the cratonic mantle (Fig. 4a-b). Several samples diverge from this melting trend with $TiO_2$ >0.6 wt % or $Cr_2O_3$ >1.5 wt % (e.g. MSIK33C; Fig. 4) and are probably affected by a secondary process. A progressive increase in $TiO_2$ (0.01-0.67 wt %) is observed in a subset of five Chatham Islands samples at near constant $Na_2O$ (ca. 0.75 wt %). Orthopyroxene Mg# varies from 0.887-0.928 and is positively correlated with Fo ($r^2$ =0.88), whereas $Al_2O_3$ varies from 0.77-5.21 wt % and is negatively correlated with Fo (not shown).

*Sulfides*

A selection of representative mantle sulfides were analysed from 8 xenoliths (E-App 2), with element distribution maps also obtained on several multi-phase sulfides (Fig. 2). Low temperature (<300 ºC) subsolidus exsolution of sulfide melt (Durazzo & Taylor, 1982, Eggler & Lorand, 1993, Szabó & Bodnar, 1995) has resulted in sulfides that consist of an assemblage of predominantly pentlandite and chalcopyrite with some grains containing minor bornite, pyrrhotite or magnetite (Fig. 2e-l). Other sulfide phases comprise sulfides with variable Ni:Fe:Cu ratios.

**Pyroxene trace element chemistry**

Despite being a strong function of temperature (Herzberg, 1978), $Al_2O_3$ in cpx can be used as an indicator of melt depletion because of its correlation with Fo (Fig. 3d). Compatible elements (Fig. 4c) are weakly negatively correlated with $Al_2O_3$, whereas moderately incompatible elements Yb and Dy are both positively correlated with $Al_2O_3$ ($r^2 = 0.93$ and 0.91, respectively, for samples from the Waitaha domain; Fig. 4d-e). All cpx in Zealandian xenoliths have Yb and Dy contents equal to or less than the primitive mantle (PM; throughout this work based on the values of Palme & O'Neill, 2003) within error, except some Chatham Islands samples (e.g. P80180) that have elevated Yb and Dy contents at low $Al_2O_3$ (ca. 2.5-3.0 wt %). Highly incompatible elements (i.e. Ce and Th) show a significantly greater dispersion with no specific correlation with $Al_2O_3$ and concentrations up to an order of magnitude greater than that of the PM (e.g. Fig. 6f; P80290).

Clinopyroxene varies from being light rare earth element (LREE) depleted with flat middle (M) -heavy (H) REE patterns (e.g. OU45852; Fig. 5a-b; Table 2) to being variously re-enriched in the LREE to MREE (e.g. La-Er; Fig. 5c-e), to samples with elevated, but curved over, LREE (i.e. La < Ce) and gently sloping MREE to HREE (i.e. Sm-Lu; Fig. 5f; P80180). REE patterns are generally anchored around the HREE end, with Yb concentrations varying from ca. 0.3-12 times that of the PM, whereas Ce is widely variable within cpx ($Ce_{PM}$ = 0.02-58). Clinopyroxene from fertile samples is commonly depleted in Sr, Zr and Ti (e.g. OU45852; Fig. 5g), with only negligible to weak enrichment in large ion lithophile elements (LILE: i.e. Th $\leq 1_{PM}$; Fig. 5h). Samples that have enrichment of LREE (i.e. $Ce_{PM} > Yb_{PM}$) are variably elevated in LILE (e.g. Th,

U and Sr) often showing strong positive anomalies (i.e. WRR-1; Fig. 5j) but remain relatively depleted in high field strength elements (HFSE; e.g. Nb, Ta and Ti). Clinopyroxene is consistently depleted in Pb relative to other elements of similar compatibility. Coexisting opx displays a similar pattern at lower concentrations being the most enriched in Th and U (Fig. 5l).

## WHOLE ROCK CHEMISTRY

### Major element chemistry

The xenoliths studied here have experienced only minor surficial weathering and are essentially unaltered, with loss on ignitions of <1.0 wt % (Table 3). The exception being samples from the Pilot Point locality that due to interaction with seawater have undergone significant alteration, and therefore their whole rock compositions should be treated with caution (see E-App 1 for further discussion). New Zealand xenoliths have whole-rock compositions (Table 3) that are consistently more depleted than PM estimates (Palme & O'Neill, 2003), with the observed variability generally consistent with that observed in upper mantle peridotites (Fig. 6). For example, they fall within the range of compositions seen in the weakly metasomatised, variably melt depleted Horoman peridotite, Japan (Takazawa *et al.*, 2000) and a suite of clinopyroxene-rich, unmetasomatised spinel lherzolite xenoliths from Mongolia (Ionov, 2007, Ionov & Hofmann, 2007). The $Al_2O_3$ contents vary from <0.1-4.1 wt %, although the majority of samples ($n$ = 30/38) have <2 wt % $Al_2O_3$. Only four samples are considered fertile (MgO <40 wt %; CaO, $Al_2O_3$ >3 wt %); a further nine are classified as moderately depleted ($Al_2O_3$ = 1.5-3.0 wt %), consistent with a majority of basalt-derived xenoliths worldwide

(Pearson *et al.*, 2003); the remaining 24 samples are refractory xenoliths ($Al_2O_3$ <1.5 wt %). Plots of $Al_2O_3$ (an index of melt depletion) versus other major elements show the following trends with decreasing $Al_2O_3$ (Fig. 6): 1) increasing MgO and decreasing CaO for all samples; 2) FeO is relatively constant and scatters around 8 wt %, although at <1 wt % $Al_2O_3$ higher FeO contents occur; 3) $TiO_2$ contents decrease rapidly at >2 wt % $Al_2O_3$, then more slowly although samples with $TiO_2$ greater than the ambient mantle become more common; 4) MnO and $Cr_2O_3$ contents are within the range of the PM (not shown), until <1 wt % $Al_2O_3$ where more variability is observed.

The Paleoproterozoic Waitaha domain completely encompasses the variation observed within the New Zealand mantle, although fertile compositions are still limited. The most fertile samples are from the Pilot Point locality, although as noted, the compositions of some of these xenoliths (Fig. 6; white circles; CaO >4.0 wt %) are considered unreliable due to calcite infiltration. Other New Zealand xenoliths are all depleted (<2 wt % $Al_2O_3$), but show variable enrichments in FeO coupled with depletions in MgO (i.e. P45280; Fig. 6c). Samples from the Chatham Islands have strongly depleted and restricted major element compositions (i.e. $Al_2O_3$ = 0.51-0.78 wt %; MgO = 45.2-46.8 wt %).

**Trace element chemistry**

*Bivariate MgO vs. trace element diagrams*

On chondrite-normalised (Palme & O'Neill, 2003) plots weakly incompatible elements (Al, Ca and Sc) are negatively correlated with MgO and generally lie within the variability of undisturbed melting residues (e.g. Horoman peridotite: Fig. 7). Moderately incompatible REE (i.e. Yb and Dy) are also weakly negatively correlated with MgO (Fig.

7d-e), with the majority of samples falling in or below the Horoman field, except for a few xenoliths from the Chatham Islands. However, highly incompatible lithophile elements (i.e. Sm and Th) show variable systematics relative to MgO contents (Fig. 7f-i). Samarium and Nb are generally within the Horoman field and at lower concentrations than the depleted MORB mantle (Workman & Hart, 2005); the exceptions are some samples from the Waitaha domain and Chaham Islands, whereas, Th and Zr are significantly enriched above values in Horoman peridotite in the majority of samples, with several samples even having concentrations greater than those of the PM (Fig. 7i).

*Multi-element diagrams*

On PM-normalised (Palme & O'Neill, 2003) REE plots samples generally have flat MREE-HREE patterns with variable levels of depletion relative to the PM (i.e. FvF-1; WTL-2; Fig. 8c, e) and are also variable enriched in LREE (i.e. $La/Yb_N$ = 0.16-15.9; N = chondrite normalised). However, xenoliths from the Chatham Islands (i.e. Ohira Bay; Fig. 8g) possess progressively increasing concentrations of HREE to LREE. Samples from the Waitaha domain commonly exhibit positive Th-U and negative Nb-Ta anomalies on multi-element diagrams (Fig. 8).

**Highly siderophile element chemistry**

Total PGE concentrations of Zealandianxenoliths vary between 1.4 and 33 ppb (*n* = 27; Table 3). The majority of samples have Iridium-Group PGE (I-PGE: Os, Ir, and Ru; Barnes *et al.*, 1985) contents comparable to estimates of the PM (Becker et al. 2006; n = 19; Fig. 9). Osmium concentrations range from 1-7 ppb (Table 3), with Ir and Ru showing similar concentration ranges and all three elements are positively correlated ($r^2_{(Os/Ir)}$ = 0.90: Fig. 10a; $r^2_{(Ru/Ir)}$ = 0.80: not shown). Samples with the lowest Os

concentrations (<1 ppb) show positive Ru anomalies on PM-normalised diagrams, often coupled with enrichments of Re over Pd (e.g. P43153b; Fig. 9b). The majority of New Zealand xenoliths, especially those within the Waitaha domain, show variable depletions in the P-PGE (Palladium-Group PGE; Pt, Pd) and Re relative to I-PGE (Fig. 9). Pt concentrations vary from <0.1 to 12 ppb and are also well correlated with Ir for the majority of xenoliths ($r^2_{(Pt/Ir)} = 0.83$; Fig. 10b). Whereas, Pd contents vary from 0.01-9.1 ppb, with Re having a more restricted range of 0.006-0.266 ppb and dropping rapidly with decreasing Ir content (Fig. 10c). Although individual PGE (e.g. Ir, Pd) are weakly correlated with indices of melt depletion (e.g. $Al_2O_3$; not shown), the $Pt/Ir_N$ ratio shows a much tighter correlation, gradually decreasing until ca. 1.0 wt % $Al_2O_3$ and then dropping rapidly (Fig. 10e). Samples from Ngatutura Point have unique PGE patterns with anomalously high Pt/Ir (Fig. 9a).

## THERMOBAROMETRY

Sharp boundaries between xenoliths and the host basalt indicate that the xenoliths were transported rapidly to the surface (Fig. 1). The near 1:1 correlation between Mg# in whole rock and Fo in ol in Zealandian xenoliths (Fig. 11a) and the homogeneity of minerals within the xenoliths, especially from the Waitaha domain ($n$ = 22/27; Table 1), is compelling evidence for chemical equilibrium at a specific set of temperature conditions.

### Equilibration Temperatures

Numerous types of geothermometers have been proposed for calculating the equilibration temperatures of spinel bearing peridotites (e.g. Ballhaus *et al.*, 1991, Brey & Köhler,

1990, De Hoog *et al.*, 2010, Köhler & Brey, 1990, Taylor, 1998, Wells, 1977). Unfortunately, however, there is no precise way of calculating pressures in spinel peridotites (the sole garnet-free geobarometer proposed by Köhler & Brey (1990) produces highly erratic results; see Witt-Eickschen & O'Neill (2005)). Equilibration pressures are only constrained mineralogically to within the spinel stability field (0.8-1.8 GPa; O'Neill, 1981). In this study temperatures have been calculated assuming a pressure of 1.3 GPa, with the reported errors due to the uncertainty of the samples position within the stability field of spinel.

Equilibration temperatures for New Zealand xenoliths are calculated using five different geothermometers (Table A1.1) and range from 750-1060 ºC using Taylor (1998; here after TA98), whereas the Ca-in-orthopyroxene thermometer of Brey and Kohler (1990; here after $BKN_{Opx}$) produces a more restricted temperature range of 830-1020 ºC ($n$ = 39; Fig. 12). Calculated temperatures using thermometers incorporating cpx information (i.e. TA98) that are ≤ 800 ºC are unreliable because with decreasing temperature these geothermometers become increasingly reliant on small variations of CaO in the context of large total CaO contents. Thus, due to the low temperature of the xenoliths in this study, and for internal consistency, $BKN_{Opx}$ temperatures are preferred. Temperatures calculated for harzburgites using $BKN_{Opx}$ are minimum estimates, as CaO is not buffered by cpx, although they generally agree well with temperatures calculated by the Al in ol thermometer of De Hoog *et al.* (2010; see Fig. A1.7) . Within an individual xenolith locality equilibration temperatures are generally reproducible within ± 30 ºC (1σ; Fig. 12). Within the Waitaha domain, three localities (Trig L, Ram Rock and Fortification Peak) have average temperatures of ca. 870-900 ºC, while the nearby (<65 km) Pilot

Point locality is 100 ºC hotter with an average temperature of 1000 ± 30 ºC. This stratification of average temperatures between two proximate localities (<12 km) is also observed on the Chatham Islands and suggests that xenoliths are being sampled from the entire depth range of the spinel-facies SCLM. Calculated $BKN_{Opx}$ temperatures are positively correlated with the concentrations of CaO and $Cr_2O_3$ in ol (Fig. 11b) that are known to be sensitive to temperature (Ionov, 2007, Köhler & Brey, 1990).

**Oxygen fugacity**

Oxygen fugacities relative to the FMQ (fayalite-magnetite-quartz) buffer were calculated using the ol-opx-sp barometer of O'Neill & Wall (1987), updated by replacing the Gibbs free energy of the reaction $Mg_2SiO_4 + SiO_2 = Mg_2Si_2O_6$ (needed for the calculation of the activity of $SiO_2$) with the data from Holland & Powell (1998). A pressure of 1.3 GPa was assumed, and sp compositions were calculated by averaging analyses of 8 to12 grains in each xenolith. The calculated $fO_2$ depends on the $Fe^{3+}$ content of sp, which was determined from EPMA data by stoichiometry. The typical precision of routine EPMA for major elements in sp propagates to a standard deviation of ±0.025 in $Fe^{3+}/\sum Fe$ (see Canil & O'Neill, 1996; herein Table A1.1 ≤ 0.02). This precision, which is similar to that from determinations of $Fe^{3+}/\sum Fe$ by Mössbauer spectroscopy (Canil & O'Neill, 1996, Wood & Virgo, 1989), is due to non-systematic analytical uncertainties (e.g. counting statistics) and does not depend on the standards used. Analytical accuracy, which depends on the standards and correction procedures, may produce systematic errors in $Fe^{3+}/\sum Fe$ determined by stoichiometry (Wood and Virgo 1989). To check for this, four standard spinels from the study of Wood and Virgo (1989), KLB 8311, KLB 8316, KLB 8320 and SC8803B, covering $Cr_2O_3$ contents from 8.6 to 43.8 wt %, were analysed. We found no

systematic effects, and the root mean square difference between $Fe^{3+}/\sum Fe$ calculated by stoichiometry from EPMA data and that given by Wood and Virgo (1989) from Mössbauer spectroscopy was 0.025, which is concordant with expectations from the combined uncertainties of the two methods. An additional simple check for systematic errors is to examine the analytical totals of the sp after calculation of $Fe^{3+}$. Here no correlation is observed between the analytical totals, Cr# or $Fe^{3+}/\sum Fe$ (Fig. A1.11), precluding the possibility of systematic errors biasing the calculation of $Fe^{3+}/\sum Fe$ by more than a few percent. The uncertainty in calculated $Fe^{3+}/\sum Fe$ translates into an uncertainty in calculated $\Delta \log fO_2$ which varies greatly with the value of $Fe^{3+}/\sum Fe$, becoming infinite as $Fe^{3+}/\sum Fe$ approaches 0, hence $fO_2$ calculated from sp with low $Fe^{3+}/\sum Fe$ are indicative only. This problem is minimal in this study, where all analysed sp have reasonably high $Fe^{3+}/\sum Fe$ (0.08 to 0.22; Table A1.1), except for two samples with $Fe^{3+}/\sum Fe \leq 0.04$ (MSIK33C and WRR-6). Comparison with the oxybarometer of Ballhaus *et al.* (1991) shows that there is a systematic offset between these formulations that is negatively correlated with the Cr# of sp, although the two formulations generally agree within ±0.5 log units (Fig. A1.12).

New Zealand xenoliths generally reflect reducing conditions relative to the FMQ buffer with ΔFMQ varying from -4.7 to 0.1 (Table A1.1). Within the better constrained Waitaha domain values vary from -2.6 to -0.2 and are weakly negatively correlated with Cr# of spinel (Fig. 13a), and cluster around ΔFMQ -1 (Fig. 13b), consistent with other observations in the shallow cratonic mantle and abyssal peridotites worldwide (Bryndzia & Wood, 1990, Frost & McCammon, 2008, Woodland & Koch, 2003). Three xenoliths from Ram Rock have ΔFMQ <-1.8 consistent with more reducing conditions being

present at this locality, than the majority of the Waitaha domain. Xenoliths from the Chatham Islands are slightly more oxidized (ΔFMQ = -0.6 to 0.1) than those from the Waitaha domain, especially at similar degrees of melt extraction (Fig. 13), a conclusion that would not be affected by any systematic error in the determination of $Fe^{3+}/\sum Fe$ in sp.

## DISCUSSION

### Quantifying the effects of secondary disturbance on xenolith compositions

Prior to making any inferences about the petrogenetic history of these xenoliths based on bulk rock analyses, we first assess the effects of possible late-stage processes on their trace element signatures. In garnet-free peridotites, cpx becomes the major host (>90-95 %) of the majority of incompatible trace elements (Bedini & Bodinier, 1999, Eggins *et al.*, 1998). Using the whole rock and cpx trace element data and calculated modal compositions, it is possible to undertake simple mass balance calculations to assess whether the cpx composition is consistent with the whole rock composition (Fig. A1.3). Two external agents may be responsible for modifying the composition of a xenolith once it is removed from the SCLM: 1) the addition of small volumes of basaltic magma during their entrainment, transport to the surface and eruption; and/or 2) grain boundary alteration during surficial weathering.

To quantify the maximum amount of basalt infiltration that any given sample may have experienced, basalt was added until any element was present in a greater amount than required to balance the whole rock budget (e.g. Sr in WFP-11; Fig. A1.3). In the nominally least metasomatised sample (i.e. OU45852), the MREE-HREE in cpx balance

the whole rock contents although a very small amount of basalt (<0.02 %) is required to increase the majority of highly incompatible elements to their whole rock concentrations. However, this does not sufficiently increase the large ion lithophile element (LILE: U, Ba, Sr) concentrations to those observed in the whole rock, thus a significant proportion (>80 %) of these elements probably came from alteration. In some samples the bulk rock compositions (apart from HREE) are so poorly balanced (Fig. A1.3) that they cannot be used to constrain any metasomatic processes. Bulk rock compositions can only be used for modelling if they actually reflect primary peridotite compositions, which is not always the case (e.g. common metasomatic indices such as Zr/Hf do not balance), and therefore in this instance cpx compositions are better for assessing metasomatic signatures.

**Major element evidence for cryptic refertilisation**

The observation of secondary hydrous phases (i.e. phlogopite, pargasite, apatite) in the SCLM is generally interpreted as evidence for secondary refertilisation of mantle peridotite (Bodinier *et al.*, 1988, Ionov & Hofmann, 1995, Yaxley *et al.*, 1991). Although, no such secondary phases have been found directly during this study. In mantle peridotites the concentration of $Al_2O_3$ is considered to be a robust indicator of partial melting, because it is moderately incompatible during mantle melting irrespective of the depth (Herzberg, 2004, Walter, 2003), and is also generally immobile during secondary alteration processes. The majority of New Zealand xenoliths plot near experimental derived polybaric melting trends at shallow depths (1 GPa; Herzberg, 2004) and within the Horoman peridotite field on an MgO-$Al_2O_3$ plot (Fig. 6a). In contrast,

several samples appear to be slightly enriched in CaO (Fig. 6b) at a given $Al_2O_3$ content, compared to the primary melt depletion trend observed within the Horoman peridotite. The elevated CaO and lower Fo in sample NGB-3 compared with NGB-4 at their very low $Al_2O_3$ contents ($Al_2O_3$ <0.16 wt %: CaO = 1.88 vs. 0.23 wt %; Fo = 89.7 vs. 92.2), is consistent with the cpx in this dunite being secondary. For peridotites, this distinction becomes clearer when plotting bulk rock atomic Ca/Al versus MgO (Fig. 14). Ionov & Hofmann (2007) reported gradually increasing Ca/Al from the PM value (Ca/Al = 1.1; Palme & O'Neill, 2003) up to ca. 1.3 with progressive melt depletion in fertile Mongolian xenoliths with >2.0 wt % $Al_2O_3$. Thus, here we conservatively consider samples with Ca/Al >1.5 to have been refertilised resulting in formation of secondary cpx (e.g. Ionov *et al.*, 2005). The refractory xenoliths from the Chatham Islands clearly exhibit the effect of variable addition of secondary cpx ($Al_2O_3$ = 0.51-0.78 wt %; Ca/Al = 1.28-2.34; Fig. 14; Table 3).

Numerous studies have documented Fe-enrichments in refractory peridotites with FeO contents up to 10-15 wt % (e.g. Bodinier & Godard, 2003, Boyd *et al.*, 1997, Ionov *et al.*, 2005). Experimental data have shown that FeO contents >9 wt % are inconsistent with undisturbed melting residues of the fertile mantle (FeO ca. 8.5 wt %) at any pressure (e.g. Herzberg, 2004, Walter, 2003). New Zealand xenoliths have a large range in FeO contents from 7.2-11.8 wt %, with the refractory other New Zealand xenoliths showing the strongest Fe-enrichments relative to pristine melting residues (Fig. 6). Several of these xenoliths have coupled Fe-enrichments in oland whole rock (e.g. P45280; Fig. 3 & 6c), consistent with the infiltration of a 'basaltic' melt into these olivine-rich rocks, which have enhanced permeability due to pyroxene removal (Bodinier *et al.*, 1988). Similarly,

the elevated $Na_2O$ contents (up to 0.41 wt %; Fig A1.4) observed in some of the more refractory xenoliths are compatible with global basaltic refertilisation trends (Lee *et al.*, 2011). An additional test to distinguish secondary processes in mantle xenoliths are $TiO_2$ contents, which commonly shows strong enrichments in metasomatised Fe-rich rocks (e.g. Bodinier & Godard, 2003, Ionov & Hofmann, 2007, Menzies *et al.*, 1987). $TiO_2$ contents in Zealandian xenoliths vary from 0.02-0.16 wt %, with several depleted samples showing large enrichments of $TiO_2$ above the ambient mantle trend at a given $Al_2O_3$ content (e.g. P80354c, MSIK33C; Fig. 6d). Major element evidence suggests the majority of Zealandian xenoliths ($n$ = 26/38) have experienced refertilisation by a basaltic melt leading to the formation of secondary cpx and/or Fe-rich ol.

**Characterising the pervasive metasomatism under Zealandia**

Trace elements can provide more subtle clues as to the extent and exact nature of the metasomatic agents (melts or fluids) percolating through the SCLM and modifying its composition. Due to the likelihood that the bulk rock trace element budgets may have been disturbed by secondary processes, we use cpx compositions to fingerprint this metasomatic signature. However, due to the extensive subsolidus re-equilibration observed in the Zealandian SCLM (i.e. two-pyroxene temperatures <900 °C) it is not possible to directly calculate the composition of the melt that was in equilibrium with this cpx (see modelling below).

Clinopyroxene REE patterns are consistent with all samples (except OU45852; see Figs. 5) having interacted with a metasomatic agent that has introduced at least some LREE. Cpx multi-element patterns are also highly variably (Fig. A1.8) with order of

magnitude variations in the concentrations of LILE, HFSE and REE within the cpx from different xenoliths (e.g. Th, Nb and La, respectively; Fig. 15). Three main types of cpx patterns can be recognised, from least to most metasomatised: 1) largely unmetasomatised samples with only subtle inflections in cpx REE patterns up to Nd ($n$ = 6; Fig. 5d-e); 2) weakly to moderately metasomatised samples with moderate to strong inflections in cpx REE patterns up to Ho ($n$ = 29). This type includes the majority of samples and they typically exhibit positive Th-U and Sr anomalies and Nb-Ta deficits on multi-element diagrams (e.g. WFP-1; Fig. 5). Sample WRR-1 forms a unique end member of this type with only weak REE enrichment, but a strong Th enrichment at a low Nb concentration (Figs. 5m & 15); and 3) intensely metasomatised samples ($n$ = 5) with extremely MREE-LREE enriched whole rock REE patterns with inflections occurring up to Yb (Fig. 8). Clinopyroxenes exhibit negative Sr anomalies and concave LREE patterns and continuously decreasing HREE (e.g. P80180; Fig. 5i), indicative of complete re-equilibration with the metasomatic agent. The strength of metasomatism in the SCLM has been shown to be proportional to distance from the metasomatic equilibration front (Ionov *et al.*, 2002), thus the Zealandian samples represent a gradation from cryptically metasomatised peridotites in close proximity to the cross-cutting magmatic dykes or veins to weakly metasomatised peridotites occurring in more distal regions. The extreme metasomatism preserved in the Chatham Island xenoliths (Fig. 5) is consistent with them having the highest $fO_2$ in the Zealandian SCLM (Fig. 13) as depleted peridotites like these require only small amounts of $Fe_2O_3$ to raise their $fO_2$ (Frost & McCammon, 2008, Woodland *et al.*, 2006). In some cases this metasomatism

must have occurred shortly before entrainment (e.g. DPP-1; Fig. A1.7) because cpx crystals display LREE disequilibrium between grains within a single xenolith. Carbonatite melts are considered to be effective metasomatic agents because of their low viscosity (Dawson et al., 1990), high and variable trace element contents (Nelson et al., 1988) and ability to efficiently transport LILE and REE and fractionate them from HFSE (Green & Wallace, 1988, Rudnick *et al.*, 1993, Yaxley *et al.*, 1991).The metasomatised xenoliths analysed herein contain cpx with variably fractionated Nb/Ta and to a lesser extent Zr/Hf (Fig. 5l-o) and often positive Sr anomalies and strong enrichments of Th and U over Nb. The fractionation of elements with similar incompatibility and behaviour is inconsistent with small degree silicate melts in the SCLM (see Fig. 8), but rather requires interaction with carbonatite melt. . Higher partition coefficients for Ta (relative to Nb) are expected for silicates in equilibrium with carbonatite melt fractionating the Nb/Ta ratio of the carbonatite relative to the PM (Green et al., 1992, Sweeney et al., 1992). Similar characteristics are seen in other xenolith suites worldwide assumed to have undergone carbonatite infiltration (e.g. Ionov *et al.*, 1993, Yaxley *et al.*, 1998). These observations are in accord with those of Scott *et al.* (2014a, 2014b) where carbonatite metasomatism was recognised in the SCLM beneath the South Island, largely on the basis of the low Ti/Eu of cpx and the rare occurrence of apatite at one modally metasomatised locality (Kattothyrst) within the Waitaha domain. In addition, there is direct evidence of carbonatitic magmas interacting with the SCLM in this region with calciocarbonatites observed within the Alpine Dyke swarm in the Southern Alps (Barreiro & Cooper, 1987, Cooper & Paterson, 2008). To summarise, the strong enrichments in REE, Th-U and

fractionations of Nb/Ta and Ti/Eu in cpx from Zealandian xenoliths requires that metasomatism was generated at least in part by interaction with a carbonatite melt.

To explain the unusual end-member sample WRR-1 (Fig. 15), with relatively low REE in cpx but extreme Th/Nb (Fig. 5m) requires a more complicated history. Clinopyroxenes within this xenolith have elevated Ti/Eu (≤22,000; Fig. 15) relative to the PM ($Ti/Eu_{cpx}$ = 3,980) but at very low absolute Ti concentrations (<320 ppm), requiring this xenolith to be the result of interaction with a carbonatitic melt that had already undergone apatite fractionation. Experimental studies show that the MREE are extremely compatible in apatite ($D^{ap/melt}$ >0.4-4), but will not take up significant Th and U ($D^{ap/melt}$ <0.15 and 0.01)(Klemme & Dalpé, 2003, Watson & Green, 1981); resulting in a metasomatic agent still strongly enriched in Th and U but strong depleted in the REE.

**Determining the degree of melt depletion under Zealandia and comparison of various melting models**

This discussion will comprise three parts: 1) the construction of a classical model for the peritectic melting of a residual peridotite; 2) examination of the effects of sub-solidus redistribution of REE in clinopyroxene and the how this effects apparent degrees of melt depletion; and 3) comparisons with exiting models and recommendations for future use.

*Modelling of peritectic melting in residual peridotites*

Trace element compositions are sensitive indicators of the amount of melt that has been extracted from residual peridotites, however, it is important that the effects of any metasomatism are properly considered. As previously discussed metasomatism only

causes significant enrichment of LREE in the majority of xenoliths, whereas, HREE (e.g. Er toLu; Fig. 8) should provide robust estimates of the amounts of partial melting.

A peritectic melting model based on the equations of Shaw (1970) was used to quantify the amount of partial melting that has occurred in the spinel facies mantle under Zealandia ( see Table 4). With this model, Yb concentrations measured during whole-rock analyses can be used to calculate the amount of partial melting a sample has undergone (hereafter $F_{(Yb\ in\ WR)}$). The majority of New Zealand xenoliths have undisturbed MREE to HREE concentrations and are consistent with a single amount of melt depletion (Fig. 8c; WTL-1: F ≈ 10%; WTL-2: F ≈ 15 %; where F represents the percentage of melting), until the point of inflection related to the metasomatism of the sample. $F_{(Yb\ in\ WR)}$ is also negatively correlated with the amount of modal cpx in the samples (Fig. 16a; $r^2 = 0.90$), consistent with the progressive removal of cpx as melting proceeds. Based on this model, Zealandian xenoliths underwent between 3-28% partial melting (Table 4), with the most fertile samples ($F_{(Yb\ in\ WR)}$ <15 %) occurring exclusively in the Waitaha domain. Samples from extensively metasomatised localities may still record significant amounts of melt depletion if their HREE concentrations remain undisturbed (e.g. P80290; $F_{(Yb\ in WR)}$ = 24 %; Fig. 8g). To test the internal consistency of the model $F_{(Yb\ in\ WR)}$ is compared to $F_{(Y\ in\ WR)}$, with a 1:1 correlation observed in unmetasomatised samples (i.e. $Pr/Yb_N$ <1; Fig. 16d).

The measured concentrations of HREE in cpx, which are unlikely to be affected by metasomatism, can also be used to estimate the degree of melt depletion in these xenoliths (Fig. 5; $F_{(Dy\ in\ Cpx)}$ & $F_{(Yb\ in\ Cpx)}$; Table 4). Unlike based on the whole rock composition where the MREE-HREE concentrations of xenoliths are consistent with a

single F (Fig. 8), there are significant discrepancies between the calculated F within a single cpx depending on the REE chosen (Fig. 5). Some xenoliths contain cpx with Yb and/or Dy concentrations greater than cpx inferred to be in equilibrium with the PM (Fig. 4), and independent of their fertility can appear to be consistent with variable degrees of melting (e.g. Fig. 5; OU45852 or WRR-1). A comparison between $F_{(Yb\ in\ WR)}$ and $F_{(Yb\ in\ Cpx)}$ (Fig. 16e; hollow symbols) shows that $F_{(Yb\ in\ Cpx)}$ is consistently lower than $F_{(Yb\ in\ WR)}$, with this offset largest at lower degrees of melting. $F_{(Dy\ in\ Cpx)}$ is more variable due to the increased chance of metasomatic perturbation, but is still generally offset below the 1:1 line with a greater offset at lower F (Fig. 16f).

*The effect of subsolidus redistribution in mantle minerals*

The locus of melting in mantle peridotites probably occurs close to the dry solidus (ca. 1300ºC at 1.5 GPa; Hirschmann, 2000), and subsequently during emplacement and cooling to <1000 ºC in SCLM significant subsolidus redistribution of elements may occur. Recently Sun and Liang (2014) examined this problem in abyssal peridotites using parameterised lattice strain models, concluding that significant redistribution of REE occurs in ol, opx and garnet and perhaps in cpx, although, the extent of REE redistribution was considered insignificant when cpx modal abundances in the residual peridotite are high.

Here we have developed a set of equations to test whether subsolidus re-equilibration is the reason for the inconsistency observed between the cpx and the whole rock melting indices (Fig. 16e-f; Table 6). As pyroxenes essentially control the entire REE budget of spinel peridotites (e.g. Fig. A1.3; Eggins *et al.*, 1998) for simplicity we ignore any contributions from ol and sp. First we need to calculate the relative

proportions of cpx and opx at the locus of melting. In calculating the modal proportion of minerals in spinel lherzolites we use the constraint that the proportions of ol + sp to cpx + opx remain constant at constant composition, as temperature and pressure change:

$$X_{Opx} + X_{Cpx} = Y_{Opx} + Y_{Cpx} \quad (1)$$

Here $X_{Opx}$ and $X_{Cpx}$ are the modal proportions of these minerals as calculated by least squares regression at the current equilibration temperature (i.e. ca. 900 ºC) and $Y_{Opx}$ and $Y_{Cpx}$ are the unknown proportions of the minerals at the locus of melting (i.e. >1300 ºC). This constraint holds (Eq. 1) because ol and sp have 9 cations to 12 oxygens while opx and cpx have 8 cations to 12 oxygens, and the total number of cations to oxygens in the bulk composition is a function of that composition only. Secondly, based on stoichiometric arguments, CaO exchange is fixed between the two phases thus:

$$CaO_{Opx} \times X_{Opx} + X_{Cpx} \times CaO_{Cpx} = Y_{Opx} \times [CaO_{Opx}] + Y_{Cpx} \times [CaO_{Cpx}] \quad (2)$$

Where $CaO_{Opx}$ and $CaO_{Cpx}$ are the average concentrations of CaO measured in the phases by EPMA, and $[CaO_{Opx}]$ and $[CaO_{Cpx}]$ are the CaO concentrations at the locus of melting as assumed from an experimental study at 1300 ºC and 1.5 GPa (Falloon *et al.*, 1999; $Ca_{Opx}$ = 2.0 wt % and $Ca_{Cpx}$ = 15.8 wt %). Substitute Eq. 1 into Eq. 2 to solve for $Y_{Cpx}$:

$$Y_{Cpx} = \frac{[CaO_{Opx}] \times (X_{Opx} + X_{Cpx}) - (CaO_{Opx} \times X_{Opx} + CaO_{Cpx} \times X_{Cpx})}{[CaO_{Opx}] - [CaO_{Cpx}]} \quad (3)$$

Now that we know the relative proportions of the pyroxenes at the locus of melting, and assuming the stoichiometry reorganisation of an incompatible element (e.g. Yb) we can investigate the redistribution between the two phases during cooling. We know:

$$Yb_{Opx} \times X_{Opx} + Yb_{Cpx} \times X_{Cpx} = [Yb_{Opx}] \times Y_{Opx} + [Yb_{Cpx}] \times Y_{Cpx} \quad (4)$$

$$[Yb_{Cpx}] = [Yb_{Opx}] \times D_{Yb}^{Cpx/Opx} \quad (5)$$

Where $D_{Yb}^{Cpx/Opx}$ is the distribution coefficient for Yb between cpx and opx using the equation of Witt-Eickschen & O'Neill (2005), $Yb_{Cpx}$ is the average Yb concentration measured by LA-ICP-MS in the cpx, $Yb_{Opx}$ is the calculated concentration of Yb in opx calculated using Eq. 5 from Witt-Eickschen and O'Neill (2005) and the $D_{Yb}^{Cpx/Opx}$ relative to the xenolith, and $[Yb_{Opx}]$ and $[Yb_{Cpx}]$ are the unknown concentrations of Yb at the locus of melting in these phases. Combine these two equations to solve for $[Yb_{Opx}]$ gives:

$$[Yb_{Opx}] = \frac{Yb_{Opx} \times X_{Opx} + Yb_{Cpx} \times X_{Cpx}}{Y_{Opx} + (D_{Yb}^{Cpx/Opx} \times Y_{Cpx})} \quad (6)$$

After correcting for the subsolidus redistribution on cooling, the calculated concentrations of the elements at the locus of melting have been used to calculate $F_{(Dy\ in\ Cpx)}$ and $F_{(Yb\ in\ Cpx)}$. The calculated degrees of melting from the recalculated elemental abundances are now significantly more similar to each other (e.g. MSI20C; Table 6), consistent with the cpx crystal recording a single amount of melt extraction. $F_{(Dy\ in\ Cpx)}$ and $F_{(Yb\ in\ Cpx)}$ are now strongly correlated with $F_{(Yb)}$ plotting on top of the 1:1 line (Fig. 16e-f), suggesting this correction has been successful. Contrary to the modelling presented in Sun and Liang (2014) the results herein show in the spinel stability field that cpx may be strongly involved in the subsolidus re-equilibration of the REE, with the most significant amounts of redistribution observed in fertile samples (i.e. F may be underestimated by up to 12 % in fertile samples with modal cpx contents of ca. 10%).

*Comparisons with existing models and erroneous estimates of melt depletion*

The peritectic melting models discussed above have been compared with several commonly applied melt depletion models (Table 4 & Fig. 16). These are: 1) the model of Niu (1997) based on the strong correlation observed between the whole rock MgO

content in the residues of melting experiments and the degree of melt development (Baker & Stolper, 1994, Hirose & Kushiro, 1993, Jaques & Green, 1980) , hereafter referred to as $F_{(MgO)}$; and 2) the model of Hellebrand (2001) which is based on an empirical calibration of abyssal peridotites from mid-Atlantic Ridge with Cr# between 0.1 and 0.6 and the amount of melt extraction calculated using pure fractional melting of moderately incompatible elements (Dy, Er and Yb) in cpx, hereafter referred to as $F_{(Cr\# \text{ in } Sp)}$.

As $F_{(MgO)}$ is based on a major oxide component in ultramafic samples it should provide a robust estimate of the degree of melt depletion, although it can be perturbed by secondary Fe-enriched melts (Figs. 6 & 16c). A strong correlation is observed between $F_{(MgO)}$ and the modal content of cpx calculated in Zealandian xenoliths (Fig. 16b). $F_{(MgO)}$ and $F_{(Yb \text{ in } WR)}$ are also strongly correlated along the 1:1 line ($r^2 = 0.86$; based on the Waitaha domain) excluding samples that have undergone secondary processes (Fig. 16c)

$F_{(Cr\# \text{ in } Sp)}$ is well correlated with $F_{(Yb \text{ in } WR)}$ and $F_{(MgO)}$ (Fig. 16g-h) in the majority of samples from the Waitaha domain (excluding those effected by Fe-enrichment), however, $F_{(Cr\# \text{ in } Sp)}$ systematically underestimates the amount of melting that samples have experienced by ca. 8-12 %, irrespective of their fertility (e.g. WTL-3: $F_{(MgO)} = 13.4$ %, $F_{(Yb \text{ in } WR)} = 13.2$ %, $F_{(Cr\# \text{ in } Sp)} = 3.9$ %; WFP-5: $F_{(MgO)} = 26.1$ %, $F_{(Yb \text{ in } WR)} = 26.1$ %, $F_{(Cr\# \text{ in } Spl)} = 13.7$ %; Table 4)

Voigt & Handt (2011) investigated the effect subsolidus processes would have on the Cr# of sp in ultramafic rocks, and concluded that cooling from the liquidus to ca. 800 ºC would only result in an underestimation of $F_{(Cr\# \text{ in } Sp)}$ by up to 1.5 %. However, they did not account for the effect of Cr on the partitioning of Al. Chromium cannot be forced

into tetrahedral coordination and when Al in cpx approaches zero it becomes difficult to add Cr to this phase due to crystal field effects (e.g. Klemme & O'Neill, 2000, Liu & O'Neill, 2004). However, more importantly, the calibration of $F_{(Cr\# \text{ in Sp})}$ (Hellebrand *et al.*, 2005, 2001) is based on the amount of melting calculated using incompatible elements in cpx, and as shown above significant redistribution of these elements occurs in fertile samples. The thermal history of abyssal peridotites during subsolidus cooling is more protracted than in xenoliths (e.g. alkali basalt ascent rates are 3-9 m/s; Demouchy *et al.*, 2006), resulting in disequilibrium between cpx and opx. However, the failure to account for the effect of subsolidus redistribution in cpx, means that the equation of Hellebrand *et al.* (2001) to calculate the amount of melt depletion from the Cr# in sp is actually of limited value.

**Platinum group elements: the interplay between melt extraction signatures and secondary processes**

*Undisturbed melt depletion signatures in Zealandian xenoliths*

In mantle peridotites, PGE exhibit the following relative order of compatibility during mantle melting ($D^{solid/melt}$) Os = Ir >Ru > Pt > Pd (Pearson *et al.*, 2004), with the majority of PGE shown to be hosted within heterogeneously distributed Cu–Fe–Ni sulfides and alloys (Handler & Bennett, 1999, Luguet *et al.*, 2007, Wittig *et al.*, 2010). Within New Zealand mantle xenoliths, Os, Ir, and Ru are correlated and occur in PM-like abundances in the majority of samples (Figs. 9 & 10), consistent with the strongly compatible behaviour of these I-PGE during mantle melting (e.g. Handler & Bennett, 1999, Li *et al.*, 1996, Lorand *et al.*, 1999) and the residual base metal sulfides observed in the majority of

xenoliths (Fig. 2). Additionally, there is a lack of correlation between I-PGE and indices of melt depletion (e.g. $Al_2O_3$) even to very high degrees of partial melting (i.e. $Ru/Ir_N$ remains constant and within the range of the PM while F ≤30 %; Fig. 20a). Whereas the P-PGE, especially Pd and Re are generally strongly depleted relative to the PM in most Zealandian xenoliths (Figs. 9 & 10), with the largest depletions occurring at larger degrees of partial melting (i.e. MSI79C: Pd = 5.9 ppb at $F_{(Yb\ in\ WR)}$ = 8.4 % vs. MSI20C: Pd = 0.6 ppb at $F_{(Yb\ in\ WR)}$ = 25.5 %; Fig. 9e). Consistent with studies showing that as partial melting proceeds, Pd–Cu–Ni rich sulfides are preferentially removed because Pd readily partitions into Cu-sulfide melt and eventually dissolves into silicate melt as Pd is soluble at ppm levels in basaltic magmas (Borisov & Palme, 2000), resulting in large fractionation of the P-PGE from the I-PGE observed in melting residues (Bockrath *et al.*, 2004a, Lorand *et al.*, 1999). The PGE patterns of xenoliths from the Trig L locality record progressive P-PGE depletion (Fig. 9f), that is coupled to the fertility of these xenoliths ($F_{(MgO)}$ =11-18%; Table 6) and their $^{187}Os/^{188}Os$ ratios (Fig10f), consistent with the Re-Os isochron of McCoy-West *et al.* (2013) being a valid age relationship.

The distribution, abundance and relative proportions of the PGEs in the trace phases that control a rocks PGE budget are largely unresolved issues that complicate modelling of the PGE contents of mantle derived melts or their residues. Simple melting models that calculate the fraction of base metal sulfide remaining in the system, are broadly successful in describing the behaviour of monosulfide solid solutions (mss = $Fe_{1-x}Ni_{1-x}S$) compatible elements (i.e. I-PGE), although they often fail to properly explain the behaviour of P-PGE at a simplistic level (see Fig. 4 in Lorand *et al.*, 2013). The behaviour of Pd relative to Ir (Fig. 10d), which, although weakly correlated with indices

of melt depletion, is too variable to be accurately quantitatively modelled by batch melting processes. Distinct from the other P-PGE, Pt occurs in PM-like concentrations in more than half of the xenoliths ($n$ = 16/27) and is positively correlated with Ir ($r^2 = 0.83$; Figs. 9 & 10). However, its behaviour also appears to be strongly dependent on the degree of melt extraction. At >1.5 wt % $Al_2O_3$ samples within the Waitaha domain have $Pt/Ir_N$ that remains constant at 0.97 ± 0.08 (1σ), comparable to PM estimates (Becker *et al.*, 2006; $Pt/Ir_N = 1.12 \pm 0.23$), while at $Al_2O_3$ <1.5 wt % $Pt/Ir_N$ drops rapidly approaching zero in some Chatham Island xenoliths (Fig. 10e).

Although accurate modelling of PGE during mantle melting is complicated, it is well known that the partitioning behaviour of PGE is strongly dependant on sulfur availability (Andrews & Brenan, 2002, Fleet *et al.*, 1996). Using the mass balance equation $C_0 = FC_l + (1-F)C_r$ indicates that residual mss ($C_r = 0$) will be eliminated from the restite after 20-25 % melting (Fig. 17) depending on the values chosen for $C_l$ (i.e. solubility of S in the partial melt = 1000 or 1197 ppm; Mavrogenes & O'Neill, 1999; Jenner & O'Neill, 2012) and $C_0$ (i.e. S concentration of the primitive source = 200 or 250 ppm; Becker et al., 2006; Palme & O'Neill, 2003). When $Pt/Ir_N$ is plotted against the calculated melting percentage (F; Fig. 17b), it becomes clear that the rapid drop in the $Pt/Ir_N$ occurs at the same time at which S is near to/becomes exhausted in the melting residue (i.e. F >20%). This is consistent with Ir being retained in refractory PGE-rich phases (i.e. Ru–Os–Ir alloys and laurite) that form when mss breaks down, due to its very low solubility (ca. 10 ppb level) in basaltic melts (Barnes & Fiorentini, 2008, Borisov & Palme, 2000). Whereas, Pt initially begins to form Pt-Ir-(Os) alloys after moderate amounts of melting due to its low solubility in residual mss (i.e. relative to Ru; Barnes *et*

*al.*, 2001, Bockrath *et al.*, 2004b, Brenan & Andrews, 2001). However, prior to the complete disappearance of mss when the partial melts become S undersaturated, Pt-Ir-(Os) alloys break down to form Ru-Os rich alloys or laurite series minerals (Lorand *et al.*, 2013) liberating the Pt into the sulfide melt causing a rapid drop in $Pt/Ir_N$ (Fig. 17b).

Despite the observations herein of significant refertilisation and widespread carbonatite metasomatism occurring in the Zealandian SCLM, the majority of xenoliths possess undisturbed PGE patterns (especially I-PGE contents) that are consistent with a simple melt depletion history.

*Secondary processes that may mobilise PGEs*

The extremely heterogeneous distribution of the minute alloys and sulfides that dominate the PGE budget of peridotites mean that nugget effects are often observed in the cratonic SCLM (e.g. Aulbach *et al.*, 2004, Griffin *et al.*, 2004). Due to the small size of some xenoliths analysed here nugget effects could explain some of the observed variability. The small refractory xenoliths from Ngatutura Point exhibit variable Os contents, PGE patterns and anomalously high $Pt/Ir_N$ (Figs. 9 & 10) consistent with the heterogeneous distribution of micron size PGE nuggets. Additionally, small xenoliths with variable I-PGE contents greater than those of the PM could be attributed to nugget effects (e.g. DPP-6; Fig. 9h; note also a positive Pt anomaly).

Approximately half of the off-cratonic xenoliths analysed worldwide display marked whole rock Os depletions relative to Ir (Handler *et al.*, 2005, Ionov *et al.*, 2006, Lorand *et al.*, 2013). This is surprising given that these elements are not easily fractionated by magmatic processes and are equally compatible during mantle melting

(Ballhaus *et al.*, 2006, Fleet *et al.*, 1999, Mungall & Brenan, 2014). Three processes have been suggested to account for these Os depletions: 1) selective removal of Os during supergene weathering of host base metal sulfides (e.g. Handler & Bennett, 1999); 2) degassing of the highly volatile compound $OsO_4$ from the host magma during emplacement (e.g. Lorand *et al.*, 2003a); and 3) interaction with S-undersaturated fluids resulting in sulfide break down (Liu *et al.*, 2010). However, Os-loss has played only a minor role in the Zealandian xenoliths with the majority of samples having PM-like Os concentrations (Fig. 9) and only four samples having <1 ppb Os (e.g. P43153b), providing assurance as to the undisturbed PGE budget of these rocks. Additionally some of these low-Os samples also exhibit positive Ru anomalies (e.g. P80291; Fig. 9c), which have been attributed to complex desulfidation reactions of residual mss, liberating Pt-Ir-Os alloys while leaving Ru due to its preference for more refractory sulfides (i.e. laurite; Brenan & Andrews, 2001).

The uppermost SCLM is a region where secondary base metal sulfide precipitation preferentially occurs, because ofthe progressive consumption of upwelling silicate melts, eventually resulting in S-saturation. This process can lead to the formation of numerous intergranular blebs a few tens of micrometres across, composed of pentlandite and chalcopyrite intergrowths (Lorand *et al.*, 2003b) and cause possibly Pd enrichments unrelated to general peridotite fertility (Handler & Bennett, 1999). Although significant Pd enrichments are not observed in Zealandian xenoliths several samples contain >100 interstitial sulfides (Table 2) that can be coupled with Re-enrichments (e.g. P43153b; Fig. 9). Coupled Os-loss and secondary Re-enrichment are responsible for the erratic Re-Os systematics of sample WFP-1 (Fig. 18), and result in a large two-stage

correction being required for sample P43153b due to its elevated Re/Os ($^{187}Re/^{188}Os$ = 44.6; $T_{RD2}$ = 2.32 Ga; McCoy-West *et al.*, 2013). Therefore, this single Proterozoic model age from outside the Waitaha domain should be interpreted with caution.

**Refinement of the age of the Paleoproterozoic Waitaha domain**

Based on new major and trace element data presented here we have extended the boundaries of the Paleoproterozoic Waitaha domain underlying southern Zealandia. Previously, the Fortification Peak locality was excluded from the Waitaha domain based on the poor fit of the xenoliths on the regional aluminochron ($Al_{(0.60)}$ = 1.94 ± 0.31 Ga; McCoy-West *et al.*, 2013), despite the close spatial proximity to other localities in the Otago region (Fig. A1.1). However, here Fortification Peak (and Five Forks) are now considered to be part of the Waitaha domain due to their strong correlation with major and trace element trends observed elsewhere within the Waitaha domain. Additionally, the two Fortification Peak xenoliths that preserve PM-like Os concentrations (Os = 3.0-4.8 ppb) have Paleoproterozoic Os model ages (WFP-2 $T_{MA}$ = 1.84 Ga; WFP-8 $T_{MA}$ = 1.78 Ga; McCoy-West *et al.*, 2013).

The inclusion of Fortification Peak within the Waitaha domain results in a strong correlation being observed between $^{187}Os/^{188}Os_{(i)}$ and $^{187}Re/^{188}Os$ (Fig. 18a; $r^2$ = 0.85). The Re depletion intercept age calculated from this regression is 1.99 ± 0.21 Ga and is within error of the 'errorchron' age of 2.12 ± 0.57 Ga calculated from the slope (Ludwig, 2008), consistent with this correlation being a valid age relationship. Recalculation of whole rock $Fe_2O_3$ to FeO, resulted in a small shift in $Al_2O_3$ contents (≤ 2 % relative), and subsequently the revised aluminochron age for the Waitaha domain is 1.91 ± 0.39 Ga

(Fig. 18b; $r^2 = 0.72$). This regression includes one additional sample (WFP-8) from Fortification Peak, and is almost identical with a slightly larger error to that presented in McCoy-West *et al.* (2013). Refinement of the age of the Waitaha domain herein to 1.99 ± 0.21 Ga has not resulted in any reinterpretations of the geologic history. However, there is now nothing constraining the southern limit of the Waitaha domain, which has an increased minimum extent of ≥ ca. 55,000 $km^2$. Furthermore, the significant temperature range 880-1000 °C preserved in nearby Waitaha domain localities with ancient Re-Os ages, consistent with sampling of the entire spinel facies mantle, suggests that at least ca. 2 million $km^3$ of Paleoproterozoic SCLM underlies Zealandia, although this region could be significantly larger if it extends underneath the Campbell Plateau.

**Summary of the melting and metasomatic history of the Zealandian lithosphere**

Re-Os isotopic evidence from mantle xenoliths within the Waitaha domain are consistent with a widespread region (ca. 55,000 $km^2$) of SCLM that underwent melt depletion in the Paleoproterozoic at ca. 2.0 Ga. Additionally, the undisturbed PGE patterns (i.e. lower P-PGE to I-PGE; Fig. 9) and coherent Re-Os systematics (i.e. Re-Os errorchron; Fig. 18) of the majority of samples in the Waitaha domain, requires both a relatively simple melt depletion history and the long-term preservation of their original mantle sulfides. Other regions of the SCLM underpinning Zealandia are considerably younger, with two further regions recognised (McCoy-West *et al.*, 2013): 1) xenoliths from the Chatham Islands are probably consistent with the SCLM undergoing melt depletion in the Neoproterozoic (ca. 0.8-1.1 Ga); and 2) other regions of mainland New Zealand outside the Waitaha domain (i.e. especially those located to the west of the Alpine Fault) probably formed during

crustal growth at the eastern margin of Gondwana in the early Phanerozoic (ca. 0.35-0.54 Ga).

The SCLM of Zealandia represents an example of a long-lived (ca. 2 Gyr) coherent region, that despite being variably but not extensively depleted (Fo = 89.4-91.7), has been preserved without being recycled back into the asthenosphere. Conventionally, the SCLM is considered to resist delamination because of density, temperature and water conditions which create a thermal boundary layer isolating it from the convecting mantle (Carlson, 1995, Lee *et al.*, 2011). Geophysical evidence suggests that the Waitaha domain has become completely decoupled from its original overlying crust, with seismic, magnetic and density profiles of the surface terranes continuous to mid-to lower crustal depths with no evidence for an intra-crustal decollement (Mortimer *et al.*, 2002, Stern *et al.*, 2007). However, if the Waitaha SCLM had been exhumed from below its complementary crust for >1.5 Gyr it seems unlikely it would have survived, due to the minimal density contrast between this SCLM and the asthenospheric mantle ($\Delta\rho_{SCLM\text{-}ASP}$ = 0.02-0.05 $Mgm^{-3}$). Instead in this instance it could be argued that it was probably the buoyant overlying crust that aided in the preservation of this weakly buoyant SCLM and that complete decoupling occurred relatively recently.

Lithophile trace elements record a distinctive metasomatic signature with positive U-Th anomalies and HFSE depletion that is observed in a widespread region regardless of the Re-Os age of the SCLM (i.e. cpx trace element patterns; Figs. A1.7-8). This carbonatite-type metasomatism widely distributed throughout the lithosphere of Zealandia (this study; Scott *et al.*, 2014a, 2014b), and is also observed in the SCLM as far away as Marie Byrd Land and Victoria Land, West Antarctica (Martin *et al.*, 2013, Panter

*et al.*, 2000). The similarity of this metasomatic signature over such a broad area with variable SCLM formation ages requires that this metasomatic event occurred sometime in the Late Phanerozoic, but prior to the separation of Zealandia from Marie Byrd Land during the break-up of Gondwana and the onset of basaltic magmatism with this signature at ca. 100 Ma (McCoy-West *et al.*, 2010), consistent with suggestions of previous authors (Hart *et al.*, 1997, Panter *et al.*, 2006, 2000). However, the exact timing and origin of this metasomatic signature (e.g. subduction or plume related) remains unresolved.

## CONCLUSIONS

A comprehensive petrologic study of 40 mantle xenoliths from 13 localities around the micro-continent of New Zealand has shown that:

1) Mantle xenoliths from underneath Zealandia are exclusively derived from the spinel facies with equilibration temperatures varying between ca. 850-1050 °C. Large temperature gradients observed between nearby localities <20 km apart suggests sampling of the entire spinel facies SCLM.
2) Major element systematics are consistent with a variably depleted off-cratonic mantle that underwent ca. 5-28 % melting. Secondary processes have affected some xenoliths; elevated Ca/Al is the result of cryptic refertilisation and subsequent clinopyroxene formation, while interaction with Fe-rich melts resulted in elevated $FeO_T$ and low forsterite olivine.
3) Metasomatism is complex with samples varying from those with weak REE enrichment and notable positive Sr and U-Th anomalies and negative Nb-Ta anomalies in clinopyroxene to those that have extremely high concentrations of REE, Th-U and Nb. Fractionations of Nb/Ta and depletions in Ti in clinopyroxene are consistent with pervasive interaction with carbonatite-type melts at the base of the SCLM.

4) Notably, PGE systematics are unaffected by this widespread metasomatic overprint, rather being consistent with simple melt depletion history and the retention of base metal sulfides in the majority of xenoliths. The rapid decrease in $Pt/Ir_N$ observed at ca. 1 wt % $Al_2O_3$ is a direct result of the exhaustion of sulfide in the mantle residue at ca. 25% melting and the inability of Pt to form a stable alloy phase.
5) Peritectic melting models indicate that the Zealandian xenoliths are the residues of between 3 to 28% partial melting. Models presented here, in contrast to previous studies, show that clinopyroxene is strongly involved in the subsolidus redistribution of the REE. Failure to account for the effect of subsolidus redistribution in clinopyroxene, leads to underestimation of the amount of melt extraction by up to 12 % in fertile samples and means that some widely-used methods are of limited value (e.g. Cr# in spinel calculation of Hellebrand *et al.* 2001).
6) The age distribution and chemical composition of SCLM associated with the young micro-continent Zealandia demonstrates the stabilisation of weakly buoyant off-cratonic Paleoproterozoic-Phanerozoic SCLM, despite widespread refertilisation and metasomatism. This provides a clear demonstration of continent stabilisation in the absence of Archean SCLM.

**Acknowledgements**

AMW's visit to UMD was funded by an ANU Vice Chancellors Travel Grant and a J.C. Jaeger Fellowship at the ANU. T. Ireland, N. Mortimer, H. Campbell, C. Timm, K. Hoernle, I. Smith and A. Raey are thanked for providing samples. B. Rapp, C. Allen and J-W. Park provided analytical assistance. J. Wykes and P. Sossi are thanked for analyses of calibrated spinel standards. T. Whan, H. Cocker, D. Ionov and V. Salters are thanked for comments on an earlier draft of this manuscript. J. Gamble is thanked for editorial assistance with formal journal reviews by A. Peslier, C. Timm and A. Martin significantly improving the manuscript.

## REFERENCES


Andrews, D. R. A. & Brenan, J. M. (2002). The solubility of ruthenium in sulfide liquid: Implications for platinum group mineral stability and sulfide melt–silicate melt partitioning. *Chemical Geology* **192**, 163-181.

Aulbach, S., Griffin, W. L., Pearson, N. J., O'Reilly, S. Y., Kivi, K., Doyle, B. J. (2004). Mantle formation and evolution, Slave Craton: Constraints from HSE abundances and Re–Os isotope systematics of sulfide inclusions in mantle xenocrysts. *Chemical Geology* **208**, 61-88.

Baker, M. B. & Stolper, E. M. (1994). Determining the composition of high-pressure mantle melts using diamond aggregates. *Geochimica et Cosmochimica Acta* **58**, 2811-2827.

Ballhaus, C., Berry, R. F., Green, D. H. (1991). High pressure experimental calibration of the olivine-orthopyroxene-spinel oxygen geobarometer: implications for the oxidation state of the upper mantle. *Contributions to Mineralogy and Petrology* **107**, 27-40.

Ballhaus, C., Bockrath, C., Wohlgemuth-Ueberwasser, C., Laurenz, V., Berndt, J. (2006). Fractionation of the noble metals by physical processes. *Contributions to Mineralogy and Petrology* **152**, 667-684.

Barnes, S.-J., Naldrett, A. J., Gorton, M. P. (1985). The origin of the fractionation of platnium-group elements in terrestrial magmas. *Chemical Geology* **53**, 303-323.

Barnes, S.-J., van Achterbergh, E., Makovicky, E., Li, C. (2001). Proton microprobe results for the partitioning of platinum-group elements between monosulphide solid solution and sulphide liquid. *South African Journal of Geology* **104**, 275-286.

Barnes, S. J. & Fiorentini, M. L. (2008). Iridium, ruthenium and rhodium in komatiites: Evidence for iridium alloy saturation. *Chemical Geology* **257**, 44-58.

Barnes, S. J. & Roeder, P. L. (2001). The range of spinel compositions in terrestrial mafic and ultramafic rocks. *Journal of Petrology* **42**, 2279-2302.

Barreiro, B. A. & Cooper, A. F. (1987). A Sr, Nd, and Pb isotope study of alkaline lamprophyres and related rocks from Westland and Otago, South Island, New Zealand. *Geological Society of America Special Papers* **215**, 115-126.

Becker, H., Horan, M. F., Walker, R. J., Gao, S., Lorand, J. P., Rudnick, R. L. (2006). Highly siderophile element composition of the Earth's primitive upper mantle: Constraints from new data on peridotite massifs and xenoliths. *Geochimica et Cosmochimica Acta* **70**, 4528-4550.

Bedini, R. M. & Bodinier, J. L. (1999). Distribution of incompatible trace elements between the constituents of spinel peridotite xenoliths: ICP-MS data from the East African rift. *Geochimica et Cosmochimica Acta* **63**, 3883-3900.

Black, P. M. & Brothers, R. N. (1965). Olivine nodules in olivine nephelinite from Tokatoka, Northland. *New Zealand Journal of Geology and Geophysics* **8**, 62-80.

Bockrath, C., Ballhaus, C., Holzheid, A. (2004a). Fractionation of the platinum-group elements during mantle melting. *Science* **305**, 1951-1953.

Bockrath, C., Ballhaus, C., Holzheid, A. (2004b). Stabilities of laurite $RuS_2$ and monosulfide liquid solution at magmatic temperature. *Chemical Geology* **208**, 265-271.

Bodinier, J.-L. & Godard, M. (2003). Orogenic, ophiolitic, and abyssal peridotites. In: Carlson, R. W. (ed.) *Treatise of Geochemistry*. Amsterdam, Netherlands: Elsevier, 103-170.

Bodinier, J. L., Dupuy, C., Dostal, J. (1988). Geochemistry and petrogenesis of Eastern Pyrenean peridotites. *Geochimica et Cosmochimica Acta* **52**, 2893-2907.

Borisov, A. & Palme, H. (2000). Solubilities of noble metals in Fe-containing silicate melts as derived from experiments in Fe-free systems. *American Mineralogist* **85**, 1665-1673.

Boyd, F. R., Pokhilenko, N. P., Pearson, D. G., Mertzman, S. A., Sobolev, N. V., Finger, L. W. (1997). Composition of the Siberian cratonic mantle: evidence from Udachnaya peridotite xenoliths. *Contributions to Mineralogy and Petrology* **128**, 228-246.

Brenan, J. M. & Andrews, D. (2001). High-temperature stability of laurite and Ru-Os-Ir alloy and their role in PGE fractionation in mafic magmas. *The Canadian Mineralogist* **39**, 341-360.

Brey, G. P. & Köhler, T. P. (1990). Geothermobarometry in four-phase lherzolites II: New thermobarometers, and practical assessment of existing thermobarometers. *Journal of Petrology* **31**, 1353-1378.

Brothers, R. N. & Rodgers, K. A. (1969). Petrofabric studies of ultramafic nodules from Auckland, New Zealand. *The Journal of Geology* **77**, 452-465.

Bryndzia, L. T. & Wood, B. J. (1990). Oxygen thermobarometry of abyssal spinel peridotites: The redox state and C-O-H volatile composition of the Earth's sub-oceanic upper mantle. *American Journal of Science* **290**, 1093-1116.

Canil, D. & O'Neill, H. S. C. (1996). Distribution of ferric iron in some upper-mantle assemblages. *Journal of Petrology* **37**, 609-635.

Carlson, R. W. (1995). A continental life preserver. *News and Views: Nature* **376**, 116-117.

Coombs, D. S., Adams, C. J., Roser, B. P., Reay, A. (2008). Geochronology and geochemistry of the Dunedin Volcanic Group, eastern Otago, New Zealand. *New Zealand Journal of Geology and Geophysics* **51**, 195-218.

Cooper, A. F., Barreiro, B. A., Kimbrough, D. L., Mattinson, J. M. (1987). Lamprophyre dike intrusion and the age of the Alpine Fault, New Zealand. *Geology* **15**, 941-944.

Cooper, A. F. & Paterson, L. A. (2008). Carbonatites from a lamprophyric dyke swarm, South Westland, New Zealand. *Canadian Mineralogist* **46**, 753-777.

Cooper, R. A. & Tulloch, A. J. (1992). Early Paleozoic terranes in New Zealand and their relationship to the Lachlan Fold Belt. *Tectonophysics* **214**, 129-144.

Dawson, J. B., Pinkerton, H., Norton, G. E., Pyle, D. M. (1990). Physicochemical properties of alkali carbonatite lavas: Data from the 1988 eruption of Oldoinyo Lengai, Tanzania. *Geology* **18**, 260-263.

De Hoog, J. C. M., Gall, L., Cornell, D. H. (2010). Trace-element geochemistry of mantle olivine and application to mantle petrogenesis and geothermobarometry. *Chemical Geology* **270**, 196-215.

Demouchy, S., Jacobsen, S. D., Gaillard, F., Stern, C. R. (2006). Rapid magma ascent recorded by water diffusion profiles in mantle olivine. *Geology* **34**, 429-432.

Dick, H. J. & Bullen, T. (1984). Chromian spinel as a petrogenetic indicator in abyssal and alpine-type peridotites and spatially associated lavas. *Contributions to Mineralogy and Petrology* **86**, 54-76.

Durazzo, A. & Taylor, L. A. (1982). Exsolution in the mss-pentlandite system: Textural and genetic implications for Ni-sulfide ores. *Mineralium Deposita* **17**, 313-332.

Eagles, G., Gohl, K., Larter, R. D. (2004). High-resolution animated tectonic reconstruction of the South Pacific and West Antarctic margin. *Geochemistry Geophysics Geosystems* **5**, Q07002, doi:07010.01029/02003GC000657.

Eggins, S. M., Rudnick, R. L., McDonough, W. F. (1998). The composition of peridotites and their minerals: a laser-ablation ICP–MS study. *Earth and Planetary Science Letters* **154**, 53-71.

Eggler, D. H. & Lorand, J. P. (1993). Mantle sulfide geobarometry. *Geochimica et Cosmochimica Acta* **57**, 2213-2222.

Falloon, T. J., Green, D. H., Danyushevsky, L. V., Faul, U. H. (1999). Peridotite melting at 1.0 and 1.5 GPa: An experimental evaluation of techniques using diamond aggregates and mineral mixes for determination of near-solidus melts. *Journal of Petrology* **40**, 1343-1375.

Fleet, M. E., Crocket, J. H., Liu, M., Stone, W. E. (1999). Laboratory partitioning of platinum-group elements (PGE) and gold with application to magmatic sulfide–PGE deposits. *Lithos* **47**, 127-142.

Fleet, M. E., Crocket, J. H., Stone, W. E. (1996). Partitioning of platinum-group elements (Os, Ir, Ru, Pt, Pd) and gold between sulfide liquid and basalt melt. *Geochimica et Cosmochimica Acta* **60**, 2397-2412.

Frost, D. J. & McCammon, C. A. (2008). The Redox State of Earth's Mantle. *Annual Review of Earth and Planetary Sciences* **36**, 389-420.

Gamble, J. A., Morris, P. A., Adams, C. J. (1986). The geology, petrology and geochemistry of Cenozoic volcanic rocks from the Campbell Plateau and Chatham Rise. In: Smith, I. E. M. (ed.) *Late Cenozoic volcanism in New Zealand*: Royal Society of New Zealand Bulletin, 344-365.

Green, D. H. & Wallace, L. M. (1988). Mantle metasomatism by ephemeral carbonatite melts. *Nature* **336**, 459-462.

Green, T. H., Adam, J., Siel, S. H. (1992). Trace element partitioning between silicate minerals and carbonatite at 25 kbar and application to mantle metasomatism. *Mineralogy and Petrology* **46**, 179-184.

Griffin, W. L., Begg, G. C., Dunn, D., O'Reilly, S. Y., Natapov, L. M., Karlstrom, K. (2011). Archean lithospheric mantle beneath Arkansas: Continental growth by microcontinent accretion. *Geological Society of America Bulletin* **123**, 1763-1775.

Griffin, W. L., Belousova, E. A., O'Neill, C., O'Reilly, S. Y., Malkovets, V., Pearson, N. J., Spetsius, S., Wilde, S. A. (2014). The world turns over: Hadean–Archean crust–mantle evolution. *Lithos* **189**, 2-15.

Griffin, W. L., Graham, S., O'Reilly, S. Y., Pearson, N. J. (2004). Lithosphere evolution beneath the Kaapvaal Craton: Re–Os systematics of sulfides in mantle-derived peridotites. *Chemical Geology* **208**, 89-118.

Griffin, W. L., O'Reilly, S. Y., Ryan, C. G., Gaul, O., Ionov, D. A. (1998). Secular variation in the composition of the subcontinental lithospheric mantle: Geophysical and geodynamic implications. In: Braun, J., Dooley, J. C., Goleby, B. R., van der Hilst, R. D., Klootwijk, C. T. (eds.) *Structure and evolution of the Australian continent*. Washington DC: American Geophysics Union, 1-26.

Griffin, W. L., O'Reilly, S. Y., Abe, N., Aulbach, S., Davies, R. M., Pearson, N. J., Doyle, B. J., Kivi, K. (2003). The origin and evolution of Archean lithospheric mantle. *Precambrian Research* **127**, 19-41.

Grindley, G. W., Adams, C. J., Lumb, J. T., Watters, W. A. (1977). Paleomagnetism, K-Ar dating and tectonic interpretation of Upper Cretaceous and Cenozoic volcanic rocks of the Chatham Islands, New Zealand. *New Zealand Journal of Geology and Geophysics* **20**, 425-467.

Handler, M. R. & Bennett, V. C. (1999). Behaviour of Platinum-group elements in the subcontinental mantle of eastern Australia during variable metasomatism and melt depletion. *Geochimica et Cosmochimica Acta* **63**, 3597-3618.

Handler, M. R., Bennett, V. C., Carlson, R. W. (2005). Nd, Sr and Os isotope systematics in young, fertile spinel peridotite xenoliths from northern Queensland, Australia: A unique view of depleted MORB mantle? *Geochimica et Cosmochimica Acta* **69**, 5747-5763.

Handler, M. R., Bennett, V. C., Esat, T. M. (1997). The persistence of off-cratonic lithospheric mantle: Os isotopic systematics of variably metasomatised southeast Australian xenoliths. *Earth and Planetary Science Letters* **151**, 61-75.

Hart, S. R., Blusztajn, J., LeMasurier, W. E., Rex, D. C. (1997). Hobbs Coast Cenozoic volcanism: Implications for the West Antarctic rift system. *Chemical Geology* **139**, 223-248.

Hellebrand, E., Snow, J., Mostefaoui, S., Hoppe, P. (2005). Trace element distribution between orthopyroxene and clinopyroxene in peridotites from the Gakkel Ridge: a SIMS and NanoSIMS study. *Contributions to Mineralogy and Petrology* **150**, 486-504.

Hellebrand, E., Snow, J. E., Dick, H. J. B., Hofmann, A. W. (2001). Coupled major and trace elements as indicators of the extent of melting in mid-ocean-ridge peridotites. *Nature* **410**, 677-681.

Herzberg, C. (2004). Geodynamic information in peridotite petrology. *Journal of Petrology* **45**, 2507-2530.

Herzberg, C. T. (1978). Pyroxene geothermometry and geobarometry: experimental and thermodynamic evaluation of some subsolidus phase relations involving pyroxenes in the system CaO-MgO-Al2O3-SiO2. *Geochimica et Cosmochimica Acta* **42**, 945-957.

Hirose, K. & Kushiro, I. (1993). Partial melting of dry peridotites at high pressures: Determination of compositions of melts segregated from peridotite using aggregates of diamond. *Earth and Planetary Science Letters* **114**, 477-489.

Hirschmann, M. M. (2000). Mantle solidus: Experimental constraints and the effects of peridotite composition. *Geochemistry, Geophysics, Geosystems* **1**, 1042.

Hoernle, K., Tilton, G., Le Bas, M., Duggen, S., Garbe-Schönberg, D. (2002). Geochemistry of oceanic carbonatites compared with continental carbonatites: Mantle recycling of oceanic crustal carbonate. *Contributions to Mineralogy and Petrology* **142**, 520-542.

Hoke, L., Poreda, R., Reay, A., Weaver, S. D. (2000). The subcontinental mantle beneath southern New Zealand, characterised by helium isotopes in intraplate basalts and gas-rich springs. *Geochimica et Cosmochimica Acta* **64**, 2489-2507.

Holland, T. J. B. & Powell, R. (1998). An internally consistent thermodynamic data set for phases of petrological interest. *Journal of Metamorphic Geology* **16**, 309-343.

Horan, M. F., Walker, R. J., Morgan, J. W., Grossman, J. N., Rubin, A. E. (2003). Highly siderophile elements in chondrites. *Chemical Geology* **196**, 27-42.

Ionov, D., Prikhodko, V., Bodinier, J.-L., Sobolev, A., Weis, D. (2005). Lithospheric mantle beneath the south-eastern Siberian craton: Petrology of peridotite xenoliths in basalts from the Tokinsky Stanovik. *Contributions to Mineralogy and Petrology* **149**, 647-665.

Ionov, D. A. (2007). Compositional variations and heterogeneity in fertile lithospheric mantle: Peridotite xenoliths in basalts from Tariat, Mongolia. *Contributions to Mineralogy and Petrology* **154**, 455-477.

Ionov, D. A., Bodinier, J.-L., Mukasa, S. B., Zanetti, A. (2002). Mechanisms and sources of mantle metasomatism: Major and trace element compositions of peridotite xenoliths from Spitsbergen in the context of numerical modelling. *Journal of Petrology* **43**, 2219-2259.

Ionov, D. A., Dupuy, C., O'Reilly, S. Y., Kopylova, M. G., Genshaft, Y. S. (1993). Carbonated peridotite xenoliths from Spitsbergen: Implications for trace element signature of mantle carbonate metasomatism. *Earth and Planetary Science Letters* **119**, 283-297.

Ionov, D. A. & Hofmann, A. W. (1995). Nb–Ta-rich mantle amphiboles and micas: Implications for subduction-related metasomatic trace element fractionations. *Earth and Planetary Science Letters* **131**, 341-356.

Ionov, D. A. & Hofmann, A. W. (2007). Depth of formation of subcontinental off-craton peridotites. *Earth and Planetary Science Letters* **261**, 620-634.

Ionov, D. A., Shirey, S. B., Weis, D., Brügmann, G. (2006). Os-Hf-Sr-Nd isotope and PGE systematics of spinel peridotite xenoliths from Tok, SE Siberian craton: Effects of pervasive metasomatism in shallow refractory mantle. *Earth and Planetary Science Letters* **241**, 47-64.

Janney, P. E., Shirey, S. B., Carlson, R. W., Pearson, D. G., Bell, D. R., Le Roex, A. P., Ishikawa, A., Nixon, P. H., Boyd, F. R. (2010). Age, composition and thermal characteristics of South African off-craton mantle lithosphere: Evidence for a multi-stage history. *Journal of Petrology* **51**, 1849-1890.

Jaques, A. L. & Green, D. H. (1980). Anhydrous melting of peridotite at 0–15 Kb pressure and the genesis of tholeiitic basalts. *Contributions to Mineralogy and Petrology* **73**, 287-310.

Jenner, F. E. & O'Neill, H. S. C. (2012). Major and trace analysis of basaltic glasses by laser-ablation ICP-MS. *Geochemistry, Geophysics, Geosystems* **13**, Q03003.

Kamenetsky, V. S., Crawford, A. J., Meffre, S. (2001). Factors controlling chemistry of magmatic spinel: An empirical study of associated olivine, Cr-spinel and melt inclusions from primitive rocks. *Journal of Petrology* **42**, 655-671.

Kimbrough, D. L., Tulloch, A. J., Coombs, D. S., Landis, C. A., Johnston, M. R., Mattinson, J. M. (1994). Uranium-lead zircon ages from the Median Tectonic Zone, New Zealand. *New Zealand Journal of Geology and Geophysics* **37**, 393-419.

Klemme, S. & Dalpé, C. (2003). Trace-element partitioning between apatite and carbonatite melt. *American Mineralogist* **88**, 639-646.

Klemme, S. & O'Neill, H. S. C. (2000). The effect of Cr on the solubility of Al in orthopyroxene: Experiments and thermodynamic modelling. *Contributions to Mineralogy and Petrology* **140**, 84-98.

Köhler, T. P. & Brey, G. P. (1990). Calcium exchange between olivine and clinopyroxene calibrated as a geothermobarometer for natural peridotites from 2 to 60 kb with applications. *Geochimica et Cosmochimica Acta* **54**, 2375-2388.

Larter, R. D., Cunningham, A. P., Barker, P. F., Gohl, K., Nitsche, F. O. (2002). Tectonic evolution of the Pacific margin of Antarctica 1. Late Cretaceous tectonic reconstructions. *Journal of Geophysical Research-Solid Earth* **107**, B122345, doi:122310.121029/122000JB000052.

Le Bas, M. J. & Streckeisen, A. L. (1991). The IUGS systematics of igneous rocks. *Journal of the Geological Society* **148**, 825-833.

Lee, C.-T. A., Luffi, P., Chin, E. J. (2011). Building and destroying continental mantle. *Annual Review of Earth and Planetary Sciences* **39**, 59-90.

Li, C., Barnes, S. J., Makovicky, E., Rose-Hansen, J., Makovicky, M. (1996). Partitioning of nickel, copper, iridium, rhenium, platinum, and palladium between monosulfide solid solution and sulfide liquid: Effects of composition and temperature. *Geochimica et Cosmochimica Acta* **60**, 1231-1238.

Liu, J., Rudnick, R. L., Walker, R. J., Gao, S., Wu, F., Piccoli, P. M. (2010). Processes controlling highly siderophile element fractionations in xenolithic peridotites and their influence on Os isotopes. *Earth and Planetary Science Letters* **297**, 287-297.

Liu, X. & O'Neill, H. S. C. (2004). Partial melting of spinel lherzolite in the system CaO–MgO–$Al_2O_3$–$SiO_2$ ± $K_2O$ at 1.1 GPa. *Journal of Petrology* **45**, 1339-1368.

Lorand, J.-P., Alard, O., Luguet, A., Keays, R. R. (2003a). Sulfur and selenium systematics of the subcontinental lithospheric mantle: Inferences from the Massif Central xenolith suite (France). *Geochimica et Cosmochimica Acta* **67**, 4137-4151.

Lorand, J.-P., Luguet, A., Alard, O. (2013). Platinum-group element systematics and petrogenetic processing of the continental upper mantle: A review. *Lithos* **164–167**, 2-21.

Lorand, J.-P., Pattou, L., Gros, M. (1999). Fractionation of platinum-group elements and gold in the upper mantle: A detailed study in Pyrenean orogenic lherzolites. *Journal of Petrology* **40**, 957-981.

Lorand, J.-P., Reisberg, L., Bedini, R. M. (2003b). Platinum-group elements and melt percolation processes in Sidamo spinel peridotite xenoliths, Ethiopia, East African Rift. *Chemical Geology* **196**, 57-75.

Ludwig, K. R. (2008). Isoplot 3.71. Berkeley Geochronology Centre.

Luguet, A., Shirey, S. B., Lorand, J.-P., Horan, M. F., Carlson, R. W. (2007). Residual platinum-group minerals from highly depleted harzburgites of the Lherz massif (France) and their role in HSE fractionation of the mantle. *Geochimica et Cosmochimica Acta* **71**, 3082-3097.

Luhr, J. F. & Aranda-Gómez, J. J. (1997). Mexican peridotite xenoliths and tectonic terranes: Correlations among vent location, texture, temperature, pressure, and oxygen fugacity. *Journal of Petrology* **38**, 1075-1112.

Martin, A. P., Cooper, A. F., Price, R. C. (2013). Petrogenesis of Cenozoic, alkalic volcanic lineages at Mount Morning, West Antarctica and their entrained lithospheric mantle xenoliths: Lithospheric versus asthenospheric mantle sources. *Geochimica et Cosmochimica Acta* **122**, 127-152.

Mavrogenes, J. A. & O'Neill, H. S. C. (1999). The relative effects of pressure, temperature and oxygen fugacity on the solubility of sulfide in mafic magmas. *Geochimica et Cosmochimica Acta* **63**, 1173-1180.

McCoy-West, A. J., Baker, J. A., Faure, K., Wysoczanski, R. (2010). Petrogenesis and origins of mid-Cretaceous continental intraplate volcanism in Marlborough, New Zealand: Implications for the long-lived HIMU magmatic mega-province of the SW Pacific. *Journal of Petrology* **51**, 2003-2045.

McCoy-West, A. J., Bennett, V. C., Puchtel, I. S., Walker, R. J. (2013). Extreme persistence of cratonic lithosphere in the Southwest Pacific: Paleoproterozoic Os isotopic signatures of Zealandia. *Geology* **41**, 231-234.

McDade, P., Blundy, J. D., Wood, B. J. (2003). Trace element partitioning on the Tinaquillo Lherzolite solidus at 1.5 GPa. *Physics of the Earth and Planetary Interiors* **139**, 129-147.

Meisel, T., Walker, R. J., Irving, A. J., Lorand, J.-P. (2001). Osmium isotopic compositions of mantle xenoliths: A global perspective. *Geochimica et Cosmochimica Acta* **65**, 1311-1323.

Menzies, M. A., Roggers, N., Tindle, A., Hawkesworth, C. J. (1987). Metasomatic and enrichment processes in lithopsheric peridotites, an efffect of asthenosphere-lithosphere interaction. In: Menzies, M. A. & Hawkesworth, C. J. (eds.) *Mantle metasomatism*. London, United Kingdom: Acedemic Press, 313-361.

Morris, P. A. (1985a). The geochemistry of Eocene-Oligocene volcanics on the Chatham Islands, New Zealand. *New Zealand Journal of Geology and Geophysics* **28**, 459-469.

Morris, P. A. (1985b). Petrology of Late Cretaceous alkaline volcanic rocks from the Chatham Islands, New Zealand. *New Zealand Journal of Geology and Geophysics* **28**, 253-266.

Mortimer, N. (2004). New Zealand's geological foundations. *Gondwana Research* **7**, 261-272.

Mortimer, N. & Campbell, H. J. (2014). *Zealandia: Our continent revealed*. New Zealand: Penguin Books.

Mortimer, N., Davey, F. J., Melhuish, A., Yu, J., Godfrey, N. J. (2002). Geological interpretation of a deep seismic reflection profile across the Eastern Province and Median Batholith, New Zealand: Crustal architecture of an extended Phanerozoic convergent orogen. *New Zealand Journal of Geology and Geophysics* **45**, 349-363.

Mortimer, N., Tulloch, A. J., Spark, R. N., Walker, N. W., Ladley, E., Allibone, A., Kimbrough, D. L. (1999). Overview of the Median Batholith, New Zealand: A new interpretation of the geology of the Median Tectonic Zone and adjacent rocks. *Journal of African Earth Sciences* **29**, 257-268.

Mungall, J. & Brenan, J. (2014). Partitioning of platinum-group elements and Au between sulfide liquid and basalt and the origins of mantle-crust fractionation of the chalcophile elements. *Geochimica et Cosmochimica Acta* **125**, 265-289.

Nelson, D. R., Chivas, A. R., Chappell, B. W., McCulloch, M. T. (1988). Geochemical and isotopic systematics in carbonatites and implications for the evolution of ocean-island sources. *Geochimica et Cosmochimica Acta* **52**, 1-17.

Niu, Y. (1997). Mantle melting and melt extraction processes beneath ocean ridges: Evidence from abyssal peridotites. *Journal of Petrology* **38**, 1047-1074.

O'Neill, H. S. C. (1981). The transition between spinel lherzolite and garnet lherzolite, and its use as a geobarometer. *Contributions to Mineralogy and Petrology* **77**, 185-194.

O'Neill, H. S. C. & Wall, V. J. (1987). The olivine-orthopyroxene-spinel oxygen geobarometer, the nickel precipitation curve, and the oxygen fugacity of the Earth's upper mantle. *Journal of Petrology* **28**, 1169-1191.

Palme, H. & O'Neill, H. S. C. (2003). Cosmochemical estimates of mantle composition. In: Holland, H. D. & Turrekian, K. K. (eds.) *Treatise of Geochemistry*. Amsterdam, Netherlands: Elsevier, 1-38.

Panter, K. S., Blusztajn, J., Hart, S. R., Kyle, P. R., Esser, R., McIntosh, W. C. (2006). The origin of HIMU in the SW Pacific: Evidence from intraplate volcanism in southern New Zealand and Subantarctic Islands. *Journal of Petrology* **47**, 1673-1704.

Panter, K. S., Hart, S. R., Kyle, P., Blusztanjn, J., Wilch, T. (2000). Geochemistry of Late Cenozoic basalts from the Crary Mountains: characterization of mantle sources in Marie Byrd Land, Antarctica. *Chemical Geology* **165**, 215-241.

Pearson, D. G., Canil, D., Shirey, S. B. (2003). Mantle samples included in volcanic rocks: Xenoliths and diamonds. In: Carlson, R. W. (ed.) *Treatise of Geochemistry*. Amsterdam, Netherlands: Elsevier, 171-276.

Pearson, D. G., Irvine, G. J., Carlson, R. W., Kopylova, M. G., Ionov, D. A. (2002). The development of lithospheric keels beneath the earliest continents: time constraints using PGE and Re-Os isotope systematics. *Geological Society, London, Special Publications* **199**, 65-90.

Pearson, D. G., Irvine, G. J., Ionov, D. A., Boyd, F. R., Dreibus, G. E. (2004). Re-Os isotope systematics and platinum group element fractionation during mantle melt extraction: A study of massif and xenolith peridotite suites. *Chemical Geology* **208**, 29-59.

Pearson, D. G. & Nowell, G. M. (2004). Re-Os and Lu-Hf isotope constraints on the origin and age of pyroxenites from the Beni Bousera peridotite massif: Implications for mixed peridotite-pyroxenite mantle sources. *Journal of Petrology* **45**, 439-455.

Pearson, D. G., Shirey, S. B., Carlson, R. W., Boyd, F. R., Pokhilenko, N. P., Shimizu, N. (1995). Re-Os, Sm-Nd, and Rb-Sr isotope evidence for thick Archaean lithospheric mantle beneath the Siberian craton modified by multistage metasomatism. *Geochimica et Cosmochimica Acta* **59**, 959-977.

Peslier, A. H., Francis, D., Ludden, J. (2002). The lithospheric mantle beneath continental margins: Melting and melt–rock reaction in Canadian Cordillera xenoliths. *Journal of Petrology* **43**, 2013-2047.

Peslier, A. H., Reisberg, L., Ludden, J., Francis, D. (2000). Os isotopic systematics in mantle xenoliths: Age constraints on the Canadian Cordillera lithosphere. *Chemical Geology* **166**, 85-101.

Poudjom Djomani, Y. H., O'Reilly, S. Y., Griffin, W. L., Morgan, P. (2001). The density structure of subcontinental lithosphere through time. *Earth and Planetary Science Letters* **184**, 605-621.

Price, R. C., Cooper, A. F., Woodhead, J. D., Cartwright, I. (2003). Phonolitic diatremes within the Dunedin Volcano, South Island, New Zealand. *Journal of Petrology* **44**, 2053-2080.

Price, R. C. & Green, D. H. (1972). Lherzolite nodules in a "mafic phonolite" from north-east Otago, New Zealand. *Nature* **235**, 133-134.

Rae, A. J. (1990). Geochemistry of the Siberia Hill volcanics and the ultramafic inclusions, Siberia Hill, East Otago, New Zealand. *Department of Geology*. Dunedin, New Zealand: University of Otago, 210.

Rafferty, W. J. & Heming, R. F. (1979). Quaternary alkalic and sub-alkalic volcanism in South Auckland, New Zealand. *Contributions to Mineralogy and Petrology* **71**, 139-150.

Reay, A., McIntosh, P. E., Gibson, I. L. (1991). Lherzolite xenolith bearing flows from the east Otago province: Crystal fractionation of upper mantle magmas. *New Zealand Journal of Geology and Geophysics* **34**, 317-327.

Reay, A. & Sipiera, P. P. (1987). Mantle xenoliths from the New Zealand region. In: Nixon, P. H. (ed.) *Mantle xenoliths*. Chichester, Great Britain: John Wiley & Sons Ltd., 347-358.

Reay, M. B. (1993). Geology of the middle Clarence Valley. *1:50,000 Geological Map 10. 1 sheet + 144p.* Lower Hutt, New Zealand: Institute of Geological and Nuclear Sciences

Robinson, J. A. C., Wood, B. J., Blundy, J. D. (1998). The beginning of melting of fertile and depleted peridotite at 1.5 GPa. *Earth and Planetary Science Letters* **155**, 97-111.

Rodgers, K. A. & Brothers, R. N. (1969). Olivine, pyroxene, feldspar and spinel in ultramafic nodules from Auckland, New Zealand. *Mineralogical Magazine* **37**, 375-390.

Rodgers, K. A., Brothers, R. N., Searle, E. J. (1975). Ultramafic nodules and their host rocks from Auckland, New Zealand. *Geological Magazine* **112**, 163-174.

Rudnick, R. L., McDonough, W. F., Chappell, B. W. (1993). Carbonatite metasomatism in the northern Tanzanian mantle: Petrographic and geochemical characteristics. *Earth and Planetary Science Letters* **114**, 463-475.

Scott, J. M., Hodgkinson, A., Palin, J. M., Waight, T. E., Meer, Q. H. A., Cooper, A. F. (2014a). Ancient melt depletion overprinted by young carbonatitic metasomatism in the New Zealand lithospheric mantle. *Contributions to Mineralogy and Petrology* **167**, 1-17.

Scott, J. M., Waight, T. E., van der Meer, Q. H. A., Palin, J. M., Cooper, A. F., Münker, C. (2014b). Metasomatized ancient lithospheric mantle beneath the young Zealandia microcontinent and its role in HIMU-like intraplate magmatism. *Geochemistry, Geophysics, Geosystems* **15**, 3477-3501.

Sewell, R. J. (1988). Late Miocene volcanic stratigraphy of central Banks Peninsula, Canterbury, New Zealand. *New Zealand Journal of Geology and Geophysics* **31**, 41-64.

Sewell, R. J., Hobden, B. J., Weaver, S. D. (1993). Mafic and ultramafic mantle and deep crustal xenoliths from Banks Peninsula, South Island, New Zealand. *New Zealand Journal of Geology and Geophysics* **36**, 223 - 231.

Sewell, R. J., Weaver, S. D., Reay, M. B. (1992). Geology of Banks Peninsula. *1:100,000 Geological Map 3. 1 sheet*. Lower Hutt, New Zealand: Institute of Geological and Nuclear Sciences.

Shaw, D. M. (1970). Trace element fractionation during anatexis. *Geochimica et Cosmochimica Acta* **34**, 237-243.

Stern, T., Okaya, D., Kleffmann, S., Scherwath, M., Henrys, S., Davey, F. (2007). Geophysical exploration and dynamics of the Alpine Fault Zone. In: Okaya, D., Stern, T., Davey, F. (eds.) *A Continental Plate Boundary: Tectonics at South Island, New Zealand*. Washington, DC: AGU, 207-233.

Sun, C. & Liang, Y. (2012). Distribution of REE between clinopyroxene and basaltic melt along a mantle adiabat: Effects of major element composition, water, and temperature. *Contributions to Mineralogy and Petrology* **163**, 807-823.

Sun, C. & Liang, Y. (2013). The importance of crystal chemistry on REE partitioning between mantle minerals (garnet, clinopyroxene, orthopyroxene, and olivine) and basaltic melts. *Chemical Geology* **358**, 23-36.

Sun, C. & Liang, Y. (2014). An assessment of subsolidus re-equilibration on REE distribution among mantle minerals olivine, orthopyroxene, clinopyroxene, and garnet in peridotites. *Chemical Geology* **372**, 80-91.

Sutherland, R. (1995). The Australia-Pacific boundary and Cenozoic plate motions in the SW Pacific: Some constraints from Geosat data. *Tectonics* **14**, 819-831.

Sutherland, R. (1999). Basement geology and tectonic development of the greater New Zealand region: an interpretation from regional magnetic data. *Tectonophysics* **308**, 341-362.

Sweeney, R. J., Green, D. H., Sie, S. H. (1992). Trace and minor element partitioning between garnet and amphibole and carbonatitic melt. *Earth and Planetary Science Letters* **113**, 1-14.

Szabó, C. & Bodnar, R. J. (1995). Chemistry and origin of mantle sulfides in spinel peridotite xenoliths from alkaline basaltic lavas, Nógrád-Gömör Volcanic Field, northern Hungary and southern Slovakia. *Geochimica et Cosmochimica Acta* **59**, 3917-3927.

Takazawa, E., Frey, F. A., Shimizu, N., Obata, M. (2000). Whole rock compositional variations in an upper mantle peridotite (Horoman, Hokkaido, Japan): Are they consistent with a partial melting process? *Geochimica et Cosmochimica Acta* **64**, 695-716.

Taylor, W. R. (1998). An experimental test of some geothermometer and geobarometer formulations for upper mantle peridotites with application to the thermobarometry of fertile lherzolite and garnet websterite. *Neues Jahrbuch fuer Mineralogie: Abhandlungen* **172**, 381-408.

Timm, C., Hoernle, K., Van Den Bogaard, P., Bindeman, I., Weaver, S. (2009). Geochemical evolution of intraplate volcanism at Banks Peninsula, New Zealand: Interaction between asthenospheric and lithospheric melts. *Journal of Petrology* **50**, 989-1023.

Timm, C., Hoernle, K., Werner, R., Hauff, F., den Bogaard, P. v., White, J., Mortimer, N., Garbe-Schönberg, D. (2010). Temporal and geochemical evolution of the Cenozoic intraplate volcanism of Zealandia. *Earth Science Reviews* **98**, 38-64.

Tulloch, A. J. & Nathan, S. (1990). Spinel harzburgite xenoliths in alkali basalt and camptonite from North Westland and Southeast Nelson, New Zealand. *New Zealand Journal of Geology and Geophysics* **33**, 529-534.

Walker, R. J., Carlson, R. W., Shirey, S. B., Boyd, F. R. (1989). Os, Sr, Nd, and Pb isotope systematics of southern African peridotite xenoliths: Implications for the chemical evolution of subcontinental mantle. *Geochimica et Cosmochimica Acta* **53**, 1583-1595.

Wallace, R. C. (1975). Mineralogy and petrology of xenoliths in a diatreme from south Westland, New Zealand. *Contributions to Mineralogy and Petrology* **49**, 191-199.

Walter, M. J. (2003). Melt extraction and compositional variability in the mantle lithosphere. In: Carlson, R. W. (ed.) *Treatise of Geochemistry*. Amsterdam, Netherlands: Elsevier, 363-394.

Watson, E. B. & Green, T. H. (1981). Apatite/liquid partition coefficients for the rare earth elements and strontium. *Earth and Planetary Science Letters* **56**, 405-421.

Wells, P. R. A. (1977). Pyroxene thermometry in simple and complex systems. *Contributions to Mineralogy and Petrology* **62**, 129-139.

Witt-Eickschen, G. & O'Neill, H. S. C. (2005). The effect of temperature on the equilibrium distribution of trace elements between clinopyroxene, orthopyroxene, olivine and spinel in upper mantle peridotite. *Chemical Geology* **221**, 65-101.

Wittig, N., Pearson, D. G., Baker, J. A., Duggen, S., Hoernle, K. (2010). A major element, PGE and Re-Os isotope study of Middle Atlas (Morocco) peridotite xenoliths: Evidence for coupled introduction of metasomatic sulphides and clinopyroxene. *Lithos* **115**, 15-26.

Wood, B., J. & Virgo, D. (1989). Upper mantle oxidation state: Ferric iron contents of lherzolite spinels by $^{57}$Fe Mössbauer spectroscopy and resultant oxygen fugacities. *Geochimica et Cosmochimica Acta* **53**, 1277-1291.

Woodland, A. B. & Koch, M. (2003). Variation in oxygen fugacity with depth in the upper mantle beneath the Kaapvaal craton, Southern Africa. *Earth and Planetary Science Letters* **214**, 295-310.

Woodland, A. B., Kornprobst, J., Tabit, A. (2006). Ferric iron in orogenic lherzolite massifs and controls of oxygen fugacity in the upper mantle. *Lithos* **89**, 222-241.

Workman, R. K. & Hart, S. R. (2005). Major and trace element composition of the depleted MORB mantle (DMM). *Earth and Planetary Science Letters* **231**, 53-72.

Wright, J. B. (1966). Olivine nodules in a phonilite of the East Otago alkaline province, New Zealand. *Nature* **5035**, 519.

Wright, J. B. (1968). Contributions to the volcanic succession and petrology of the Auckland Islands, New Zealand. III. Minor intrusives on the Ross volcano. *Transactions of the Royal Society of New Zealand* **6**, 1-11.

Yao, L., Sun, C., Liang, Y. (2012). A parameterized model for REE distribution between low-Ca pyroxene and basaltic melts with applications to REE partitioning in low-Ca pyroxene along a mantle adiabat and during pyroxenite-derived melt and peridotite interaction. *Contributions to Mineralogy and Petrology* **164**, 261-280.

Yaxley, G. M., Crawford, A. J., Green, D. H. (1991). Evidence for carbonatite metasomatism in spinel peridotite xenoliths from western Victoria, Australia. *Earth and Planetary Science Letters* **107**, 305-317.

Yaxley, G. M., Green, D. H., Kamenetsky, V. (1998). Carbonatite metasomatism in the southeastern Australian lithosphere. *Journal of Petrology* **39**, 1917-1930.

## Figure Captions

*Figure 1*: Photomicrographs of New Zealand mantle xenoliths. (a) Lherzolite xenolith (WFP-2) from the Fortification Peak locality, which is ca. 8 cm across exposed in aphyric basalt. (b) Wet cut-surface of the largest xenolith (OU45852) in this suite (ca. 50 cm across) from Trig L, Waitaha domain. Note: the minimal weathering rind on the sample. (c) Small equigranular dunite xenolith (NGB-4) with disseminated idiomorphic chromite from Ngatutura Point, North Island. (d) Protogranular lherzolite (OU45852) contains abundant large ol, opx and cpx (ca. 4-8 mm) and rare (ca. 1.5 %) light brown spinels blebs. Alteration is limited to cracks between grains. (e) Equigranular olivine harzburgite (WFP-11) which is dominated by recrystallised ol crystals ≤ 1 mm across although a large relict opx up to 4 mm long is observed. (f) Intensely altered lherzolite from Pilot Point (DPP-5), the sample contains large opx and sp, with smaller cpx crystals. Although intensely altered by iron-oxyhydroxides ± calcite ± talc although domains of fresh olivine remain. (g) Cr-rich spinel, which has formed a symplectite with olivine in a partially altered region of sample P80180 (Ohira Bay, Chatham Islands). (h) Al-rich spinel with symplectite-like texture (WTL-1) in contact with all three silicate phases. Note: the sharp contact between the xenolith and the basalt.

*Figure 2:* Sulfides in New Zealand mantle xenoliths. (a-e, i) Reflected light photomicrographs. (f-h, j-l) false colour electron microprobe element distribution maps (a) Sulfide bleb ca. 40 μm in diameter with a core of pentlandite (pnt) and rim of pyrrhotite (po). (b) Trail of small (< 10 μm) secondary sulfides composed of pentlandite (pnt) and chalcopyrite (cp). (c) Small (10 to 20 μm) secondary sulfides comprising pentlandite (pnt) and chalcopyrite (cp). (d) Small (<10 to 20 μm) secondary Ni-rich pentlandite-like phase (pnt) in altered olivine. (e) Two sulfide blebs, exsolved from mono sulfide solution (mss), comprising chalcopyrite (cp), pentlandite (pnt) and bornite (bn) within olivine. (f-h) Cu, Ni and Fe maps of sulfides in image e. (i) Large (ca. 100 μm) sulfide grain containing pentlandite (pnt), chalcopyrite (cp) and minor magnetite (mgt). (j-l) Cu, Ni and Fe maps of sulfides in image i.

*Figure 3*: Chemical variations in olivine and other mineral phases in New Zealand mantle xenoliths. Mantle xenoliths are divided into three groups: (1) Waitaha domain (circles); (2) Chatham Islands (squares); and (3) all other localities (diamonds) based on Re-Os isotopic characteristics (McCoy-West *et al.*, 2013). Comparative data fields are taken from Ionov *et al.* (2005) and references therein. (a-b) Forsterite content of olivine versus Cr# of spinel. The pristine fertile mantle (Ionov, 2007) has the following composition: Fo = 89.2; $Cr\#_{(Sp)} = 0.077$. (a) Error bars are shown for samples with variation in $Cr\#_{(Sp)} \geq 0.02$ (1σ). (b) Individual olivine analyses (open symbols) are plotted for samples with heterogeneous olivine compositions (Fo > ±0.08 %; 1σ). Three traverses were conducted across the zoned olivines in MSI33B, resulting in the abundance of data points. (c-d) Forsterite content of olivine versus $MnO_{(ol)}$ and the $Al_2O_{3(cpx)}$, respectively. Regressions are through samples from the Waitaha domain (excluding wehrlite WRR-6).

*Figure 4*: Chemical variation of clinopyroxene in Zealandian mantle xenoliths. Symbols are the same as Fig. 3. (a-b) Plots of $TiO_2$ and $Cr_3O_2$ versus $Na_2O$ contents. Arrows show the melting trend for abyssal peridotites (Hellebrand *et al.*, 2001), and those inferred for 'fluid' (high Na >2 wt %, low Ti) and 'melt' (high Ti, low to moderate Na) metasomatism (Ionov *et al.*, 2005). Comparative data fields are taken from Ionov *et al.* (2005) and references therein. (c-f) Plots clinopyroxene $Al_2O_3$ content versus Sc, Yb, Dy and Th, respectively. Regressions are through samples from the Waitaha domain. Primitive mantle concentrations are for clinopyroxene calculated to be in equilibrium with the primitive mantle of Palme & O'Neill (2003).

*Figure 5*: Clinopyroxene trace element compositions of New Zealand mantle xenoliths. (a-c) Primitive mantle-normalised average rare earth element compositions of samples from the Waitaha domain ($n = 24$), the rest of New Zealand ($n = 3$) and the Chatham Islands ($n = 6$). Representative primitive mantle-normalised clinopyroxene rare earth element (d-i) and multi-element (j-o) patterns. n is the number of individual crystals analysed from each sample. Normalising values are from Palme & O'Neill (2003). (f, l)

orthopyroxene (dark lines) data from sample DPP-2 are also shown. The dotted lines represent the composition of clinopyroxene in equilibrium with the residue after 0-25 % peritectic melting (presented herein). The samples show the effects of increasing amounts of metasomatism (i.e. d-i). Clinopyroxene trace element patterns for individual samples available in E-Appendix 1.

*Figure 6*: Plots of selected whole-rock major element data versus $Al_2O_3$ content. Symbols are the same as Fig. 3, except samples with excess pyroxene in their calculated modal compositions (see Fig A1.2; half-filled symbols); and samples with elevated CaO contents (>4 wt %; Table 3), from the Pilot Point locality (white circles) are distinguished. Comparative data (triangles) is from a relatively fertile suite of mantle xenoliths from Mongolia (Ionov, 2007, Ionov & Hofmann, 2007). The red shaded area represents the Horoman ophiolite (Takazawa *et al.*, 2000), a sequence of variably melt-depleted peridotites. Primitive mantle (PM; black square) values ± 1σ errors are taken from Palme & O'Neill (2003). (a,c) Lines show evolution of experimental residues at 1 GPa after up to 40 % batch melting (Herzberg, 2004). Elevated $FeO_{(T)}$ and $TiO_2$ contents cannot be produced by partial melting and are inferred to be refertilisation.

*Figure 7*: Plots showing the whole-rock variability of selected chondrite-normalised (Palme & O'Neill, 2003) refractory lithophile elements versus MgO content . Symbols are the same as Fig. 6. (a-i) Primitive mantle (PM; Palme & O'Neill, 2003) and the depleted MORB mantle (DMM; Workman & Hart, 2005) are shown for comparison. Graphs illustrate the changes in behaviour with the increasing incompatibility of the elements. (a-e) Regressions are through samples from the Waitaha domain (excluding olivine websterites; DPP-6 and MSI79C).

*Figure 8*: Whole rock rare earth element and multi-element primitive mantle-normalised (Palme & O'Neill, 2003) patterns of Zealandian mantle xenoliths. (a-b) Rare earth element plots of samples from the Waitaha domain ($n$ = 23), and the rest of New Zealand ($n$ = 6) and the Chatham Islands ($n$ = 6), respectively. Three representative locations are

shown: (c-d) Five Forks and Stoddard, Waitaha domain; (e-f) Trig L, Waitaha domain; (g-h) Ohira Bay, Chatham Islands. The dotted lines represent the composition of the mantle restite after 0-25 % peritectic melting (presented herein). (i-j) Note the change in scale. Comparative compositions of average Cape Verde oceanic calico-carbonatites (Hoernle *et al.*, 2002), small degree intraplate basalts from New Zealand (range represents ca. 2-3 % melting; McCoy-West *et al.*, 2010) and a southeast Australian apatite-bearing wehrlite (Yaxley *et al.*, 1998).

*Figure 9*: Whole rock primitive upper mantle-normalised (Becker *et al.*, 2006) platinum group element plots of New Zealand mantle xenoliths. Samples are divided on the basis of locality from north to south: (a-c) other New Zealand; (d) Chatham Islands; (e-i) Waitaha domain. Xenoliths from distinct localities within the same panel have different symbols.

*Figure 10*: (a-c) Osmium, Pt and Re whole rock concentrations versus Ir (ppb), respectively. Regression lines shown are for the Waitaha domain xenoliths. (d-e) Chondrite-normalised (Average CI; Horan *et al.*, 2003) Pd/Ir and Pt/Ir ratios versus $Al_2O_3$ content (an index of melt depletion). (f) Chondrite-normalised Pt/Ir plotted against initial $^{187}Os/^{188}Os$ calculated at the age of eruption (see McCoy-West *et al.*, 2013). Primitive mantle (PM; black square) values ± 1σ errors are taken from Becker *et al.* (2006), Palme & O'Neill (2003) and Meisel *et al.* (2001). (e-f) Red circles represent samples from the Trig L locality that define the Re-Os isochron presented in McCoy-West *et al.* (2013).

*Figure 11:* The degree of equilibrium within Zealandian mantle xenoliths. (a) Whole rock Mg# versus olivine forsterite content. Regression is for samples from the Waitaha domain ($r^2 = 0.92$) and is extremely close to the dotted 1:1 line. Samples from the Pilot Point locality with excess CaO in their whole rock powders (white circles) are excluded. (b) Contents of MnO, CaO and $Cr_2O_3$ in olivine versus equilibration temperature ($BKN_{opx}$; Ca in orthopyroxene; Brey & Köhler, 1990) for all xenoliths. As expected CaO and $Cr_2O_3$ contents show positive temperature dependence.

*Figure 12*: Calculated equilibration temperatures of mantle xenoliths from under New Zealand. The Ca in orthopyroxene geothermometer of Brey & Köhler (1990) ($BKN_{opx}$) has been utilised where possible, otherwise the olivine-clinopyroxene Ca exchange thermometer of Köhler & Brey (1990) has been used. Average temperatures with 1σ errors (shaded fields) are presented for localities with at least 3 xenoliths. Temperatures for harzburgites calculated using the $BKN_{opx}$ (shown with an arrow) are minimum estimates, as CaO is not buffered by clinopyroxene.

*Figure 13:* Oxygen fugacities in New Zealand mantle xenoliths were calculated relative to the fayalite magnetite-quartz buffer (ΔFMQ) using the ol-opx-sp barometer of O'Neill and Wall (1987) assuming perfect stoichiometry and a pressure of 1.3 GPa. (a) ΔFMQ versus Cr# of spinel. Error bars represent the uncertainty related to pressure window of the spinel stability field (0.8-1.8 GPa). (b) Histogram of ΔFMQ of Waitaha domain and Chatham Islands xenoliths, with the least abundant location shown at the front. Chatham Islands xenoliths appear slightly more oxidised.

*Figure 14*: A plot of whole-rock MgO versus Ca/Al an indicator of secondary clinopyroxene where Ca/Al >1.5 (Ionov *et al.*, 2005). Symbols are the same as Fig. 4, except that samples with FeO >9 wt % or Ca/Al >1.5 are hollow (i.e. those considered to have experienced refertilisation).

*Figure 15:* Trace element concentrations and ratios of clinopyroxene from Zealandian mantle xenoliths. Samples with distinctive metasomatic signatures have been plotted separately (e.g. WRR-1; Fig. 5). All clinopyroxene (diamonds) represents the complete dataset of LA-ICP-MS analyses ($n$ = 289). Comparative data: apatite bearing (stars) are the average compositions of cpx within two apatite-bearing xenoliths from Kattothyrst (Scott *et al.*, 2014a); the purple field represent the variability observed in xenoliths within the Waitaha domain (Scott *et al.*, 2014b). Also shown is clinopyroxene in equilibrium with the primitive mantle (black square) and the effect of the removal of up to 5 % melt

in 1 % increments (red line) using the model herein. N = chondrite-normalised using the values of Palme and O'Neill (2003)

*Figure 16*: Comparison of various models for constraining the amount of partial melting in mantle residues. Symbols are the same as Fig. 3, with regressions calculated from Waitaha domain samples. F = the percentage of melt extracted from the residue. The shaded area around the 1:1 line represents a 2 % error. (a-b) The modal clinopyroxene content of the xenoliths versus $F_{(Yb\ in\ WR)}$ and $F_{(MgO)}$ (Niu, 1997), respectively. Samples excluded from the regressions are plotted white. (c) $F_{(MgO)}$ versus $F_{(Yb\ in\ WR)}$. (d) $F_{(Yb\ in\ WR)}$ versus $F_{(Y\ in\ WR)}$. Symbols are distinguished based on their degree of REE enrichment through metasomatism ($Pr/Yb_N$: <1 (coloured); 1-3 (grey); >3 (white)). (e-f) $F_{(Yb\ in\ WR)}$ versus $F_{(Yb\ in\ Cpx)}$ and $F_{(Dy\ in\ Cpx)}$, respectively. Filled symbols have been corrected for subsolidus redistribution of elements, assuming an original locus of melting at 1300 °C at 1.5 GPa using experimental data (Falloon *et al.*, 1999) and stoichiometric redistribution CaO and therefore Dy or Yb between opx and cpx (see text), while hollow symbols represent F calculated using the measured concentrations in cpx. Dotted lines are regressions through the original data. Prior to correction for the subsolidus redistribution, HREE in cpx significantly underestimates the amount of melting that fertile samples have undergone. (g-h) $F_{(Yb\ in\ WR)}$ and $F_{(MgO)}$, respectively versus $F_{(Cr\#\ in\ Sp)}$ (Hellebrand *et al.*, 2001) . $F_{(Cr\#\ in\ Sp)}$ systematically underestimates the amount of partial melting.

*Figure 17*: Plots of the calculated amount of partial melting (F in percent: using whichever is the greater of $F_{(MgO)}$ or $F_{(Yb\ in\ WR)}$) versus chondrite-normalised (Horan *et al.*, 2003) Ru/Ir (a) and Pt/Ir (b) . Solid lines represent the depletion of S as partial melting proceeds from a primitive mantle with 250 ± 30 (Becker *et al.*, 2006) or 200 ± 40 ppm (Palme & O'Neill, 2003) S and a melt capacity of 1000 ppm S (Mavrogenes & O'Neill, 1999). The dotted line represents extraction of a melt with the maximum S content observed in primitive ocean floor basalts (i.e. MgO >8wt %; S = 1197 ppm; Jenner & O'Neill, 2012). The calculated degree of partial melting in sample DPP-2 (Fo = 91.2) is considered to be underestimated due to pyroxene excess in the whole-rock powder and

has been increased accordingly. $Ru/Ir_N$ remains stable to high degrees of partial melting as these elements form refractory alloys, whereas $Pt/Ir_N$ begins to drop rapidly at ca. 20 % melting as S becomes exhausted and Pt readily enters the melt phase.

*Figure 18*: Whole-rock $^{187}Re/^{188}Os$ (a) and $Al_2O_3$ (b) versus $^{187}Os/^{188}Os_{(i)}$ (calculated for the time of eruption) for Zealandian mantle xenoliths. Ages represent Re depletion ages and are calculated using the parameters presented in McCoy-West *et al.* (2013). Symbols are the same as Fig. 4, except samples from Fortification Peak are distinguished separately (triangles). Samples excluded from the regressions are plotted white. (a) A strong correlation is observed between $^{187}Os/^{188}Os$ and $^{187}Re/^{188}Os$ for samples within the Waitaha domain ($r^2 = 0.851$; $n = 12/17$). The intercept age of this robust regression is 1.99 ± 0.21 Ga and is within error of the 'errorchron' age (2.12 ± 0.57 Ga; Ludwig, 2008) calculated from the slope of this regression. Five samples have been excluded: four of these are small xenoliths (e.g. DPP-6; MSI79C; MSI20C; MSI20G) that are susceptible to the nugget effect; the final sample WFP-1 has disturbed Re/Os systematics (i.e. Os loss) with an $^{187}Os/^{188}Os_{(i)}$ greater than the primitive mantle ($^{187}Os/^{188}Os = 0.1296 \pm 8$; Meisel *et al.*, 2001). (b) A slightly weaker correlation is observed between $Al_2O_3$ and $^{187}Os/^{188}Os$ ($r^2 = 0.716$; $n = 13/17$), providing an aluminochron Re extraction age ($Al_{0.60}$) of 1.91 ± 0.39 Ga.

## Table Captions

*Table 1: Petrographic summary of New Zealand mantle xenoliths, including calculated modal abundances and mineral compositions.*

[1]Rock types are based on the classification of Le Bas & Streckeisen (1991) and use calculated modal abundances. Values in parentheses are based on visual estimates. [2]Modal abundances of phases were calculated using least squares regressions with errors calculated using the Deming method (see E-Appendix 1 for further details). [3]Abundance of discrete sulfide grains (≥2 μm) was estimated by visual inspection of a standard polished thin section. [4]Errors (1σ) are based on repeat analyses of multiple grains within

a single sample (generally *n* = 8-14). # = Sample contains heterogeneous olivine (i.e. Fo ±0.15 %). ^ = Sample contains heterogeneous spinel (i.e. Cr# ± 0.025). * = Modal composition may not be representative due to small xenolith size. Fo =100 x (Mg/(Mg + Fe)); Cr# = Cr/(Cr + Al). dun: dunite; hzb: harzburgite; lhz: lherzolite; Ol web: olivine websterite; whr: wehrlite; n.f. none found. Complete data are available in E-Appendix 2.

*Table 2: Average LA-ICP-MS trace element analyses (ppm) of clinopyroxene and orthopyroxene from New Zealand mantle xenoliths.*

*n* = the number of individual crystals that comprise the average composition. n.m. not measured; b.d. below detection; cpx: clinopyroxene; opx: orthopyroxene. # Sample P80353 is a gabbroic xenolith from the Chatham Islands. Complete data are available in E-Appendix 3.

*Table 3: Whole rock major, trace and platinum group element concentrations of New Zealand mantle xenoliths.*

*n* = the number of line analysis on the same glass disks that comprise the average composition. Errors on trace elements data (1σ) are on the last integer and based on replicate analyses of the same fused glass disk. LOI: Loss on ignition; dun: dunite; hzb: harzburgite; lhz: lherzolite; Ol web: olivine websterite; whr: wehrlite; n.m. not measured. [1] Whole-rock major element data have been recalculated on anhydrous basis assuming all Fe is FeO from the values presented in the online supplement of McCoy-West *et al.* (2013). [2] Replicate analysis of the same solution. [3] Analyses of second glass disk prepared in an identical manner. [4] Trace element data should be interpreted with caution due to seawater infiltration. * Re, Os and $^{187}Os/^{188}Os_{(i)}$ (initial $^{187}Os/^{188}Os$ calculated at the time of eruption) are taken from McCoy-West *et al.* (2013). Errors on platinum group element concentration data are <0.1 %. Ratios have been chondrite-normalised based on values in Palme and O'Neill (2003) and Horan *et al.* (2003).

*Table 4: A comparison of several models for estimating the degree of melt depletion in Zealandian xenoliths.*

$F_{(MgO)}$ is calculated using $F = -1.234 + (3.249x10^{-2} \times MgO)$ (Niu, 1997), which assumes a fertile mantle with 38.3 wt % MgO. $F_{(Cr\# \text{ in } Sp)}$ is calculated using $F = (10 \times \ln(Cr\#)) + 24$ (Hellebrand *et al.*, 2001), numbers in parentheses are from samples at higher Cr# than the original calibration (i.e. Cr# >0.6). $F_{(Yb \text{ in } WR)}$, $F_{(Y \text{ in } WR)}$ $F_{(Yb \text{ in } Cpx)}$ and $F_{(Dy \text{ in } Cpx)}$ are based on the partial melting model herein. Using the non-modal batch melting equation of Shaw (1970) and assuming an initial modal mineralogy of: ol = 0.506; opx = 0.281; cpx = 0.189; sp = 0.025, undergoing peritectic melting in the following proportions: ol = -0.24; opx = 0.33; cpx = 0.83; sp = 0.08 (Robinson *et al.*, 1998) and utilising an up to date compilation of partition coefficients (Table A1.8; Ionov *et al.*, 2002, McDade *et al.*, 2003, Sun & Liang, 2012, Sun & Liang, 2013, Yao *et al.*, 2012). Further details of the melting model are presented in E-Appendices 1 and 4. Numbers in parentheses are those calculated prior to correction for subsolidus exchange between cpx and opx. Square brackets show the amount of Yb and Dy that would have been present in cpx at the locus of melting. n.m. not measured; c.n.p. calculation not possible.

*Table 1: Petrographic summary of New Zealand mantle xenoliths, including calculated modal abundances and mineral compositions.*

| Sample | Locality | Rock[1] Type | Modal Composition (%)[2] Ol | Opx | Cpx | Sp | MSWD | Sulf[3] *n*= | Olivine[4] Fo (%) | $MnO_{Ol}$ (wt %) | $CaO_{Ol}$ (wt %) | $Al_2O_{3\ Cpx}$ (wt %) | $TiO_{2\ Cpx}$ (wt %) | $Na_2O_{Cpx}$ (wt %) | Spinel[4] Cr# | $TiO_{2\ Sp}$ (wt %) |
|---|---|---|---|---|---|---|---|---|---|---|---|---|---|---|---|---|
| **North Island** | | | | | | | | | | | | | | | | |
| NGB-3 | Ngatutura | whr | 91.5 ±0.4 | -- | 7.2 ±0.4 | 1.3 ±0.1 | 9.21 | 16 | 89.75 ±0.06 | 0.171 | 0.071 | 0.37 | 0.03 | 0.24 | 0.820 ±0.015 | 0.43 |
| NGB-4# | " | dun | 97.6 ±0.1 | -- | 0.9 ±0.1 | 1.5 ±0.1 | 0.17 | n.f. | 92.18 ±0.28 | 0.124 | 0.033 | 1.78 | 0.04 | 1.15 | 0.808 ±0.005 | 0.12 |
| **South Island** | | | | | | | | | | | | | | | | |
| P43153b# | Canoe | (hzb) | (80.8) | (19.0) | -- | (0.2) | | 696 | 91.59 ±1.67 | 0.118 | 0.089 | -- | -- | -- | 0.612 ±0.003 | 0.02 |
| P45280# | Strauchon | hzb | 73.0 ±2.0 | 27.0 ±2.1 | -- | 0.02 ±0.2 | 2.39 | n.f. | 87.52 ±0.56 | 0.192 | 0.156 | -- | -- | -- | 0.614 ±0.024 | 0.31 |
| MSI33B#^ | Cookson | (hzb) | (75.0) | (22.5) | (2.3) | (0.2) | | n.f. | 91.68 ±0.54 | 0.175 | 0.111 | 2.21 | 0.98 | 0.71 | 0.801 ±0.001 | 0.22 |
| MSI33D# | " | (hzb) | (78.0) | (20.0) | (1.9) | (0.1) | | -- | 89.72 ±0.98 | 0.134 | 0.064 | -- | -- | -- | -- | -- |
| MSIK33C^ | " | (hzb) | (54.8) | (43.0) | (2.5) | (0.2) | | -- | 90.26 ±0.07 | 0.125 | 0.077 | 6.07 | 1.20 | 1.78 | 0.731 ±0.002 | 0.10 |
| *Waitaha domain* | | | | | | | | | | | | | | | | |
| MSI20C* | Stoddard | hzb | 64.6 ±2.0 | 33.8 ±2.1 | 1.3 ±0.2 | 0.3 ±0.1 | 11.9 | -- | 91.16 ±0.09 | 0.117 | 0.057 | 2.85 | 0.05 | 1.14 | 0.437 ±0.010 | 0.06 |
| MSI20G*^ | " | hzb | 55.9 ±2.0 | 42.3 ±2.3 | 1.4 ±0.7 | 0.4 ±0.1 | 15.5 | -- | 91.10 ±0.12 | 0.116 | 0.057 | 2.62 | 0.04 | 1.11 | 0.463 ±0.036 | 0.04 |
| MSI20H^ | " | hzb | (70.0) | (28.2) | (1.5) | (0.3) | | n.f. | 91.10 ±0.06 | 0.137 | 0.057 | 3.59 | 0.16 | 1.09 | 0.384 ±0.030 | 0.09 |
| FvF-1 | Five Forks | lhz | 60.7 ±1.8 | 27.2 ±2.2 | 10.8 ±0.6 | 1.3 ±0.2 | 2.10 | 52 | 90.15 ±0.04 | 0.146 | 0.056 | 6.37 | 0.25 | 1.44 | 0.126 ±0.006 | 0.05 |
| MSI79C* | Kakanui | Ol web | 37.8 ±2.2 | 54.2 ±2.5 | 7.5 ±0.6 | 0.5 ±0.3 | 0.34 | 540 | 89.90 ±0.09 | 0.131 | 0.084 | 7.19 | 0.34 | 1.69 | 0.128 ±0.004 | 0.11 |
| WTL-1 | Trig L | lhz | 63.3 ±1.9 | 24.9 ±2.1 | 9.6 ±0.5 | 2.1 ±0.2 | 0.51 | 16 | 90.17 ±0.06 | 0.129 | 0.054 | 5.43 | 0.24 | 0.99 | 0.145 ±0.004 | 0.06 |
| WTL-2 | " | hzb | 67.0 ±1.9 | 27.0 ±2.1 | 4.8 ±0.4 | 1.1 ±0.2 | 1.33 | 6 | 91.18 ±0.05 | 0.113 | 0.049 | 4.47 | 0.12 | 1.06 | 0.232 ±0.062 | 0.06 |
| WTL-3 | " | lhz | 71.4 ±1.9 | 17.7 ±2.1 | 9.4 ±0.5 | 1.5 ±0.2 | 1.78 | 35 | 89.52 ±0.06 | 0.134 | 0.039 | 5.39 | 0.26 | 0.92 | 0.134 ±0.09 | 0.06 |
| OU45852 | " | lhz | 68.8 ±1.8 | 18.8 ±2.1 | 10.7 ±0.6 | 1.7 ±0.2 | 1.15 | 5 | 90.24 ±0.04 | 0.141 | 0.065 | 5.92 | 0.21 | 1.06 | 0.126 ±0.005 | 0.05 |
| WRR-1# | Ram Rock | lhz | 77.9 ±2.0 | 13.7 ±2.1 | 6.9 ±0.4 | 1.4 ±0.2 | 0.80 | 152 | 90.39 ±0.27 | 0.122 | 0.052 | 3.76 | 0.07 | 0.75 | 0.198 ±0.022 | 0.13 |
| WRR-3 | " | lhz | 72.1 ±1.7 | 17.4 ±2.0 | 9.1 ±0.5 | 1.5 ±0.1 | 1.42 | 76 | 90.03 ±0.05 | 0.123 | 0.053 | 4.19 | 0.15 | 0.65 | 0.177 ±0.005 | 0.05 |
| WRR-5 | " | hzb | 81.6 ±1.8 | 12.9 ±1.9 | 4.4 ±0.3 | 1.1 ±0.1 | 1.31 | n.f. | 91.12 ±0.07 | 0.113 | 0.050 | 2.69 | 0.03 | 0.61 | 0.407 ±0.019 | 0.04 |
| WRR-6# | " | whr | 87.1 ±0.6 | -- | 12.6 ±0.6 | 0.3 ±0.1 | 54.0 | 4 | 89.26 ±0.56 | 0.198 | 0.043 | 0.65 | 0.02 | 1.19 | 0.730 | 0.09 |
| WRR-7 | " | hzb | 81.2 ±1.7 | 13.2 ±1.8 | 4.6 ±0.3 | 1.0 ±0.1 | 1.71 | 19 | 90.68 ±0.08 | 0.114 | 0.050 | 4.00 | 0.12 | 0.98 | 0.283 ±0.012 | 0.05 |
| WRR-9# | " | hzb | 70.1 ±2.1 | 24.4 ±2.2 | 4.9 ±0.4 | 0.5 ±0.1 | 6.5 | 118 | 90.43 ±0.45 | 0.127 | 0.036 | 2.54 | 0.10 | 1.39 | 0.631 ±0.017 | 0.10 |
| DPP-1 | Pilot Point | (lhz) | (54.5) | (26.0) | (18.0) | (1.5) | | -- | 89.72 ±0.03 | 0.116 | 0.086 | 6.99 | 0.33 | 1.52 | 0.111 ±0.002 | 0.10 |
| DPP-2# | " | (hzb) | (76.0) | (19.0) | (4.0) | (1.0) | | n.f. | 91.34 ±0.20 | 0.114 | 0.085 | 3.06 | 0.06 | 1.13 | 0.473 ±0.006 | 0.11 |
| DPP-3 | " | lhz | 58.1 ±1.9 | 23.4 ±2.4 | 17.0 ±0.9 | 1.5 ±0.2 | 1.01 | n.f. | 89.66 ±0.05 | 0.130 | 0.080 | 6.94 | 0.47 | 1.60 | 0.109 ±0.003 | 0.13 |
| DPP-5 | " | (lhz) | (57.5) | (25.0) | (16.0) | (1.5) | | n.f. | 89.42 ±0.12 | 0.126 | 0.088 | 7.17 | 0.41 | 1.57 | 0.109 ±0.003 | 0.12 |
| DPP-6*# | " | Ol web | 37.1 ±2.0 | 50.2 ±2.4 | 11.3 ±0.7 | 1.4 ±0.2 | 3.88 | 8 | 89.43 ±0.20 | 0.134 | 0.088 | 7.06 | 0.54 | 1.50 | 0.161 ±0.004 | 0.25 |
| WFP-1 | Fortification | hzb | 78.3 ±1.8 | 17.7 ±1.9 | 3.0 ±0.2 | 1.0 ±0.1 | 0.41 | n.f. | 91.76 ±0.14 | 0.117 | 0.067 | 3.23 | 0.03 | 0.74 | 0.303 ±0.020 | 0.02 |
| WFP-2 | Peak | lhz | 70.8 ±1.9 | 20.3 ±2.1 | 7.3 ±0.4 | 1.7 ±0.2 | 0.47 | 52 | 89.90 ±0.06 | 0.132 | 0.079 | 4.52 | 0.24 | 0.80 | 0.174 ±0.011 | 0.07 |
| WFP-4 | " | hzb | 78.8 ±1.9 | 18.4 ±2.0 | 2.1 ±0.2 | 0.7 ±0.1 | 1.74 | 94 | 91.05 ±0.08 | 0.114 | 0.076 | 1.87 | 0.01 | 0.45 | 0.430 ±0.017 | 0.03 |
| WFP-5 | " | hzb | 77.5 ±1.7 | 18.7 ±1.8 | 2.9 ±0.2 | 0.9 ±0.1 | 0.93 | 4 | 91.72 ±0.08 | 0.108 | 0.035 | 2.70 | 0.04 | 0.63 | 0.358 ±0.017 | 0.03 |
| WFP-7 | " | hzb | 75.6 ±1.9 | 18.4 ±2.0 | 4.9 ±0.3 | 1.1 ±0.1 | 0.31 | 32 | 90.72 ±0.06 | 0.122 | 0.072 | 3.24 | 0.10 | 0.64 | 0.279 ±0.012 | 0.05 |
| WFP-8 | " | lhz | 66.5 ±2.1 | 23.4 ±2.3 | 8.4 ±0.5 | 1.7 ±0.3 | 0.62 | 32 | 90.36 ±0.06 | 0.131 | 0.086 | 3.14 | 0.04 | 0.48 | 0.205 ±0.007 | 0.02 |
| WFP-11 | " | hzb | 82.1 ±1.9 | 15.8 ±2.1 | 1.6 ±0.5 | 0.5 ±0.1 | 0.36 | 6 | 91.57 ±0.15 | 0.108 | 0.027 | 2.25 | 0.00 | 0.58 | 0.449 ±0.023 | 0.02 |
| **Chatham Islands** | | | | | | | | | | | | | | | | |
| P80180# | Ohira Bay | hzb | 73.2 ±1.7 | 23.2 ±1.8 | 3.3 ±0.3 | 0.4 ±0.1 | 1.84 | 13 | 90.92 ±0.21 | 0.125 | 0.081 | 2.31 | 0.36 | 0.81 | 0.557 ±0.006 | 0.32 |
| P80290 | " | hzb | 75.2 ±1.6 | 20.7 ±1.7 | 3.7 ±0.3 | 0.4 ±0.1 | 0.68 | n.f. | 90.75 ±0.08 | 0.116 | 0.074 | 2.10 | 0.01 | 0.75 | 0.525 ±0.019 | 0.05 |
| P80291#^ | " | hzb | 79.2 ±1.9 | 16.6 ±2.1 | 3.5 ±0.4 | 0.6 ±0.1 | 0.65 | n.f. | 90.86 ±0.30 | 0.128 | 0.064 | 2.69 | 0.09 | 1.47 | 0.569 ±0.047 | 0.13 |
| P80354a#^ | Snake | hzb | 75.5 ±1.9 | 22.0 ±2.0 | 1.9 ±0.3 | 0.6 ±0.1 | 2.03 | n.f. | 91.41 ±0.61 | 0.113 | 0.037 | 2.21 | 0.07 | 0.71 | 0.498 ±0.075 | 0.19 |
| P80354b^ | Gully | hzb | 82.6 ±2.0 | 14.7 ±2.1 | 2.1 ±0.2 | 0.5 ±0.2 | 1.77 | n.f. | 91.61 ±0.13 | 0.122 | 0.037 | 2.92 | 0.22 | 0.72 | 0.411 ±0.035 | 0.15 |
| P80354c#^ | " | lhz | 78.2 ±2.0 | 16.2 ±2.1 | 5.1 ±0.3 | 0.5 ±0.2 | 0.81 | 58 | 90.89 ±0.35 | 0.129 | 0.050 | 4.01 | 0.72 | 0.67 | 0.420 ±0.141 | 0.30 |

*Table 2: Average LA-ICP-MS trace element compositions (ppm) of clinopyroxene and orthopyroxene.*

| Sample: | NGB-3 | NGB-4 | P43153b | MSI33D | MSIK33C | MSI20C | MSI20G | MSI20G |
|---|---|---|---|---|---|---|---|---|
| Locality: | Ngatutara | Ngatutara | Canoe | Cookson | Cookson | Stoddard | Stoddard | Stoddard |
| Phase: | cpx | cpx | opx | opx | cpx | cpx | cpx | opx |
| $SiO_2$ (wt %) | 55.46 | 55.08 | 55.49 | 57.68 | 52.25 | 54.59 | 54.50 | 57.17 |
| CaO (wt %) | 24.42 | 21.44 | 0.88 | 0.55 | 18.64 | 21.46 | 21.48 | 0.77 |
| *n* = | *14* | *1* | *12* | *6* | *7* | *12* | *8* | *7* |
| Li (ppm) | 3.84 | 7.72 | 2.68 | 1.90 | 6.96 | 3.43 | 3.74 | 3.84 |
| Sc | 111 | 116 | 18.7 | 7.79 | 57.9 | 85.6 | 88.8 | 12.8 |
| Ti | 156 | 86.4 | 1.43 | 571 | 8194 | 276 | 263 | 68.5 |
| V | n.m. | n.m. | n.m. | n.m. | n.m. | n.m. | n.m. | n.m. |
| Cr | 2112 | 10669 | 4910 | 3672 | 11463 | 6805 | 6168 | 1967 |
| Mn | 423 | 523 | 925 | 1243 | 712 | 519 | 548 | 1189 |
| Co | 17.6 | 16.8 | 58.1 | 57.5 | 23.2 | 19.7 | 20.2 | 117.4 |
| Ni | 240 | 217 | 915 | 817 | 429 | 364 | 379 | 2444 |
| Zn | 6.29 | 3.67 | 29.1 | 62.7 | 13.3 | 7.00 | 7.36 | 45.6 |
| Ga | 0.628 | 2.79 | 0.885 | 5.55 | 6.99 | 1.68 | 1.81 | 0.863 |
| Rb | 0.0004 | 0.047 | 0.001 | 0.027 | 0.177 | 0.021 | 0.003 | 0.001 |
| Sr | 40.1 | 447 | 0.113 | 3.37 | 114 | 95.4 | 124 | 0.157 |
| Y | 0.965 | 2.21 | 0.002 | 0.885 | 16.0 | 2.63 | 2.58 | 0.110 |
| Zr | 0.042 | 19.6 | 0.006 | 7.3 | 238 | 12.2 | 15.0 | 0.390 |
| Nb | 0.005 | 0.077 | 0.010 | 0.233 | 0.477 | 0.168 | 0.129 | 0.006 |
| Mo | 0.010 | 0.239 | 0.027 | 0.084 | 0.023 | 0.080 | 0.071 | 0.040 |
| Ba | 0.047 | 0.092 | 0.001 | 0.635 | 0.894 | 0.161 | 0.038 | 0.0002 |
| La | 0.007 | 14.5 | 0.012 | 0.328 | 2.66 | 9.61 | 12.7 | 0.009 |
| Ce | 0.015 | 20.7 | 0.028 | 0.603 | 11.2 | 13.4 | 18.6 | 0.029 |
| Pr | 0.003 | 1.60 | 0.002 | 0.065 | 2.27 | 1.08 | 1.50 | 0.006 |
| Nd | 0.043 | 3.74 | 0.004 | 0.277 | 14.1 | 3.02 | 3.93 | 0.023 |
| Sm | 0.046 | 0.354 | b.d. | 0.082 | 5.06 | 0.383 | 0.465 | 0.006 |
| Eu | 0.021 | 0.113 | 0.0002 | 0.032 | 1.78 | 0.139 | 0.167 | 0.003 |
| Gd | 0.113 | 0.306 | 0.0001 | 0.107 | 5.63 | 0.324 | 0.343 | 0.009 |
| Tb | 0.023 | 0.045 | 0.0003 | 0.022 | 0.792 | 0.052 | 0.055 | 0.002 |
| Dy | 0.179 | 0.296 | 0.0003 | 0.153 | 4.30 | 0.380 | 0.385 | 0.012 |
| Ho | 0.040 | 0.073 | b.d. | 0.033 | 0.667 | 0.089 | 0.088 | 0.003 |
| Er | 0.129 | 0.289 | 0.0005 | 0.104 | 1.49 | 0.312 | 0.317 | 0.015 |
| Tm | 0.019 | 0.054 | 0.0004 | 0.016 | 0.163 | 0.051 | 0.051 | 0.003 |
| Yb | 0.145 | 0.421 | 0.009 | 0.117 | 0.851 | 0.386 | 0.382 | 0.039 |
| Lu | 0.024 | 0.076 | 0.003 | 0.019 | 0.105 | 0.064 | 0.063 | 0.008 |
| Hf | 0.002 | 0.436 | 0.0003 | 0.199 | 11.7 | 0.107 | 0.173 | 0.007 |
| Ta | b.d. | 0.005 | 0.0002 | 0.018 | 0.064 | 0.034 | 0.029 | 0.000 |
| Pb | 0.276 | 2.92 | 0.005 | 0.015 | 0.075 | 0.650 | 0.699 | 0.004 |
| Th | 0.000 | 1.45 | 0.001 | 0.072 | 0.065 | 2.27 | 2.83 | 0.016 |
| U | 0.001 | 0.309 | 0.001 | 0.011 | 0.013 | 0.610 | 0.724 | 0.009 |

*Table 2: continued*

| Sample: | FvF-1 | MSI79C | WTL-1 | WTL-2 | WTL-3 | OU45852 | WRR-1 | WRR-3 |
|---|---|---|---|---|---|---|---|---|
| Locality: | Five Forks | Kakanui | Trig L | Trig L | Trig L | Trig L | Ram Rock | Ram Rock |
| Phase: | cpx | cpx | cpx | cpx | cpx | cpx | cpx | cpx |
| $SiO_2$ (wt %) | 52.34 | 53.17 | 53.09 | 53.78 | 53.13 | 53.88 | 54.17 | 53.58 |
| CaO (wt %) | 21.47 | 19.21 | 22.18 | 21.99 | 22.19 | 21.66 | 23.27 | 23.45 |
| *n* = | *16* | *11* | *9* | *9* | *8* | *11* | *8* | *9* |
| Li (ppm) | 5.90 | 8.49 | 13.9 | 21.0 | 9.74 | 1.18 | 6.31 | 6.00 |
| Sc | 64.8 | 63.4 | 66.0 | 70.0 | 65.6 | 63.1 | 71.8 | 70.8 |
| Ti | 1789 | 2275 | 1535 | 884 | 1720 | 1380 | 282 | 1025 |
| V | n.m. | n.m. | 260 | 237 | 264 | n.m. | 228 | 262 |
| Cr | 7602 | 5877 | 6069 | 8206 | 5668 | 6723 | 7844 | 6849 |
| Mn | 678 | 701 | 583 | 513 | 633 | 582 | 585 | 603 |
| Co | 21.5 | 22.8 | 17.9 | 17.2 | 19.0 | 19.5 | 18.5 | 21.0 |
| Ni | 389 | 393 | 317 | 322 | 319 | 336 | 352 | 354 |
| Zn | 7.38 | 8.72 | 4.78 | 5.08 | 5.42 | 7.42 | 6.21 | 10.0 |
| Ga | 3.89 | 3.91 | 2.57 | 2.11 | 2.90 | 2.78 | 1.59 | 2.43 |
| Rb | 0.007 | 0.015 | 0.004 | 0.009 | 0.006 | 0.002 | 0.005 | 0.007 |
| Sr | 26.3 | 89.2 | 4.51 | 24.7 | 0.463 | 0.899 | 13.8 | 9.57 |
| Y | 14.5 | 17.7 | 14.4 | 8.15 | 15.0 | 16.7 | 5.123 | 10.6 |
| Zr | 4.91 | 13.25 | 1.16 | 4.51 | 1.27 | 1.90 | 4.99 | 1.50 |
| Nb | 0.243 | 2.845 | 0.021 | 0.354 | 0.117 | 0.009 | 0.052 | 0.218 |
| Mo | 0.022 | 0.032 | 0.014 | 0.021 | 0.016 | 0.013 | 0.055 | 0.035 |
| Ba | 0.020 | 0.306 | 0.180 | 0.054 | 0.055 | 0.171 | 0.034 | 0.046 |
| La | 1.07 | 6.06 | 0.023 | 1.57 | 0.025 | 0.001 | 1.80 | 1.33 |
| Ce | 2.23 | 8.62 | 0.015 | 2.08 | 0.031 | 0.032 | 1.63 | 2.50 |
| Pr | 0.299 | 0.750 | 0.016 | 0.219 | 0.021 | 0.030 | 0.069 | 0.226 |
| Nd | 1.54 | 2.99 | 0.307 | 1.06 | 0.414 | 0.452 | 0.093 | 0.758 |
| Sm | 0.691 | 1.09 | 0.448 | 0.408 | 0.592 | 0.507 | 0.019 | 0.276 |
| Eu | 0.343 | 0.492 | 0.219 | 0.175 | 0.281 | 0.271 | 0.015 | 0.142 |
| Gd | 1.38 | 2.01 | 1.21 | 0.711 | 1.40 | 1.37 | 0.142 | 0.747 |
| Tb | 0.294 | 0.392 | 0.278 | 0.150 | 0.294 | 0.317 | 0.051 | 0.185 |
| Dy | 2.31 | 2.92 | 2.24 | 1.20 | 2.39 | 2.61 | 0.587 | 1.58 |
| Ho | 0.525 | 0.643 | 0.523 | 0.289 | 0.560 | 0.604 | 0.177 | 0.391 |
| Er | 1.65 | 1.98 | 1.70 | 0.985 | 1.78 | 1.94 | 0.688 | 1.28 |
| Tm | 0.240 | 0.281 | 0.237 | 0.146 | 0.243 | 0.282 | 0.113 | 0.190 |
| Yb | 1.61 | 1.86 | 1.65 | 1.01 | 1.72 | 1.90 | 0.818 | 1.25 |
| Lu | 0.233 | 0.265 | 0.236 | 0.151 | 0.248 | 0.273 | 0.130 | 0.187 |
| Hf | 0.150 | 0.520 | 0.172 | 0.184 | 0.213 | 0.201 | 0.022 | 0.071 |
| Ta | n.m. | 0.078 | 0.000 | 0.015 | 0.000 | 0.000 | 0.006 | 0.016 |
| Pb | 0.034 | 0.073 | 0.045 | 0.057 | 0.006 | 0.015 | 0.211 | 0.055 |
| Th | 0.178 | 0.480 | 0.000 | 0.128 | 0.014 | 0.000 | 3.20 | 0.305 |
| U | 0.055 | 0.121 | 0.000 | 0.115 | 0.051 | 0.000 | 0.839 | 0.098 |

*Table 2: continued*

| Sample: | WRR-5 | WRR-7 | WRR-9 | DPP-1 | DPP-2 | DPP-2 | DPP-3 | DPP-5 |
|---|---|---|---|---|---|---|---|---|
| Locality: | Ram Rock | Ram Rock | Ram Rock | Pilot Point | Pilot Point | Pilot Point | Pilot Point | Pilot Point |
| Phase: | cpx | cpx | opx | cpx | cpx | opx | cpx | cpx |
| $SiO_2$ (wt %) | 54.76 | 54.27 | 58.43 | 52.57 | 54.69 | 57.68 | 52.82 | 52.81 |
| CaO (wt %) | 23.71 | 22.97 | 0.50 | 20.23 | 21.39 | 0.88 | 20.61 | 20.02 |
| *n* = | *9* | *13* | *8* | *10* | *9* | *7* | *10* | *9* |
| Li (ppm) | 4.27 | 4.62 | 1.96 | 1.33 | 2.07 | 0.98 | 1.07 | 1.26 |
| Sc | 64.2 | 85.0 | 15.3 | 59.0 | 63.0 | 18.9 | 65.7 | 60.8 |
| Ti | 228 | 805 | 371 | 2324 | 331 | 132 | 3259 | 2870 |
| V | 190 | 241 | n.m. | 258 | 186 | n.m. | 263 | 272 |
| Cr | 7376 | 8487 | 4838 | 6456 | 8587 | 4720 | 6295 | 6111 |
| Mn | 553 | 568 | 1149 | 758 | 607 | 1004 | 688 | 771 |
| Co | 19.3 | 18.7 | 54.7 | 25.3 | 22.8 | 59.0 | 22.2 | 24.5 |
| Ni | 335 | 347 | 732 | 451 | 425 | 866 | 395 | 392 |
| Zn | 6.07 | 5.96 | 33.0 | 10.4 | 8.16 | 30.6 | 7.69 | 8.83 |
| Ga | 1.32 | 2.15 | 2.73 | 4.25 | 2.19 | 1.67 | 3.84 | 4.26 |
| Rb | 0.003 | 0.042 | 3.49 | 0.005 | 0.006 | 0.003 | 0.030 | 0.005 |
| Sr | 72.8 | 28.4 | 13.1 | 24.5 | 254 | 0.926 | 64.9 | 18.7 |
| Y | 2.40 | 8.46 | 0.784 | 18.4 | 4.42 | 0.342 | 21.0 | 18.7 |
| Zr | 3.43 | 11.8 | 2.91 | 15.7 | 14.3 | 0.796 | 30.1 | 14.1 |
| Nb | 0.149 | 0.095 | 1.75 | 0.233 | 1.29 | 0.106 | 0.199 | 0.154 |
| Mo | 0.038 | 0.025 | 0.176 | 0.034 | 0.093 | 0.046 | 0.018 | 0.020 |
| Ba | 0.479 | 0.103 | 3.49 | 0.049 | 0.155 | 0.007 | 0.021 | 0.043 |
| La | 5.33 | 2.89 | 1.31 | 1.531 | 13.38 | 0.040 | 0.804 | 0.115 |
| Ce | 8.19 | 4.24 | 2.23 | 2.35 | 25.0 | 0.107 | 3.02 | 0.710 |
| Pr | 0.813 | 0.391 | 0.207 | 0.332 | 2.561 | 0.014 | 0.601 | 0.248 |
| Nd | 3.04 | 1.588 | 0.695 | 2.17 | 9.22 | 0.071 | 3.81 | 2.24 |
| Sm | 0.583 | 0.511 | 0.114 | 1.13 | 1.54 | 0.022 | 1.61 | 1.29 |
| Eu | 0.199 | 0.220 | 0.039 | 0.513 | 0.523 | 0.009 | 0.691 | 0.568 |
| Gd | 0.548 | 0.839 | 0.102 | 2.08 | 1.21 | 0.031 | 2.59 | 2.26 |
| Tb | 0.081 | 0.168 | 0.017 | 0.408 | 0.155 | 0.006 | 0.487 | 0.432 |
| Dy | 0.480 | 1.33 | 0.118 | 3.08 | 0.888 | 0.044 | 3.59 | 3.20 |
| Ho | 0.090 | 0.304 | 0.026 | 0.671 | 0.161 | 0.011 | 0.778 | 0.692 |
| Er | 0.254 | 0.971 | 0.091 | 2.091 | 0.449 | 0.043 | 2.31 | 2.08 |
| Tm | 0.037 | 0.145 | 0.016 | 0.298 | 0.062 | 0.008 | 0.325 | 0.289 |
| Yb | 0.261 | 0.948 | 0.130 | 1.91 | 0.410 | 0.074 | 2.09 | 1.87 |
| Lu | 0.043 | 0.145 | 0.023 | 0.275 | 0.062 | 0.014 | 0.304 | 0.272 |
| Hf | 0.123 | 0.346 | 0.051 | 0.585 | 0.143 | 0.009 | 0.910 | 0.713 |
| Ta | 0.010 | 0.012 | 0.067 | 0.019 | 0.124 | 0.003 | 0.007 | 0.001 |
| Pb | 0.239 | 0.153 | 0.186 | 0.055 | 0.165 | 0.004 | 0.055 | 0.007 |
| Th | 0.359 | 0.434 | 0.532 | 1.291 | 0.781 | 0.012 | 0.028 | 0.010 |
| U | 0.337 | 0.219 | 0.141 | 0.272 | 0.231 | 0.007 | 0.005 | 0.004 |

*Table 2: continued*

| Sample: | DPP-6 | WFP-1 | WFP-2 | WFP-4 | WFP-5 | WFP-7 | WFP-8 | WFP-11 |
|---|---|---|---|---|---|---|---|---|
| Locality: | Pilot Point | Fort P | Fort P | Fort P | Fort P | Fort P | Fort P | Fort P |
| Phase: | cpx | cpx | cpx | cpx | cpx | cpx | cpx | cpx |
| $SiO_2$ (wt %) | 52.34 | 54.73 | 53.57 | 55.05 | 54.62 | 54.10 | 54.01 | 54.73 |
| CaO (wt %) | 19.95 | 23.36 | 22.94 | 23.85 | 23.93 | 23.44 | 23.63 | 23.90 |
| *n* = | *9* | *8* | *8* | *6* | *8* | *8* | *8* | *11* |
| Li (ppm) | 14.3 | 10.4 | 11.5 | 3.91 | 10.9 | 15.5 | 7.74 | 6.41 |
| Sc | 56.5 | 81.0 | 73.2 | 67.9 | 77.5 | 80.3 | 73.8 | 90.8 |
| Ti | 3755 | 168 | 1665 | 123 | 306 | 674 | 262 | 36.1 |
| V | 264 | 154 | 271 | 157 | 169 | 247 | 233 | 154 |
| Cr | 7696 | 7432 | 6495 | 4752 | 7361 | 6358 | 5669 | 6693 |
| Mn | 812 | 545 | 637 | 500 | 556 | 591 | 572 | 538 |
| Co | 25.0 | 18.2 | 19.3 | 19.0 | 19.5 | 19.4 | 20.0 | 18.5 |
| Ni | 411 | 321 | 327 | 364 | 352 | 346 | 372 | 335 |
| Zn | 10.3 | 5.48 | 5.44 | 5.65 | 5.57 | 5.51 | 5.82 | 6.05 |
| Ga | 5.51 | 1.65 | 2.71 | 0.934 | 1.23 | 1.75 | 1.44 | 1.15 |
| Rb | 0.007 | 0.006 | 0.003 | 0.088 | 0.006 | 0.021 | 0.025 | 0.255 |
| Sr | 48.7 | 136 | 22.1 | 13.8 | 19.9 | 26.6 | 0.294 | 104 |
| Y | 20.7 | 1.90 | 13.5 | 1.08 | 2.18 | 4.84 | 4.95 | 1.82 |
| Zr | 19.4 | 3.44 | 8.67 | 9.18 | 5.81 | 5.16 | 0.078 | 4.05 |
| Nb | 0.582 | 3.02 | 0.138 | 0.559 | 0.744 | 0.367 | 0.155 | 0.288 |
| Mo | 0.039 | 0.027 | 0.019 | 0.121 | 0.014 | 0.018 | 0.014 | 0.028 |
| Ba | 0.066 | 0.035 | 0.001 | 0.074 | 0.007 | 0.010 | 0.061 | 0.055 |
| La | 2.59 | 15.8 | 1.20 | 2.77 | 2.20 | 1.56 | 0.030 | 4.59 |
| Ce | 6.06 | 11.3 | 2.99 | 5.30 | 3.38 | 3.63 | 0.029 | 11.90 |
| Pr | 0.865 | 0.501 | 0.410 | 0.511 | 0.321 | 0.440 | 0.001 | 1.67 |
| Nd | 4.66 | 1.25 | 1.97 | 1.73 | 1.32 | 1.86 | 0.004 | 7.33 |
| Sm | 1.85 | 0.216 | 0.791 | 0.315 | 0.359 | 0.411 | 0.013 | 1.47 |
| Eu | 0.754 | 0.081 | 0.323 | 0.094 | 0.118 | 0.136 | 0.012 | 0.424 |
| Gd | 2.81 | 0.207 | 1.43 | 0.259 | 0.419 | 0.473 | 0.141 | 1.14 |
| Tb | 0.518 | 0.030 | 0.287 | 0.032 | 0.063 | 0.090 | 0.053 | 0.122 |
| Dy | 3.64 | 0.229 | 2.22 | 0.179 | 0.393 | 0.720 | 0.596 | 0.504 |
| Ho | 0.765 | 0.065 | 0.497 | 0.036 | 0.077 | 0.179 | 0.174 | 0.066 |
| Er | 2.25 | 0.268 | 1.55 | 0.140 | 0.236 | 0.612 | 0.646 | 0.132 |
| Tm | 0.309 | 0.050 | 0.222 | 0.025 | 0.036 | 0.098 | 0.107 | 0.017 |
| Yb | 1.95 | 0.412 | 1.45 | 0.229 | 0.267 | 0.691 | 0.748 | 0.140 |
| Lu | 0.272 | 0.072 | 0.211 | 0.038 | 0.045 | 0.107 | 0.117 | 0.026 |
| Hf | 0.791 | 0.084 | 0.346 | 0.232 | 0.185 | 0.199 | 0.002 | 0.031 |
| Ta | 0.064 | 0.197 | 0.057 | 0.070 | 0.091 | 0.085 | 0.000 | 0.082 |
| Pb | 0.118 | 0.075 | 0.075 | 0.167 | 0.013 | 0.032 | 0.005 | 0.104 |
| Th | 0.270 | 2.14 | 0.072 | 0.481 | 0.095 | 0.088 | 0.016 | 0.084 |
| U | 0.084 | 0.483 | 0.018 | 0.200 | 0.035 | 0.028 | 0.008 | 0.053 |

*Table 2: continued*

| Sample: | WFP-11 | P80180 | P80290 | P80291 | P80353# | P80354a | P80354b | P80354c |
|---|---|---|---|---|---|---|---|---|
| Locality: | Fort P | Ohira Bay | Ohira Bay | Ohira Bay | Momoe | Snake G | Snake G | Snake G |
| Phase: | opx | cpx | cpx | cpx | cpx | cpx | cpx | cpx |
| $SiO_2$ (wt %) | 57.12 | 53.73 | 54.62 | 54.84 | 53.53 | 54.73 | 54.67 | 52.95 |
| CaO (wt %) | 0.57 | 20.70 | 21.80 | 19.99 | . | 23.02 | 22.81 | 22.87 |
| *n* = | *8* | *9* | *10* | *5* | *5* | *9* | *9* | *14* |
| Li (ppm) | 2.03 | 7.28 | 4.75 | 5.61 | 2.49 | 3.81 | 5.73 | 5.96 |
| Sc | 20.7 | 75.3 | 65.3 | 75.0 | 89.5 | 94.7 | 85.2 | 72.3 |
| Ti | 15.2 | 1751 | 94.3 | 617 | 418 | 449 | 635 | 4673 |
| V | n.m. | 194 | 120 | 125 | 274 | 151 | 203 | n.m. |
| Cr | 4940 | 13752 | 6161 | 6567 | 3049 | 5588 | 6688 | 6844 |
| Mn | 1029 | 637 | 520 | 734 | 1142 | 491 | 509 | 532 |
| Co | 51.8 | 23.8 | 21.9 | 31.0 | 40.6 | 16.4 | 17.8 | 18.3 |
| Ni | 675 | 420 | 389 | 569 | 253 | 318 | 343 | 395 |
| Zn | 27.6 | 10.5 | 7.611 | 14.2 | 15.5 | 4.794 | 5.739 | 6.090 |
| Ga | 1.29 | 5.69 | 1.42 | 4.41 | 1.65 | 0.830 | 1.23 | 3.16 |
| Rb | 1.20 | 2.91 | 0.087 | 0.710 | 0.001 | 0.001 | 0.042 | 0.174 |
| Sr | 0.534 | 331 | 244 | 468 | 1.18 | 83.4 | 31.3 | 81.9 |
| Y | 0.107 | 35.3 | 2.89 | 31.0 | 4.34 | 2.63 | 6.19 | 16.6 |
| Zr | 0.248 | 275 | 14.5 | 203 | 0.531 | 14.6 | 16.9 | 47.4 |
| Nb | 0.147 | 5.15 | 1.33 | 2.53 | 0.006 | 0.158 | 0.426 | 0.077 |
| Mo | 0.037 | 0.198 | 1.58 | 0.712 | 0.030 | 0.021 | 0.059 | 0.156 |
| Ba | 0.059 | 33.8 | 14.9 | 11.1 | 0.0002 | 0.029 | 0.059 | 0.120 |
| La | 0.051 | 22.1 | 11.4 | 33.0 | 0.007 | 2.48 | 1.32 | 4.03 |
| Ce | 0.108 | 78.2 | 17.5 | 98.4 | 0.052 | 4.96 | 4.11 | 15.0 |
| Pr | 0.014 | 12.3 | 1.49 | 13.3 | 0.017 | 0.708 | 0.705 | 2.85 |
| Nd | 0.065 | 58.3 | 4.80 | 55.8 | 0.145 | 3.60 | 3.91 | 16.1 |
| Sm | 0.015 | 13.2 | 0.900 | 11.1 | 0.122 | 0.989 | 1.21 | 4.68 |
| Eu | 0.005 | 4.32 | 0.295 | 3.43 | 0.053 | 0.291 | 0.425 | 1.44 |
| Gd | 0.019 | 11.0 | 0.832 | 8.50 | 0.306 | 1.00 | 1.40 | 4.92 |
| Tb | 0.003 | 1.50 | 0.120 | 1.21 | 0.074 | 0.133 | 0.214 | 0.697 |
| Dy | 0.018 | 8.00 | 0.643 | 6.72 | 0.640 | 0.673 | 1.29 | 3.88 |
| Ho | 0.003 | 1.322 | 0.108 | 1.13 | 0.158 | 0.11 | 0.237 | 0.659 |
| Er | 0.010 | 3.27 | 0.263 | 2.95 | 0.548 | 0.247 | 0.623 | 1.59 |
| Tm | 0.002 | 0.389 | 0.032 | 0.350 | 0.082 | 0.029 | 0.079 | 0.183 |
| Yb | 0.022 | 2.12 | 0.182 | 1.98 | 0.579 | 0.196 | 0.473 | 1.00 |
| Lu | 0.006 | 0.271 | 0.027 | 0.257 | 0.094 | 0.033 | 0.067 | 0.128 |
| Hf | 0.002 | 5.59 | 0.132 | 3.29 | 0.029 | 0.395 | 0.366 | 2.09 |
| Ta | 0.009 | 0.358 | 0.060 | 0.138 | 0.0001 | 0.029 | 0.063 | 0.008 |
| Pb | 0.015 | 0.400 | 0.778 | 0.484 | 0.005 | 0.780 | 0.403 | 0.657 |
| Th | 0.068 | 0.657 | 4.953 | 0.984 | 0.0001 | 0.031 | 0.061 | 0.144 |
| U | 0.011 | 0.261 | 1.679 | 0.225 | 0.0001 | 0.053 | 0.033 | 0.034 |

*Table 3: Whole rock major, trace and platinum group element concentrations of New Zealand mantle xenoliths.*

| Sample: | NGB-3 [1] | NGB-4 [1] | P43153b [1] | P45280 [1] | MSI33D [1] | MSIK33C [1] | MSI20C [1] | MSI20G [1] | FvF-1 |
|---|---|---|---|---|---|---|---|---|---|
| Rock type: | *whr* | *dun* | *hzb* | *hzb* | *hzb* | *hzb* | *hzb* | *hzb* | *lhz* |
| *Major element analyses (wt %)* | | | | | | | | | |
| $SiO_2$ | 40.33 | 40.04 | 49.42 | 43.60 | 43.09 | 48.05 | 45.54 | 46.48 | 44.83 |
| $TiO_2$ | 0.02 | 0.02 | 0.03 | 0.03 | 0.08 | 0.15 | 0.03 | 0.04 | 0.05 |
| $Al_2O_3$ | 0.06 | 0.16 | 1.02 | 0.53 | 0.71 | 1.73 | 1.26 | 1.62 | 2.61 |
| $Cr_2O_3$ | 0.75 | 0.94 | 0.32 | 0.22 | 0.13 | 0.26 | 0.27 | 0.32 | 0.33 |
| $FeO_{(T)}$ | 10.20 | 8.14 | 9.37 | 11.80 | 10.45 | 8.72 | 8.11 | 7.71 | 8.40 |
| MnO | 0.17 | 0.13 | 0.07 | 0.16 | 0.15 | 0.12 | 0.15 | 0.14 | 0.14 |
| MgO | 46.59 | 50.32 | 38.54 | 43.14 | 44.66 | 39.96 | 44.02 | 43.01 | 40.96 |
| CaO | 1.88 | 0.23 | 1.16 | 0.39 | 0.56 | 0.91 | 0.54 | 0.60 | 2.47 |
| $Na_2O$ | 0.00 | 0.01 | 0.04 | 0.11 | 0.07 | 0.08 | 0.05 | 0.07 | 0.16 |
| $K_2O$ | 0.00 | 0.00 | 0.03 | 0.00 | 0.06 | 0.03 | 0.02 | 0.01 | 0.04 |
| $P_2O_5$ | 0.00 | 0.01 | | 0.01 | 0.03 | | | | 0.01 |
| Orig. Sum | 100.60 | 99.94 | -- | 100.75 | 100.52 | -- | -- | -- | 100.78 |
| LOI | -0.58 | -0.29 | | 0.62 | 0.99 | | | | 0.30 |
| Mg# | 0.891 | 0.917 | 0.880 | 0.867 | 0.884 | 0.891 | 0.906 | 0.909 | 0.897 |
| Ca/Al | 42.3 | 1.94 | 1.53 | 1.01 | 1.06 | 0.71 | 0.58 | 0.50 | 1.28 |
| *Trace element analyses (ppm)* | | | | | | | | | |
| *n =* | *4* | *4* | *5* | *4* | *7* | *5* | *5* | *5* | *4* |
| Ca | 11373 ±92 | 1663 ±25 | 8229 ±19 | 2465 ±17 | 3638 ±48 | 6395 ±68 | 3698 ±86 | 4728 ±72 | 15837 ±355 |
| Sc | 11.6 ±1 | 3.28 ±6 | 8.02 ±8 | 5.51 ±18 | 3.63 ±34 | 8.61 ±7 | 8.19 ±18 | 9.06 ±20 | 11.6 ±3 |
| Ti | 59.3 ±8 | 66.1 ±9 | 140 ±2 | 102±2 | 379 ±8 | 1077 ±3 | 32.0 ±3 | 56.6 ±11 | 258 ±5 |
| Cr | 4363 ±14 | 5706 ±67 | 1978 ±12 | 1371 ±15 | 829 ±6 | 1855 ±10 | 2193 ±27 | 2506 ±175 | 2122 ±12 |
| Mn | 1251 ±10 | 953 ±10 | 1180 ±6 | 1211 ±15 | 1112 ±17 | 1039 ±6 | 1066 ±7 | 1164 ±8 | 1100 ±4 |
| Co | 140 ±1 | 135 ±1 | 132 ±0.5 | 127 ±1 | 120 ±1 | 121 ±1 | 132 ±1 | 138 ±1 | 113 ±1 |
| Ni | 1796 ±15 | 1817 ±11 | 2508 ±22 | 2014 ±33 | 2302 ±29 | 2133 ±17 | 2325 ±18 | 2364 ±22 | 1984 ±14 |
| Ga | 0.766 ±36 | 1.08 ±2 | 1.94 ±4 | 0.915 ±39 | 2.39 ±8 | 2.80 ±7 | 1.24 ±4 | 1.45 ±4 | 2.17 ±5 |
| Sr | 5.60 ±7 | 6.90 ±4 | 33.4 ±5 | 1.79 ±2 | 22.7 ±4 | 13.5 ±2 | 7.05 ±5 | 8.55 ±20 | 9.94 ±19 |
| Y | 0.108 ±10 | 0.144 ±9 | 0.718 ±16 | 0.313 ±9 | 0.795 ±53 | 0.781 ±4 | 0.362 ±8 | 0.593 ±15 | 1.50 ±6 |
| Zr | 0.718 ±25 | 1.53 ±3 | 16.8 ±3 | 0.843 ±47 | 9.06 ±35 | 9.88 ±7 | 1.41 ±4 | 5.20 ±20 | 1.42 ±4 |
| Nb | 0.177 ±4 | 0.293 ±11 | 2.61 ±6 | 0.035 ±3 | 1.48 ±3 | 0.498 ±9 | 0.099 ±3 | 0.243 ±7 | 0.152 ±5 |
| Ba | 0.489 ±5 | 0.974 ±34 | 42.4 ±3 | 0.998 ±41 | 5.62 ±10 | 4.95 ±9 | 26.0 ±2 | 30.1 ±4 | 1.81 ±4 |
| La | 0.059 ±4 | 0.591 ±5 | 0.847 ±35 | 0.046 ±3 | 0.760 ±22 | 0.416 ±7 | 0.493 ±14 | 0.824 ±15 | 0.229 ±11 |
| Ce | 0.206 ±9 | 1.013 ±4 | 1.63 ±2 | 0.177 ±6 | 2.18 ±2 | 1.06 ±1 | 0.508 ±8 | 1.07 ±2 | 0.528 ±7 |
| Pr | 0.010 ±1 | 0.065 ±2 | 0.169 ±5 | 0.012 ±1 | 0.233 ±2 | 0.132 ±4 | 0.038 ±2 | 0.079 ±4 | 0.052 ±2 |
| Nd | 0.041 ±5 | 0.188 ±9 | 0.607 ±17 | 0.055 ±9 | 1.01 ±3 | 0.599 ±15 | 0.123 ±4 | 0.283 ±17 | 0.216 ±12 |
| Sm | 0.009 ±4 | 0.029 ±4 | 0.107 ±6 | 0.018 ±2 | 0.232 ±10 | 0.158 ±13 | 0.014 ±2 | 0.036 ±6 | 0.064 ±6 |
| Eu | 0.003 ±1 | 0.008 ±0.3 | 0.031 ±1 | 0.008 ±1 | 0.080 ±4 | 0.057 ±4 | 0.007 ±1 | 0.013 ±1 | 0.032 ±1 |
| Gd | 0.012 ±3 | 0.025 ±8 | 0.103 ±9 | 0.026 ±3 | 0.235 ±14 | 0.190 ±9 | 0.021 ±2 | 0.048 ±9 | 0.121 ±4 |
| Tb | 0.002 ±1 | 0.005 ±1 | 0.016 ±1 | 0.008 ±1 | 0.035 ±2 | 0.027 ±1 | — | — | 0.029 ±2 |
| Dy | 0.016 ±3 | 0.021 ±2 | 0.092 ±6 | 0.045 ±4 | 0.166 ±8 | 0.163 ±7 | 0.017 ±2 | 0.037 ±4 | 0.206 ±6 |
| Ho | 0.003 ±1 | 0.005 ±0.3 | 0.017 ±1 | 0.010 ±1 | 0.028 ±1 | 0.028 ±2 | 0.005 ±1 | 0.008 ±1 | 0.046 ±1 |
| Er | 0.010 ±1 | 0.012 ±2 | 0.058 ±3 | 0.033 ±4 | 0.073 ±6 | 0.078 ±3 | 0.016 ±1 | 0.028 ±3 | 0.165 ±15 |
| Tm | 0.002 ±0.3 | 0.002 ±1 | 0.008 ±1 | 0.005 ±1 | 0.009 ±1 | 0.009 ±2 | 0.002 ±0.4 | 0.004 ±1 | 0.025 ±1 |
| Yb | 0.015 ±3 | 0.014 ±3 | 0.062 ±4 | 0.037 ±2 | 0.060 ±6 | 0.060 ±3 | 0.021 ±2 | 0.038 ±10 | 0.180 ±5 |
| Lu | 0.002 ±0.2 | 0.002 ±1 | 0.009 ±1 | 0.006 ±1 | 0.009 ±1 | 0.008 ±1 | 0.004 ±1 | 0.006 ±1 | 0.027 ±2 |
| Hf | 0.010 ±1 | 0.029 ±2 | 0.208 ±8 | 0.018 ±2 | 0.241 ±13 | 0.389 ±10 | 0.030 ±4 | 0.106 ±4 | 0.029 ±1 |
| Ta | 0.005 ±1 | 0.012 ±1 | 0.043 ±2 | 0.003 ±1 | 0.096 ±3 | 0.040 ±3 | 0.005 ±1 | 0.014 ±1 | 0.012 ±1 |
| Th | 0.009 ±2 | 0.427 ±8 | 0.082 ±3 | 0.005 ±0.5 | 0.098 ±3 | 0.048 ±2 | 0.078 ±2 | 0.117 ±3 | 0.027 ±1 |
| U | 0.008 ±1 | 0.083 ±2 | 0.073 ±2 | 0.006 ±2 | 0.026 ±1 | 0.025 ±2 | 0.029 ±1 | 0.042 ±2 | 0.031 ±18 |
| Ti/Eu | 21816 | 8520 | 4487 | 13009 | 4716 | 18985 | 4608 | 4335 | 8151 |
| $La/Yb_N$ | 2.66 | 28.74 | 9.14 | 0.841 | 8.52 | 4.63 | 15.94 | 14.67 | 0.856 |
| *Platinum group element analyses (ppb)* | | | | | | | | | |
| Os* | 4.892 | 1.548 | 0.018 | 2.965 | 3.155 | 1.310 | 3.827 | 3.458 | |
| Ir | 1.206 | 0.885 | 0.030 | 2.880 | 2.573 | 1.848 | 3.014 | 2.347 | |
| Ru | 4.070 | 5.091 | 1.102 | 4.318 | 8.593 | 3.968 | 5.327 | 7.341 | |
| Pt | 9.336 | 7.345 | 0.091 | 1.047 | 1.220 | 0.168 | 5.331 | 4.006 | |
| Pd | 4.799 | 0.362 | 0.029 | 0.086 | 1.122 | 0.023 | 0.600 | 0.415 | |
| Re* | 0.007 | 0.018 | 0.165 | 0.013 | 0.024 | 0.010 | 0.007 | 0.011 | |
| $\Sigma_{PGE}$ | 24.3 | 15.2 | 1.4 | 11.3 | 16.7 | 7.3 | 18.1 | 17.6 | |
| $\Sigma_{I\text{-}PGE}$ | 10.2 | 7.5 | 1.1 | 10.2 | 14.3 | 7.1 | 12.2 | 13.1 | |
| $\Sigma_{P\text{-}PGE}$ | 14.1 | 7.7 | 0.1 | 1.1 | 2.3 | 0.2 | 5.9 | 4.4 | |
| $Pd/Ir_N$ | 3.15 | 0.32 | 0.76 | 0.02 | 0.34 | 0.010 | 0.16 | 0.14 | |
| $Pt/Ir_N$ | 4.00 | 4.28 | 1.59 | 0.19 | 0.24 | 0.05 | 0.91 | 0.88 | |
| $^{187}Os/^{188}Os_{(i)}$* | 0.12700 | 0.12942 | 0.11242 | 0.12584 | 0.12406 | 0.12630 | 0.11982 | 0.11989 | |

*Table 3: Continued*

| Sample: | MSI79C [1] | MSI79C [2] | WTL-1 [1] | WTL-2 [1] | WTL-3 [1] | OU45852 [1] | OU45852 [3] | WRR-1 [1] | WRR-3 [1] |
|---|---|---|---|---|---|---|---|---|---|
| Rock type: | *Ol web* | | *lhz* | *hzb* | *lhz* | *lhz* | | *hzb* | *lhz* |
| *Major element analyses (wt %)* | | | | | | | | | |
| $SiO_2$ | 48.95 | | 44.91 | 45.42 | 44.01 | 44.18 | | 43.17 | 44.00 |
| $TiO_2$ | 0.05 | | 0.05 | 0.02 | 0.05 | 0.04 | | 0.07 | 0.04 |
| $Al_2O_3$ | 3.45 | | 2.64 | 1.45 | 2.02 | 2.35 | | 1.44 | 1.76 |
| $Cr_2O_3$ | 0.37 | | 0.47 | 0.47 | 0.34 | 0.38 | | 0.36 | 0.37 |
| $FeO_{(T)}$ | 7.18 | | 8.20 | 7.77 | 9.07 | 8.35 | | 8.69 | 8.67 |
| MnO | 0.12 | | 0.13 | 0.13 | 0.14 | 0.14 | | 0.14 | 0.14 |
| MgO | 37.70 | | 41.23 | 43.48 | 42.11 | 42.05 | | 44.30 | 42.68 |
| CaO | 1.92 | | 2.29 | 1.24 | 2.21 | 2.44 | | 1.73 | 2.26 |
| $Na_2O$ | 0.23 | | 0.07 | 0.03 | 0.04 | 0.06 | | 0.07 | 0.06 |
| $K_2O$ | 0.02 | | 0.00 | 0.00 | 0.00 | 0.00 | | 0.01 | 0.01 |
| $P_2O_5$ | | | 0.01 | 0.00 | 0.01 | 0.00 | | 0.02 | 0.01 |
| Orig. Sum | -- | | 100.68 | 100.36 | 100.28 | 99.76 | | 100.68 | 100.07 |
| LOI | | | 0.46 | 0.75 | 0.63 | 0.08 | | 0.80 | 0.38 |
| Mg# | 0.904 | | 0.900 | 0.909 | 0.892 | 0.900 | | 0.901 | 0.898 |
| Ca/Al | 0.75 | | 1.17 | 1.15 | 1.48 | 1.40 | | 1.63 | 1.73 |
| *Trace element analyses (ppm)* | | | | | | | | | |
| *n =* | *5* | | *7* | *5* | *5* | *4* | *5* | *4* | |
| Ca | 14730 ±206 | | 14167 ±211 | 7969 ±52 | 14616 ±85 | 15391 ±200 | 15527 ±625 | 10617 ±164 | |
| Sc | 14.3 ±2 | | 12.9 ±2 | 10.6 ±1 | 12.6 ±2 | 12.8 ±2 | 13.2 ±5 | 9.28 ±9 | |
| Ti | 455 ±4 | | 241 ±3 | 78.2 ±12 | 255 ±2 | 202 ±3 | 203±5 | 337 ±3 | |
| Cr | 2246 ±14 | | 2951 ±31 | 2842 ±8 | 2241 ±18 | 2603 ±367 | 2433 ±173 | 2266 ±22 | |
| Mn | 1114 ±3 | | 1013 ±11 | 952 ±6 | 1056 ±5 | 1021 ±10 | 1003 ±12 | 1062 ±6 | |
| Co | 118 ±1 | | 107 ±1 | 106 ±1 | 119 ±1 | 109 ±1 | 109 ±1 | 118 ±1 | |
| Ni | 1978 ±11 | | 1851 ±39 | 1965 ±25 | 2103 ±16 | 1921 ±19 | 1904 ±11 | 2102 ±20 | |
| Ga | 4.82 ±9 | | 3.81 ±1 | 8.37 ±7 | 4.65 ±5 | 2.25 ±6 | 2.25 ±5 | 4.57 ±5 | |
| Sr | 13.7 ±2 | | 3.72 ±8 | 3.94 ±8 | 3.95 ±4 | 1.23 ±3 | 1.34 ±6 | 10.7 ±2 | |
| Y | 2.26 ±6 | | 1.48 ±2 | 1.31 ±2 | 1.49 ±3 | 1.71 ±5 | 1.69 ±9 | 0.921 ±28 | |
| Zr | 5.96 ±15 | | 2.91 ±5 | 4.03 ±6 | 1.76 ±3 | 0.497 ±31 | 0.306 ±19 | 3.33 ±6 | |
| Nb | 1.66 ±3 | | 0.547 ±13 | 0.506 ±5 | 0.546 ±10 | 0.025 ±2 | 0.041 ±3 | 1.48 ±3 | |
| Ba | 1.84 ±4 | | 0.890 ±42 | 2.14 ±16 | 1.36 ±3 | 0.777 ±16 | 0.775 ±33 | 2.77 ±12 | |
| La | 0.651 ±13 | | 0.145 ±5 | 2.18 ±22 | 0.131 ±5 | 0.054 ±1 | 0.055 ±3 | 0.708 ±10 | |
| Ce | 1.08 ±2 | | 0.185 ±6 | -- | 0.077 ±4 | 0.043 ±3 | 0.054 ±1 | 1.52 ±3 | |
| Pr | 0.102 ±4 | | 0.012 ±2 | 0.135 ±3 | 0.007 ±1 | 0.005 ±1 | 0.006 ±1 | 0.155 ±4 | |
| Nd | 0.404 ±24 | | 0.063 ±6 | 0.539 ±12 | 0.049 ±5 | 0.049 ±8 | 0.047 ±2 | 0.591 ±36 | |
| Sm | 0.125 ±10 | | 0.036 ±3 | 0.057 ±1 | 0.042 ±3 | 0.047 ±5 | 0.040 ±6 | 0.130 ±11 | |
| Eu | 0.052 ±2 | | 0.019 ±2 | 0.021 ±2 | 0.021 ±3 | 0.021 ±2 | 0.021 ±1 | 0.042 ±4 | |
| Gd | 0.222 ±11 | | 0.104 ±11 | 0.115 ±7 | 0.118 ±6 | 0.114 ±14 | 0.118 ±10 | 0.137 ±12 | |
| Tb | 0.044 ±1 | | 0.038 ±2 | 0.011 ±1 | 0.028 ±3 | 0.025 ±1 | 0.033 ±4 | 0.025 ±3 | |
| Dy | 0.335 ±10 | | 0.198 ±8 | 0.078 ±3 | 0.205 ±5 | 0.225 ±6 | 0.238 ±12 | 0.150 ±2 | |
| Ho | 0.075 ±3 | | 0.048 ±2 | 0.019 ±1 | 0.048 ±1 | 0.058 ±4 | 0.057 ±3 | 0.030 ±2 | |
| Er | 0.255 ±11 | | 0.171 ±10 | 0.059 ±3 | 0.176 ±8 | 0.205 ±9 | 0.201 ±14 | 0.094 ±4 | |
| Tm | 0.038 ±3 | | 0.025 ±2 | 0.009 ±1 | 0.026 ±1 | 0.028 ±2 | 0.029 ±2 | 0.014 ±2 | |
| Yb | 0.287 ±23 | | 0.192 ±14 | 0.069 ±4 | 0.194 ±7 | 0.214 ±5 | 0.228 ±19 | 0.100 ±9 | |
| Lu | 0.042 ±2 | | 0.031 ±1 | 0.012 ±1 | 0.031 ±1 | 0.034 ±2 | 0.035 ±2 | 0.016 ±1 | |
| Hf | 0.129 ±5 | | 0.031 ±3 | 0.036 ±4 | 0.040 ±2 | 0.024 ±2 | 0.023 ±3 | 0.078 ±6 | |
| Ta | 0.031 ±2 | | 0.003 ±1 | 0.003 ±1 | 0.002 ±1 | 0.001 ±0.2 | 0.001 ±0.2 | 0.047 ±3 | |
| Th | 0.073 ±3 | | 0.021 ±2 | 0.046 ±2 | 0.076 ±2 | 0.003 ±1 | 0.003 ±1 | 0.126 ±4 | |
| U | 0.147 ±2 | | 0.077 ±2 | 0.079 ±4 | 0.122 ±2 | 0.006 ±1 | 0.006 ±1 | 0.056 ±2 | |
| Ti/Eu | 8744 | | 13013 | 3721 | 12157 | 9562 | 9814 | 8065 | |
| $La/Yb_N$ | 1.53 | | 0.509 | 21.38 | 0.456 | 0.169 | 0.162 | 4.75 | |
| *Platinum group element analyses (ppb)* | | | | | | | | | |
| Os* | 4.718 | -- | 3.185 | 2.763 | 3.168 | 2.596 | | 3.206 | |
| Ir | 4.177 | 4.407 | 3.158 | 2.869 | 2.725 | 2.395 | | 3.107 | |
| Ru | 8.249 | 8.660 | 6.255 | 5.473 | 5.608 | 5.693 | | 4.867 | |
| Pt | 7.279 | 7.626 | 5.813 | 4.120 | 4.685 | 4.459 | | 4.693 | |
| Pd | 5.851 | 6.061 | 4.710 | 1.730 | 3.924 | 4.382 | | 1.810 | |
| Re* | 0.265 | 0.267 | 0.153 | 0.037 | 0.125 | 0.118 | | 0.083 | |
| $\Sigma_{PGE}$ | 30.5 | 31.7 | 23.3 | 17.0 | 20.2 | 19.6 | | 17.8 | |
| $\Sigma_{I\text{-}PGE}$ | 17.1 | 17.8 | 12.6 | 11.1 | 11.5 | 10.7 | | 11.2 | |
| $\Sigma_{P\text{-}PGE}$ | 13.4 | 14.0 | 10.5 | 5.8 | 8.6 | 8.8 | | 6.5 | |
| $Pd/Ir_N$ | 1.10 | | 1.18 | 0.48 | 1.14 | 1.45 | | 0.46 | |
| $Pt/Ir_N$ | 0.90 | | 0.95 | 0.74 | 0.89 | 0.96 | | 0.78 | |
| $^{187}Os/^{188}Os_{(i)}$* | 0.11953 | | 0.12390 | 0.11703 | 0.12152 | 0.12380 | | 0.11662 | |

*Table 3: Continued*

| Sample: | WRR-5 [1] | WRR-6 [1] | WRR-7 [1] | WRR-9 [1] | DPP-1 [4] | DPP-2 [4] | DPP-3 [4] | DPP-5 [4] | DPP-6 [4] |
|---|---|---|---|---|---|---|---|---|---|
| Rock type: | *hzb* | *whr* | *hzb* | *hzb* | *lhz* | *hzb* | *lhz* | *lhz* | *Ol web* |
| *Major element analyses (wt %)* | | | | | | | | | |
| $SiO_2$ | 43.38 | 41.83 | 43.35 | 44.17 | 39.10 | 45.66 | 45.60 | 42.90 | 48.57 |
| $TiO_2$ | 0.01 | 0.08 | 0.02 | 0.06 | 0.15 | 0.04 | 0.12 | 0.13 | 0.16 |
| $Al_2O_3$ | 0.76 | 1.12 | 1.00 | 1.06 | 5.45 | 1.34 | 3.24 | 4.13 | 3.87 |
| $Cr_2O_3$ | 0.49 | 0.33 | 0.37 | 0.47 | 0.64 | 0.47 | 0.37 | 0.48 | 0.63 |
| $FeO_{(T)}$ | 8.15 | 9.58 | 8.52 | 8.17 | 6.24 | 6.85 | 8.05 | 7.65 | 8.16 |
| MnO | 0.14 | 0.21 | 0.14 | 0.14 | 0.42 | 0.15 | 0.13 | 0.19 | 0.13 |
| MgO | 45.91 | 43.97 | 45.41 | 44.32 | 21.55 | 33.62 | 38.56 | 32.70 | 35.50 |
| CaO | 1.16 | 1.87 | 1.17 | 1.14 | 26.14 | 11.77 | 3.69 | 11.51 | 2.71 |
| $Na_2O$ | 0.00 | 0.41 | 0.00 | 0.24 | 0.23 | 0.03 | 0.22 | 0.25 | 0.22 |
| $K_2O$ | 0.00 | 0.32 | 0.00 | 0.19 | 0.03 | 0.05 | 0.00 | 0.01 | 0.04 |
| $P_2O_5$ | 0.00 | 0.27 | 0.01 | 0.03 | 0.05 | 0.03 | 0.02 | 0.03 | 0.01 |
| Orig. Sum | 100.00 | 100.16 | 100.17 | 100.39 | 103.30 | 101.75 | 100.75 | 101.77 | 100.53 |
| LOI | 0.36 | 0.48 | 0.40 | 0.60 | 16.32 | 9.81 | 1.72 | 6.34 | 2.83 |
| Mg# | 0.909 | 0.891 | 0.905 | 0.906 | 0.860 | 0.897 | 0.895 | 0.884 | 0.886 |
| Ca/Al | 2.07 | 2.26 | 1.58 | 1.45 | 6.48 | 11.9 | 1.54 | 3.76 | 0.95 |
| *Trace element analyses (ppm)* | | | | | | | | | |
| *n* = | *4* | | *4* | *4* | *4* | *7* | *4* | *4* | *8* |
| Ca | 6883 ±58 | | 7199 ±72 | 6948 ±114 | -- | -- | *24857 ±570* | -- | *34764 ±916* |
| Sc | 7.04 ±10 | | 7.49 ±20 | 8.12 ±5 | *22.1 ±2* | *10.6 ±2* | *14.7 ±3* | *16.9 ±3* | *14.9 ±8* |
| Ti | 36.2 ±7 | | 74.8 ±16 | 265 ±3 | *793 ±5* | *189 ±5* | *618 ±16* | *726 ±10* | *847 ±21* |
| Cr | 2741 ±66 | | 2373 ±11 | 2896 ±19 | *2399 ±8* | *3238 ±73* | *2500 ±10* | *3218 ±21* | *3984 ±19* |
| Mn | 1065 ±9 | | 1055 ±10 | 1051 ±10 | *2978 ±15* | *1247 ±29* | *1048 ±6* | *1513 ±13* | *1016 ±4* |
| Co | 117 ±1 | | 120 ±2 | 113 ±1 | *61.4 ±4* | *104 ±2* | *104 ±1* | *93.5 ±11* | *104 ±1* |
| Ni | 2212 ±19 | | 2221 ±33 | 2132 ±30 | *798 ±8* | *1914 ±56* | *1723 ±5* | *1493 ±20* | *1771 ±14* |
| Ga | 0.822 ±27 | | 1.90 ±8 | 2.21 ±6 | *4.95 ±8* | *1.85 ±8* | *3.37 ±6* | *5.30 ±5* | *4.82 ±5* |
| Sr | 8.10 ±1 | | 6.78 ±4 | 25.9 ±3 | *1914 ±6* | *1022 ±23* | *97.4 ±26* | *968 ±11* | *258 ±7* |
| Y | 0.124 ±6 | | 0.488 ±16 | 0.954 ±25 | *7.92 ±10* | *2.32 ±9* | *4.34 ±15* | *5.92 ±19* | *4.06 ±22* |
| Zr | 0.621 ±22 | | 1.06 ±1 | 5.34 ±9 | *27.3 ±2* | *38.5 ±12* | *5.34 ±20* | *18.9 ±4* | *10.7 ±6* |
| Nb | 0.190 ±2 | | 0.331 ±14 | 3.06 ±3 | *5.38 ±2* | *5.71 ±12* | *0.876 ±27* | *3.37 ±5* | *2.34 ±6* |
| Ba | 0.825 ±38 | | 0.543 ±56 | 7.11 ±6 | *55.2 ±5* | *20.9 ±4* | *3.90 ±12* | *22.1 ±1* | *3.78 ±9* |
| La | 0.226 ±11 | | 0.631 ±18 | 3.34 ±7 | *3.94 ±3* | *2.68 ±6* | *1.37 ±4* | *5.13 ±9* | *1.27 ±7* |
| Ce | 0.472 ±10 | | 1.28 ±1 | 5.62 ±4 | *4.34 ±4* | *2.97 ±6* | *1.43 ±3* | *6.70 ±5* | *2.03 ±3* |
| Pr | 0.033 ±2 | | 0.111 ±1 | 0.444 ±2 | *0.378 ±6* | *0.253 ±9* | *0.137 ±6* | *0.539 ±13* | *0.223 ±8* |
| Nd | 0.115 ±2 | | 0.363 ±16 | 1.39 ±6 | *1.35 ±5* | *0.821 ±21* | *0.624 ±29* | *1.78 ±5* | *0.928 ±47* |
| Sm | 0.019 ±4 | | 0.055 ±8 | 0.179 ±20 | *0.395 ±19* | *0.142 ±12* | *0.224 ±18* | *0.436 ±7* | *0.279 ±18* |
| Eu | 0.005 ±1 | | 0.015 ±1 | 0.059 ±2 | *0.152 ±8* | *0.045 ±3* | *0.091 ±3* | *0.148 ±5* | *0.104 ±6* |
| Gd | 0.011 ±2 | | 0.060 ±3 | 0.157 ±7 | *0.647 ±32* | *0.181 ±9* | *0.381 ±9* | *0.618 ±20* | *0.390 ±24* |
| Tb | 0.003 ±1 | | 0.013 ±2 | 0.028 ±2 | *0.126 ±1* | *0.034 ±2* | *0.076 ±1* | *0.116 ±2* | *0.077 ±6* |
| Dy | 0.019 ±4 | | 0.069 ±5 | 0.140 ±7 | *0.980 ±16* | *0.191 ±9* | *0.567 ±21* | *0.811 ±34* | *0.542 ±30* |
| Ho | 0.003 ±1 | | 0.015 ±3 | 0.028 ±2 | *0.226 ±5* | *0.042 ±3* | *0.130 ±5* | *0.182 ±4* | *0.122 ±9* |
| Er | 0.011 ±1 | | 0.055 ±2 | 0.099 ±7 | *0.781 ±19* | *0.151 ±6* | *0.426 ±10* | *0.606 ±25* | *0.419 ±25* |
| Tm | 0.002 ±0.2 | | 0.008 ±1 | 0.012 ±1 | *0.110 ±3* | *0.020 ±2* | *0.057 ±1* | *0.084 ±4* | *0.061 ±5* |
| Yb | 0.016 ±2 | | 0.065 ±6 | 0.111 ±7 | *0.702 ±7* | *0.130 ±6* | *0.393 ±15* | *0.526 ±26* | *0.412 ±23* |
| Lu | 0.003 ±1 | | 0.011 ±1 | 0.016 ±2 | *0.098 ±2* | *0.017 ±1* | *0.054 ±2* | *0.073 ±2* | *0.059 ±5* |
| Hf | 0.014 ±2 | | 0.017 ±5 | 0.092 ±5 | *0.271 ±9* | *0.124 ±6* | *0.133 ±5* | *0.226 ±5* | *0.196 ±14* |
| Ta | 0.009 ±1 | | 0.010 ±1 | 0.150 ±4 | *0.109 ±3* | *0.049 ±3* | *0.009 ±2* | *0.027 ±2* | *0.054 ±4* |
| Th | 0.037 ±2 | | 0.076 ±6 | 0.999 ±13 | *0.402 ±10* | *0.168 ±5* | *0.243 ±15* | *0.556 ±8* | *0.420 ±25* |
| U | 0.029 ±3 | | 0.028 ±3 | 0.302 ±3 | *4.36 ±4* | *1.49 ±6* | *1.09 ±2* | *3.38 ±2* | *0.830 ±8* |
| Ti/Eu | 7766 | | 5007 | 4505 | 5220 | 4229 | 6756 | 4906 | 8140 |
| $La/Yb_N$ | 9.57 | | 6.52 | 20.20 | 3.78 | 13.86 | 2.34 | 6.57 | 2.08 |
| *Platinum group element analyses (ppb)* | | | | | | | | | |
| Os* | 5.378 | | 3.937 | 6.608 | | 3.060 | | | 6.808 |
| Ir | 3.919 | | 3.316 | 4.300 | | 2.602 | | | 5.819 |
| Ru | 8.940 | | 6.800 | 8.990 | | 4.754 | | | 6.009 |
| Pt | 4.791 | | 6.517 | 5.595 | | 1.552 | | | 12.311 |
| Pd | 0.142 | | 3.052 | 9.103 | | 0.330 | | | 0.196 |
| Re* | 0.023 | | 0.032 | 0.203 | | 0.013 | | | 0.008 |
| $\Sigma_{PGE}$ | 23.2 | | 23.7 | 34.8 | | 12.3 | | | 31.2 |
| $\Sigma_{I\text{-}PGE}$ | 18.2 | | 14.1 | 19.9 | | 10.4 | | | 18.6 |
| $\Sigma_{P\text{-}PGE}$ | 4.9 | | 9.6 | 14.7 | | 1.9 | | | 12.5 |
| $Pd/Ir_N$ | 0.03 | | 0.73 | 1.67 | | 0.10 | | | 0.03 |
| $Pt/Ir_N$ | 0.63 | | 1.01 | 0.67 | | 0.31 | | | 1.09 |
| $^{187}Os/^{188}Os_{(i)}$* | 0.11797 | | 0.11653 | 0.11764 | | 0.11559 | | | 0.12566 |

*Table 3: Continued*

| Sample: | WFP-1 [1] | WFP-2 [1] | WFP-2 [3] | WFP-4 [1] | WFP-5 [1] | WFP-7 [1] | WFP-8 [1] | WFP-11 [1] | P80180 [1] |
|---|---|---|---|---|---|---|---|---|---|
| Rock type: | *lhz* | *hzb* | | *hzb* | *hzb* | *hzb* | *lhz* | *hzb* | *hzb* |
| *Major element analyses (wt %)* | | | | | | | | | |
| $SiO_2$ | 44.00 | 44.05 | 43.93 | 43.76 | 44.26 | 43.89 | 44.84 | 43.72 | 43.75 |
| $TiO_2$ | 0.02 | 0.05 | 0.05 | 0.02 | 0.02 | 0.02 | 0.02 | 0.01 | 0.07 |
| $Al_2O_3$ | 0.98 | 1.91 | 2.01 | 0.56 | 0.81 | 1.21 | 1.89 | 0.54 | 0.78 |
| $Cr_2O_3$ | 0.38 | 0.40 | 0.37 | 0.37 | 0.40 | 0.40 | 0.48 | 0.29 | 0.38 |
| $FeO_{(T)}$ | 7.51 | 8.64 | 8.55 | 8.25 | 7.57 | 8.22 | 8.13 | 7.80 | 7.92 |
| MnO | 0.12 | 0.13 | 0.13 | 0.12 | 0.13 | 0.13 | 0.14 | 0.12 | 0.13 |
| MgO | 46.12 | 42.88 | 43.07 | 46.27 | 46.02 | 44.83 | 42.33 | 46.98 | 45.82 |
| CaO | 0.84 | 1.88 | 1.83 | 0.66 | 0.78 | 1.31 | 2.16 | 0.52 | 0.92 |
| $Na_2O$ | 0.01 | 0.05 | 0.06 | 0.00 | 0.00 | 0.00 | 0.01 | 0.01 | 0.13 |
| $K_2O$ | 0.00 | 0.00 | 0.00 | 0.00 | 0.00 | 0.00 | 0.00 | 0.01 | 0.06 |
| $P_2O_5$ | 0.01 | 0.00 | 0.01 | 0.00 | 0.00 | 0.00 | 0.00 | 0.00 | 0.04 |
| Orig. Sum | 99.77 | 100.74 | 99.77 | 99.74 | 99.81 | 100.09 | 100.35 | 99.86 | 99.69 |
| LOI | 0.38 | 0.26 | 0.12 | 0.29 | 0.48 | 0.46 | 0.26 | 0.45 | 0.50 |
| Mg# | 0.916 | 0.898 | 0.900 | 0.909 | 0.915 | 0.907 | 0.903 | 0.915 | 0.912 |
| Ca/Al | 1.16 | 1.33 | 1.23 | 1.60 | 1.30 | 1.46 | 1.55 | 1.30 | 1.58 |
| *Trace element analyses (ppm)* | | | | | | | | | |
| *n* = | *5* | *4* | *4* | *5* | *4* | | *4* | *4* | *4* |
| Ca | 5495 ±90 | 11881 ±60 | 12290 ±156 | 4459 ±78 | 4975 ±9 | | 13775 ±170 | 3281 ±43 | 5814 ±123 |
| Sc | 8.93 ±14 | 11.3 ±1 | 11.4 ±3 | 9.21 ±16 | 7.47 ±8 | | 13.1 ±2 | 6.74 ±6 | 6.50 ±19 |
| Ti | 35.5 ±7 | 223 ±2 | 224 ±3 | 53.1 ±6 | 48.0 ±7 | | 46.1 ±2 | 28.4 ±6 | 353 ±5 |
| Cr | 2305 ±56 | 2412 ±28 | 2442 ±86 | 2247 ±12 | 2468 ±12 | | 3070 ±28 | 1793 ±7 | 2234 ±7 |
| Mn | 894 ±7 | 1011 ±2 | 1010 ±15 | 949 ±4 | 895 ±7 | | 992 ±10 | 920 ±4 | 943 ±5 |
| Co | 112 ±2 | 113 ±1 | 113 ±2 | 118 ±1 | 112 ±1 | | 108 ±1 | 114 ±1 | 113 ±1 |
| Ni | 2190 ±22 | 2009 ±13 | 2035 ±19 | 2217 ±7 | 2173 ±20 | | 1951 ±26 | 2217 ±10 | 2190 ±20 |
| Ga | 1.02 ±3 | 1.86 ±5 | 1.92 ±7 | 0.758 ±19 | 0.869 ±15 | | 1.52 ±5 | 0.725 ±9 | 1.43 ±5 |
| Sr | 3.51 ±7 | 1.76 ±5 | 1.79 ±4 | 2.44 ±3 | 4.88 ±4 | | 4.37 ±2 | 2.41 ±3 | 25.8 ±6 |
| Y | 0.120 ±5 | 1.11 ±3 | 1.18 ±3 | 0.140 ±7 | 0.102 ±7 | | 0.456 ±14 | 0.108 ±5 | 1.67 ±4 |
| Zr | 1.06 ±3 | 0.926 ±44 | 1.13 ±39 | 1.84 ±35 | 0.572 ±15 | | 0.310 ±12 | 1.13 ±2 | 19.3 ±4 |
| Nb | 0.473 ±13 | 0.114 ±6 | 0.115 ±7 | 0.495 ±8 | 0.128 ±7 | | 0.118 ±4 | 0.711 ±6 | 3.21 ±9 |
| Ba | 0.257 ±12 | 0.327 ±20 | 0.330 ±36 | 1.40 ±41 | 0.425 ±18 | | 0.473 ±17 | 0.792 ±37 | 10.5 ±1 |
| La | 0.470 ±8 | 0.142 ±2 | 0.162 ±52 | 0.246 ±7 | 0.089 ±3 | | 0.042 ±1 | 0.207 ±4 | 2.66 ±6 |
| Ce | 0.485 ±7 | 0.264 ±5 | 0.255 ±8 | 0.501 ±10 | 0.179 ±6 | | 0.100 ±4 | 0.464 ±9 | 6.16 ±4 |
| Pr | 0.029 ±1 | 0.028 ±2 | 0.030 ±4 | 0.048 ±2 | 0.014 ±1 | | 0.006 ±1 | 0.046 ±4 | 0.679 ±15 |
| Nd | 0.086 ±6 | 0.138 ±7 | 0.138 ±7 | 0.166 ±11 | 0.052 ±6 | | 0.016 ±2 | 0.193 ±6 | 2.63 ±7 |
| Sm | 0.015 ±2 | 0.048 ±2 | 0.053 ±4 | 0.026 ±3 | 0.012 ±4 | | 0.004 ±4 | 0.034 ±10 | 0.487 ±8 |
| Eu | 0.005 ±1 | 0.022 ±2 | 0.021 ±3 | 0.008 ±1 | 0.003 ±1 | | 0.001 ±1 | 0.010 ±2 | 0.142 ±4 |
| Gd | 0.014 ±2 | 0.091 ±1 | 0.088 ±5 | 0.026 ±2 | 0.014 ±3 | | 0.011 ±2 | 0.029 ±7 | 0.421 ±25 |
| Tb | 0.003 ±1 | 0.022 ±2 | 0.020 ±2 | 0.005 ±1 | 0.004 ±1 | | 0.006 ±2 | 0.005 ±1 | 0.058 ±3 |
| Dy | 0.014 ±2 | 0.156 ±4 | 0.170 ±13 | 0.020 ±4 | 0.013 ±3 | | 0.047 ±3 | 0.018 ±3 | 0.315 ±15 |
| Ho | 0.003 ±1 | 0.037 ±2 | 0.038 ±3 | 0.004 ±1 | 0.003 ±1 | | 0.014 ±1 | 0.002 ±1 | 0.055 ±3 |
| Er | 0.015 ±1 | 0.128 ±3 | 0.136 ±3 | 0.014 ±3 | 0.013 ±1 | | 0.056 ±6 | 0.008 ±2 | 0.161 ±8 |
| Tm | 0.003 ±1 | 0.019 ±1 | 0.020 ±1 | 0.002 ±1 | 0.002 ±1 | | 0.011 ±1 | 0.001 ±1 | 0.020 ±1 |
| Yb | 0.031 ±2 | 0.134 ±7 | 0.145 ±5 | 0.024 ±2 | 0.017 ±2 | | 0.090 ±5 | 0.010 ±2 | 0.130 ±9 |
| Lu | 0.005 ±1 | 0.022 ±1 | 0.022 ±1 | 0.004 ±1 | 0.003 ±1 | | 0.014 ±1 | 0.002 ±1 | 0.019 ±2 |
| Hf | 0.021 ±3 | 0.027 ±2 | 0.033 ±9 | 0.037 ±3 | 0.010 ±4 | | 0.003 ±2 | 0.017 ±1 | 0.369 ±8 |
| Ta | 0.017 ±2 | 0.008 ±1 | 0.006 ±1 | 0.022 ±1 | 0.005 ±1 | | 0.002 ±1 | 0.036 ±1 | 0.178 ±8 |
| Th | 0.110 ±6 | 0.012 ±1 | 0.013 ±2 | 0.071 ±3 | 0.018 ±1 | | 0.010 ±2 | 0.061 ±3 | 0.319 ±12 |
| U | 0.056 ±2 | 0.030 ±1 | 0.031 ±3 | 0.103 ±2 | 0.028 ±2 | | 0.015 ±1 | 0.193 ±2 | 0.184 ±2 |
| Ti/Eu | 7063 | 10081 | 10707 | 6706 | 14949 | | 34647 | 2945 | 2482 |
| $La/Yb_N$ | 10.36 | 0.714 | 0.754 | 6.83 | 3.51 | | 0.316 | 13.98 | 13.81 |
| *Platinum group element analyses (ppb)* | | | | | | | | | |
| Os* | 0.959 | 3.038 | | | | | 4.774 | 0.386 | 7.228 |
| Ir | 0.948 | 2.947 | | | | | 4.129 | 0.344 | 1.940 |
| Ru | 1.670 | 6.184 | | | | | 8.295 | 2.600 | 4.859 |
| Pt | 0.435 | 5.816 | | | | | 8.475 | 0.077 | 0.294 |
| Pd | 0.251 | 4.559 | | | | | 7.669 | 0.111 | 0.193 |
| Re* | 0.014 | 0.220 | | | | | 0.233 | 0.019 | 0.006 |
| $\Sigma_{PGE}$ | 4.3 | 22.8 | | | | | 33.6 | 3.5 | 14.5 |
| $\Sigma_{I\text{-}PGE}$ | 3.6 | 12.2 | | | | | 17.2 | 3.3 | 14.0 |
| $\Sigma_{P\text{-}PGE}$ | 0.7 | 10.4 | | | | | 16.1 | 0.2 | 0.5 |
| $Pd/Ir_N$ | 0.21 | 1.22 | | | | | 1.47 | 0.25 | 0.08 |
| $Pt/Ir_N$ | 0.24 | 1.02 | | | | | 1.06 | 0.11 | 0.08 |
| $^{187}Os/^{188}Os_{(i)}$* | 0.13293 | 0.12684 | | | | | 0.12354 | 0.12573 | 0.12408 |

*Table 3: Continued*

| Sample: | P80290 [1] | P80291 [1] | P80354a [1] | P80354b [1] | P80354c [1] |
|---|---|---|---|---|---|
| Rock type: | *hzb* | *hzb* | *hzb* | *hzb* | *lhz* |
| *Major element analyses (wt %)* | | | | | |
| $SiO_2$ | 44.38 | 43.03 | 44.05 | 43.63 | 43.48 |
| $TiO_2$ | 0.02 | 0.04 | 0.04 | 0.03 | 0.14 |
| $Al_2O_3$ | 0.57 | 0.64 | 0.61 | 0.51 | 0.74 |
| $Cr_2O_3$ | 0.32 | 0.39 | 0.41 | 0.27 | 0.24 |
| $FeO_{(T)}$ | 7.95 | 8.01 | 8.42 | 8.06 | 8.56 |
| MnO | 0.13 | 0.13 | 0.13 | 0.13 | 0.13 |
| MgO | 45.60 | 46.70 | 45.76 | 46.78 | 45.16 |
| CaO | 0.98 | 0.90 | 0.58 | 0.58 | 1.27 |
| $Na_2O$ | 0.02 | 0.09 | 0.00 | 0.00 | 0.25 |
| $K_2O$ | 0.01 | 0.03 | 0.00 | 0.00 | 0.02 |
| $P_2O_5$ | 0.01 | 0.04 | 0.01 | 0.01 | 0.01 |
| Orig. Sum | 100.15 | 100.72 | 100.23 | 100.12 | 100.77 |
| CMI | 0.64 | 0.73 | 0.59 | 0.58 | 0.69 |
| Mg# | 0.911 | 0.912 | 0.906 | 0.912 | 0.904 |
| Ca/Al | 2.34 | 1.91 | 1.28 | 1.54 | 2.33 |
| *Trace element analyses (ppm)* | | | | | |
| *n* = | *4* | *4* | *4* | *4* | *4* |
| Ca | 6300 ±200 | 5613 ±91 | 3739 ±94 | 3812 ±91 | 7994 ±34 |
| Sc | 7.16 ±29 | 5.83 ±10 | 7.47 ±14 | 6.71 ±10 | 7.61 ±9 |
| Ti | 74.5 ±17 | 146 ±2 | 164 ±4 | 112 ±2 | 725 ±8 |
| Cr | 1922 ±10 | 2374 ±40 | 2437 ±11 | 1723 ±13 | 1520 ±13 |
| Mn | 944 ±11 | 962 ±7 | 950 ±9 | 927 ±4 | 986 ±7 |
| Co | 112 ±1 | 118 ±1 | 115 ±1 | 117 ±1 | 116 ±1 |
| Ni | 2086 ±18 | 2343 ±13 | 2064 ±20 | 2240 ±11 | 2139 ±7 |
| Ga | 0.830 ±29 | 1.08 ±4 | 0.702 ±22 | 0.682 ±13 | 1.20 ±6 |
| Sr | 23.2 ±5 | 25.7 ±4 | 5.98 ±14 | 6.64 ±10 | 8.48 ±8 |
| Y | 0.307 ±16 | 1.26 ±4 | 0.200 ±13 | 0.244 ±6 | 1.04 ±4 |
| Zr | 4.38 ±14 | 14.6 ±3 | 1.50 ±3 | 1.40 ±4 | 3.65 ±3 |
| Nb | 0.973 ±43 | 2.74 ±2 | 0.292 ±14 | 0.215 ±7 | 0.192 ±6 |
| Ba | 9.10 ±24 | 8.36 ±10 | 3.14 ±7 | 1.96 ±6 | 2.49 ±5 |
| La | 0.828 ±36 | 3.14 ±5 | 0.229 ±12 | 0.158 ±6 | 0.301 ±8 |
| Ce | 1.31 ±3 | 7.01 ±8 | 0.537 ±12 | 0.363 ±3 | 0.986 ±16 |
| Pr | 0.115 ±8 | 0.746 ±6 | 0.063 ±1 | 0.040 ±2 | 0.157 ±8 |
| Nd | 0.393 ±20 | 2.58 ±5 | 0.268 ±18 | 0.185 ±6 | 0.841 ±45 |
| Sm | 0.060 ±9 | 0.428 ±18 | 0.060 ±5 | 0.041 ±6 | 0.238 ±10 |
| Eu | 0.017 ±2 | 0.118 ±5 | 0.017 ±1 | 0.016 ±1 | 0.073 ±4 |
| Gd | 0.055 ±4 | 0.343 ±22 | 0.051 ±2 | 0.049 ±8 | 0.261 ±8 |
| Tb | 0.011 ±2 | 0.048 ±2 | 0.007 ±1 | 0.007 ±1 | 0.035 ±2 |
| Dy | 0.054 ±3 | 0.243 ±10 | 0.038 ±2 | 0.042 ±3 | 0.217 ±11 |
| Ho | 0.009 ±2 | 0.041 ±2 | 0.007 ±1 | 0.007 ±1 | 0.036 ±1 |
| Er | 0.028 ±4 | 0.118 ±4 | 0.019 ±2 | 0.024 ±2 | 0.099 ±3 |
| Tm | 0.003 ±1 | 0.015 ±2 | 0.002 ±1 | 0.003 ±1 | 0.011 ±1 |
| Yb | 0.029 ±1 | 0.094 ±4 | 0.018 ±2 | 0.024 ±3 | 0.072 ±6 |
| Lu | 0.004 ±1 | 0.013 ±2 | 0.003 ±1 | 0.005 ±1 | 0.010 ±1 |
| Hf | 0.074 ±5 | 0.280 ±9 | 0.036 ±3 | 0.027 ±2 | 0.132 ±7 |
| Ta | 0.045 ±4 | 0.140 ±4 | 0.016 ±2 | 0.013 ±2 | 0.012 ±2 |
| Th | 0.459 ±22 | 0.208 ±4 | 0.027 ±2 | 0.025 ±4 | 0.026 ±2 |
| U | 0.137 ±4 | 0.093 ±1 | 0.015 ±1 | 0.013 ±2 | 0.014 ±2 |
| Ti/Eu | 4461 | 1236 | 9793 | 6953 | 9989 |
| $La/Yb_N$ | 19.24 | 22.39 | 8.69 | 4.43 | 2.84 |
| *Platinum group element analyses (ppb)* | | | | | |
| Os* | | 0.023 | | 3.048 | 3.723 |
| Ir | | 0.200 | | 2.929 | 3.135 |
| Ru | | 3.072 | | 5.934 | 5.513 |
| Pt | | 0.121 | | 0.602 | 3.458 |
| Pd | | 0.426 | | 0.013 | 0.494 |
| Re* | | 0.006 | | 0.009 | 0.035 |
| $\Sigma_{PGE}$ | | 3.8 | | 12.5 | 16.4 |
| $\Sigma_{I\text{-}PGE}$ | | 3.3 | | 11.9 | 12.4 |
| $\Sigma_{P\text{-}PGE}$ | | 0.5 | | 0.6 | 4.0 |
| $Pd/Ir_N$ | | 1.68 | | 0.003 | 0.12 |
| $Pt/Ir_N$ | | 0.31 | | 0.11 | 0.57 |
| $^{187}Os/^{188}Os_{(i)}$* | | 0.12989 | | 0.12169 | 0.12163 |

*Table 6: A comparison of the amount of partial melting in Zealandian mantle residues based on several melting models.*

| Sample | MgO (wt %) | Yb (ppm) | Y (ppm) | $Cr\#_{(spinel)}$ | Modal cpx | $Yb_{Cpx}$ (ppm) | $Dy_{Cpx}$ (ppm) | $F_{(MgO)}$ | $F_{(Yb\ in\ WR)}$ | $F_{(Y\ in\ WR)}$ | $F_{(Cr\#)}$ | $F_{(Yb\ in\ Cpx)}$ | | $F_{(Dy\ in\ Cpx)}$ | |
|---|---|---|---|---|---|---|---|---|---|---|---|---|---|---|---|
| North Island | | | | | | | | | | | | | | | |
| NGB-3 | 46.6 | 0.015 | 0.108 | 0.820 | 7.2 | 0.145 | 0.179 | 28.0 | 26.6 | 23.6 | (22.0) | (28.5) | | (25.0) | |
| NGB-4 | 50.3 | 0.014 | 0.144 | 0.808 | 0.9 | 0.421 | 0.296 | 40.1 | 26.8 | 22.9 | (21.9) | (24.7) | | (24.0) | |
| South Island | | | | | | | | | | | | | | | |
| P43153b | 38.5 | 0.062 | 0.718 | 0.612 | -- | -- | -- | 1.8 | 21.3 | 17.7 | (19.1) | | | | |
| P45280 | 43.1 | 0.037 | 0.313 | 0.614 | -- | -- | -- | 16.8 | 23.5 | 12.0 | (19.1) | | | | |
| MSI33D | 44.7 | 0.060 | 0.795 | -- | 1.9 | -- | -- | 21.7 | 21.5 | 17.1 | -- | | | | |
| MSIK33C | 40.0 | 0.060 | 0.781 | 0.731 | 2.5 | 0.851 | 4.30 | 6.4 | 21.4 | 17.2 | 13.9 | (20.1) | | c.n.p. | |
| *Waitaha domain* | | | | | | | | | | | | | | | |
| MSI20C | 44.0 | 0.021 | 0.362 | 0.437 | 1.3 | 0.386 [0.24] | 0.380 [0.27] | 19.6 | 25.5 | 20.5 | 15.7 | (25.0) | 26.5 | (23.5) | 24.2 |
| MSI20G | 43.0 | 0.038 | 0.593 | 0.463 | 1.4 | 0.382 [0.25] | 0.385 [0.28] | 16.3 | 23.3 | 18.6 | 16.3 | (25.1) | 26.4 | (23.5) | 24.1 |
| MSI79C | 37.7 | 0.287 | 2.255 | 0.128 | 10.8 | 1.86 [1.23] | 2.92 [2.22] | c.n.p. | 8.4 | 9.0 | 3.4 | c.n.p. | 11.5 | (8.1) | 8.7 |
| FvF-1 | 41.0 | 0.180 | 1.50 | 0.126 | 7.5 | 1.61 [1.11] | 2.31 [1.73] | 9.7 | 14.0 | 12.9 | 3.3 | (5.5) | 14.6 | (2.5) | 13.2 |
| WTL-1 | 41.2 | 0.192 | 1.48 | 0.145 | 9.6 | 1.65 [1.05] | 2.24 [1.58] | 10.6 | 13.3 | 13.0 | 4.7 | (4.6) | 15.2 | (8.6) | 14.4 |
| WTL-2 | 43.5 | 0.069 | 1.31 | 0.232 | 4.8 | 1.01 [0.65] | 1.20 [0.85] | 17.9 | 20.8 | 13.9 | 9.4 | (17.5) | 22.4 | (17.6) | 20.4 |
| WTL-3 | 42.1 | 0.194 | 1.49 | 0.134 | 9.4 | 1.72 [1.24] | 2.39 [1.79] | 13.4 | 13.2 | 12.9 | 3.9 | (2.9) | 13.0 | (7.3) | 12.8 |
| OU45852 | 42.1 | 0.214 | 1.71 | 0.126 | 10.7 | 1.90 [1.40] | 2.61 [2.01] | 13.2 | 12.1 | 11.7 | 3.3 | c.n.p. | 9.6 | (5.3) | 10.8 |
| WRR-1 | 44.3 | 0.100 | 0.921 | 0.198 | 6.9 | 0.818 [0.60] | 0.587 [0.44] | 20.5 | 18.7 | 16.3 | 7.8 | (20.6) | 23.8 | (22.4) | 23.3 |
| WRR-3 | 42.7 | n.m. | n.m. | 0.177 | 9.1 | 1.25 [0.92] | 1.58 [1.18] | 15.3 | | | 6.7 | (13.0) | 19.0 | (14.4) | 17.8 |
| WRR-5 | 45.9 | 0.016 | 0.124 | 0.407 | 4.4 | 0.261 [0.19] | 0.480 [0.36] | 25.8 | 26.4 | 23.3 | 15.0 | (26.5) | 27.5 | (23.1) | 23.7 |
| WRR-6 | 44.0 | n.m. | n.m. | 0.730 | 12.6 | -- | -- | 19.5 | | | (20.9) | | | | |
| WRR-7 | 45.4 | 0.065 | 0.488 | 0.283 | 4.6 | 0.934 [0.66] | 1.33 [0.97] | 24.1 | 21.1 | 19.4 | 11.4 | (18.8) | 23.0 | (16.5) | 19.5 |
| WRR-9 | 44.3 | 0.111 | 0.954 | 0.631 | 5.6 | -- | -- | 20.6 | 18.0 | 16.1 | (19.4) | | | | |
| DPP-1 | -- | 0.702 | 7.92 | 0.111 | 18 | 1.91 [1.56] | 3.08 [2.53] | c.n.p. | | | 2.0 | c.n.p. | 6.5 | (1.1) | 6.1 |
| DPP-2 | -- | 0.130 | 2.32 | 0.473 | 4 | 0.410 [0.32] | 0.888 [0.22] | c.n.p. | 16.8 | 8.7 | 16.5 | (24.8) | 25.7 | (20.1) | 21.7 |
| DPP-3 | 38.6 | 0.393 | 4.34 | 0.109 | 17.0 | 2.09 [1.59] | 3.59 [2.89] | 1.9 | 3.4 | 0.1 | 1.9 | c.n.p. | 4.4 | c.n.p. | 3.0 |
| DPP-5 | -- | 0.526 | 5.92 | 0.109 | 16 | 1.87 [1.50] | 3.20 [2.60] | c.n.p. | | | 1.8 | c.n.p. | 7.8 | c.n.p. | 5.4 |
| DPP-6 | 35.5 | 0.412 | 4.06 | 0.161 | 11.3 | 1.95 [1.38] | 3.64 [2.88] | c.n.p. | 2.5 | 1.2 | 5.7 | c.n.p. | 8.3 | c.n.p. | 2.8 |
| WFP-1 | 46.1 | 0.031 | 0.120 | 0.303 | 3.0 | 0.412 [0.27] | 0.229 [0.16] | 26.4 | 24.1 | 23.4 | 12.1 | (24.8) | 26.1 | (24.5) | 25.2 |
| WFP-2 | 42.9 | 0.134 | 1.14 | 0.174 | 7.3 | 1.44 [1.02] | 2.22 [1.65] | 15.9 | 16.3 | 14.9 | 6.5 | (9.2) | 16.2 | (8.8) | 14.8 |
| WFP-4 | 46.3 | 0.024 | 0.140 | 0.430 | 2.1 | 0.229 [0.15] | 0.179 [0.12] | 26.9 | 24.9 | 23.0 | 15.6 | (27.0) | 28.2 | (25.0) | 25.7 |
| WFP-5 | 46.0 | 0.017 | 0.102 | 0.358 | 2.9 | 0.267 [0.17] | 0.393 [0.27] | 26.1 | 26.1 | 23.7 | 13.7 | (26.4) | 27.8 | (23.5) | 24.3 |
| WFP-7 | 44.8 | n.m. | n.m. | 0.279 | 4.9 | 0.691 [0.48] | 0.720 [0.52] | 22.3 | | | 11.2 | (22.4) | 23.9 | (21.4) | 22.8 |
| WFP-8 | 42.3 | 0.090 | 0.456 | 0.205 | 8.4 | 0.748 [0.54] | 0.596 [0.44] | 14.1 | 19.3 | 19.7 | 8.1 | (21.7) | 23.5 | (22.4) | 23.3 |
| WFP-11 | 47.0 | 0.010 | 0.108 | 0.449 | 1.6 | 0.140 [0.09] | 0.504 [0.36] | 29.2 | 27.8 | 23.6 | 16.0 | (28.8) | 29.7 | (22.9) | 23.6 |
| Chatham Islands | | | | | | | | | | | | | | | |
| P80180 | 45.8 | 0.130 | 1.67 | 0.568 | 3.3 | 2.12 | 8.00 | 25.5 | 16.9 | 11.9 | 18.3 | c.n.p. | | c.n.p. | |
| P80290 | 45.6 | 0.029 | 0.307 | 0.529 | 3.7 | 0.182 [0.12] | 0.643 [0.45] | 24.8 | 24.3 | 21.1 | 17.6 | (27.8) | 28.8 | (22.0) | 23.1 |
| P80291 | 46.7 | 0.094 | 1.29 | 0.569 | 3.5 | 1.98 | 6.72 | 28.3 | 19.1 | 14.2 | 18.4 | c.n.p. | | c.n.p. | |
| P80354a | 45.8 | 0.018 | 0.200 | 0.532 | 1.9 | 0.196 [0.12] | 0.673 [0.46] | 25.3 | 26.0 | 22.2 | 17.7 | (27.0) | 28.8 | (21.8) | 23.1 |
| P80354b | 46.8 | 0.024 | 0.244 | 0.431 | 2.1 | 0.471 [0.30] | 1.29 [0.90] | 28.6 | 25.0 | 21.7 | 15.6 | (24.3) | 25.6 | (16.8) | 20.0 |
| P80354c | 45.2 | 0.072 | 1.04 | 0.420 | 5.1 | 1.03 [0.69] | 3.88 [2.76] | 23.3 | 20.6 | 15.5 | 15.3 | (17.1) | 21.9 | c.n.p. | 4.1 |

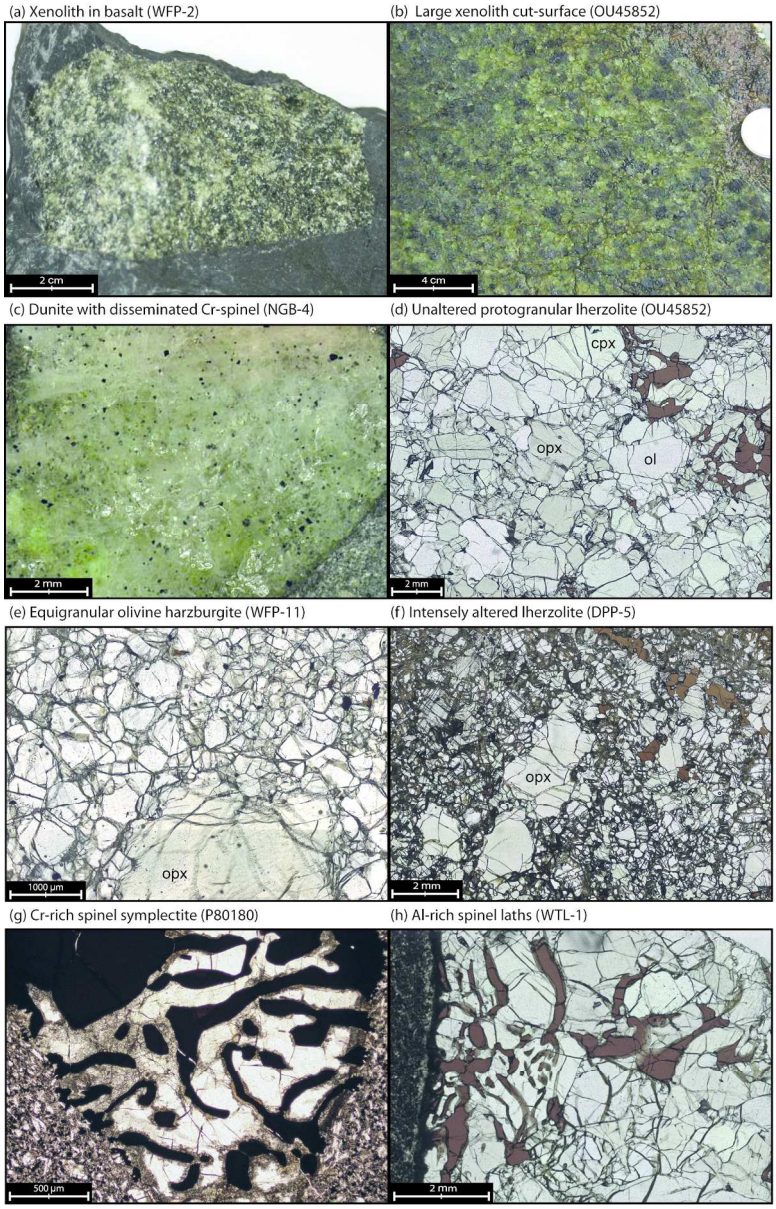


137x214mm (300 x 300 DPI)

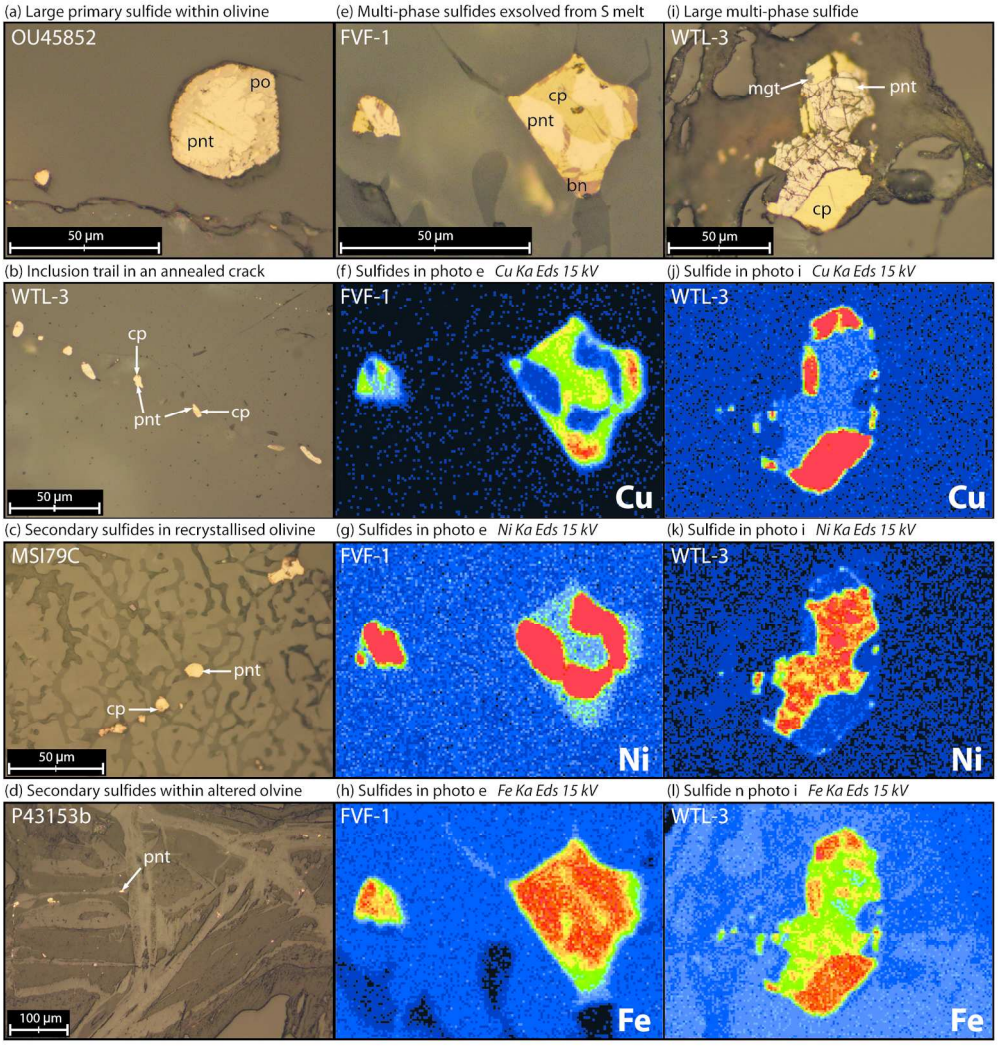


169x178mm (300 x 300 DPI)

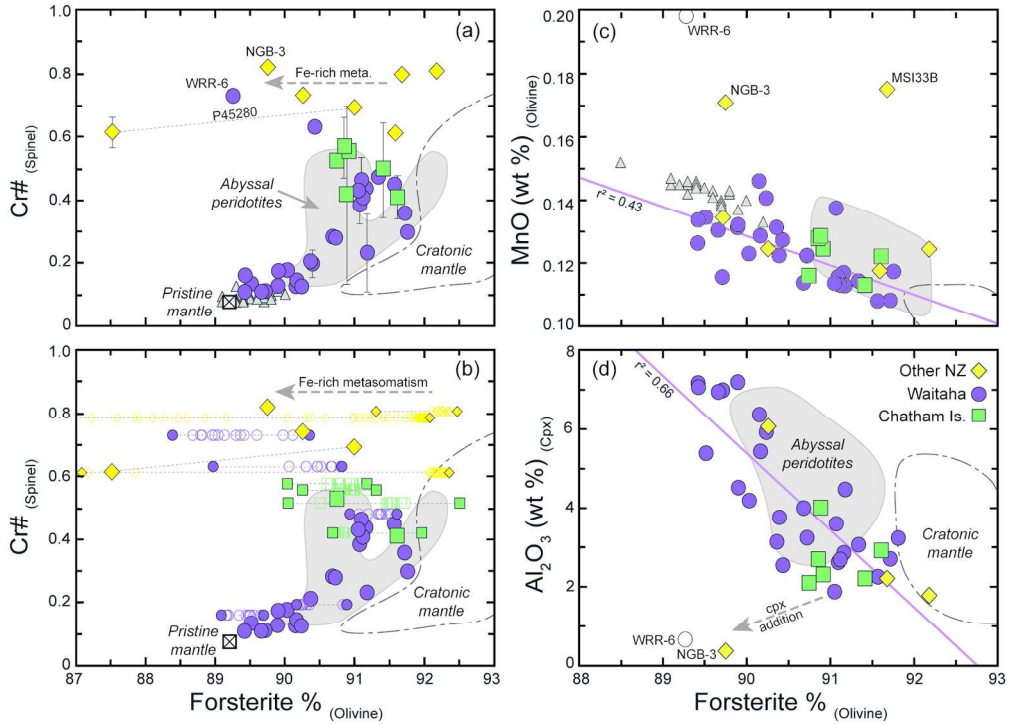


161x116mm (300 x 300 DPI)

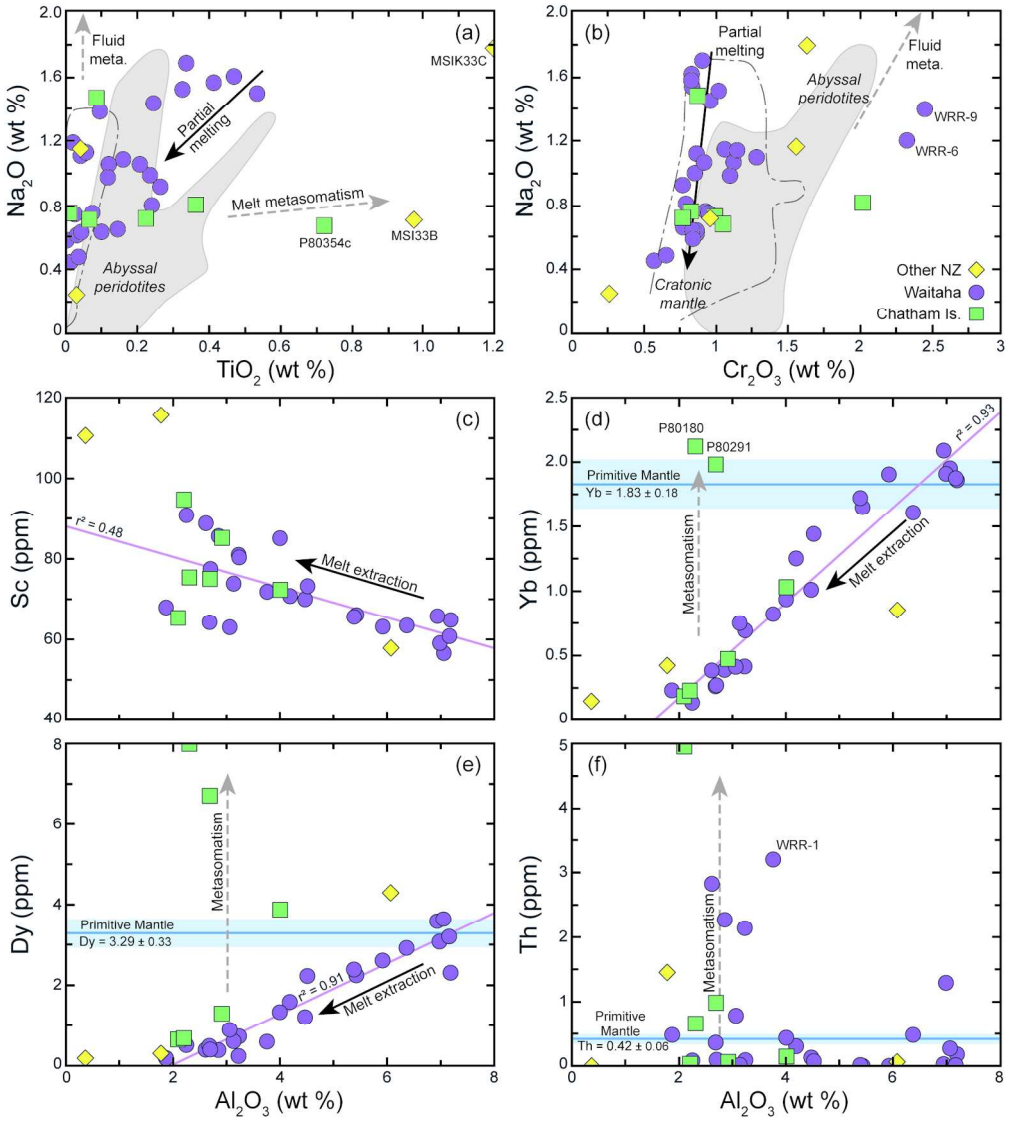


161x180mm (300 x 300 DPI)

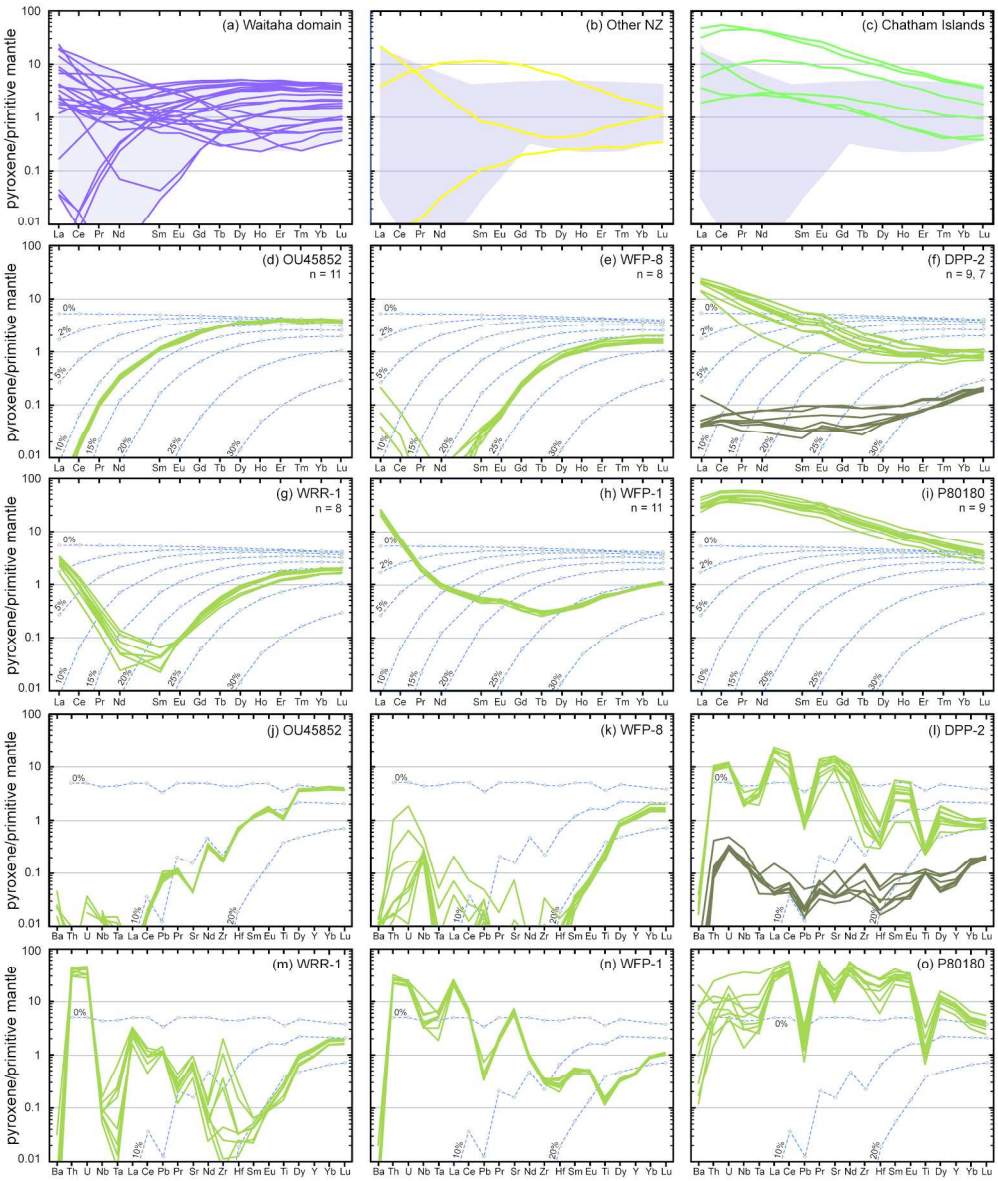


199x234mm (300 x 300 DPI)

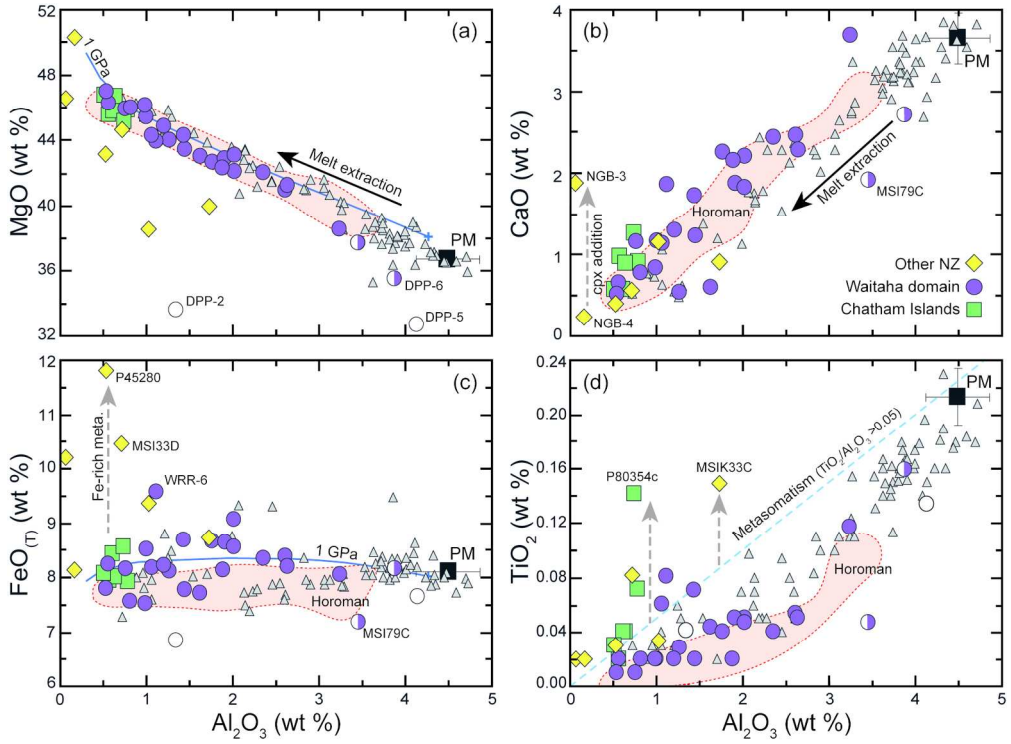


161x119mm (300 x 300 DPI)

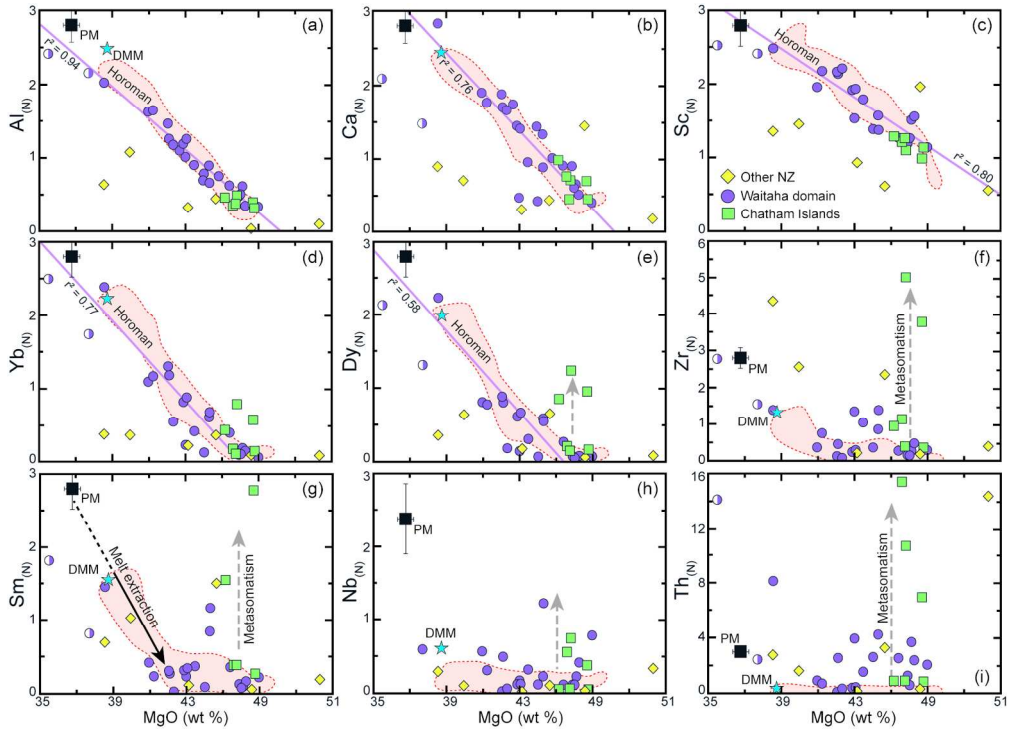


163x118mm (300 x 300 DPI)

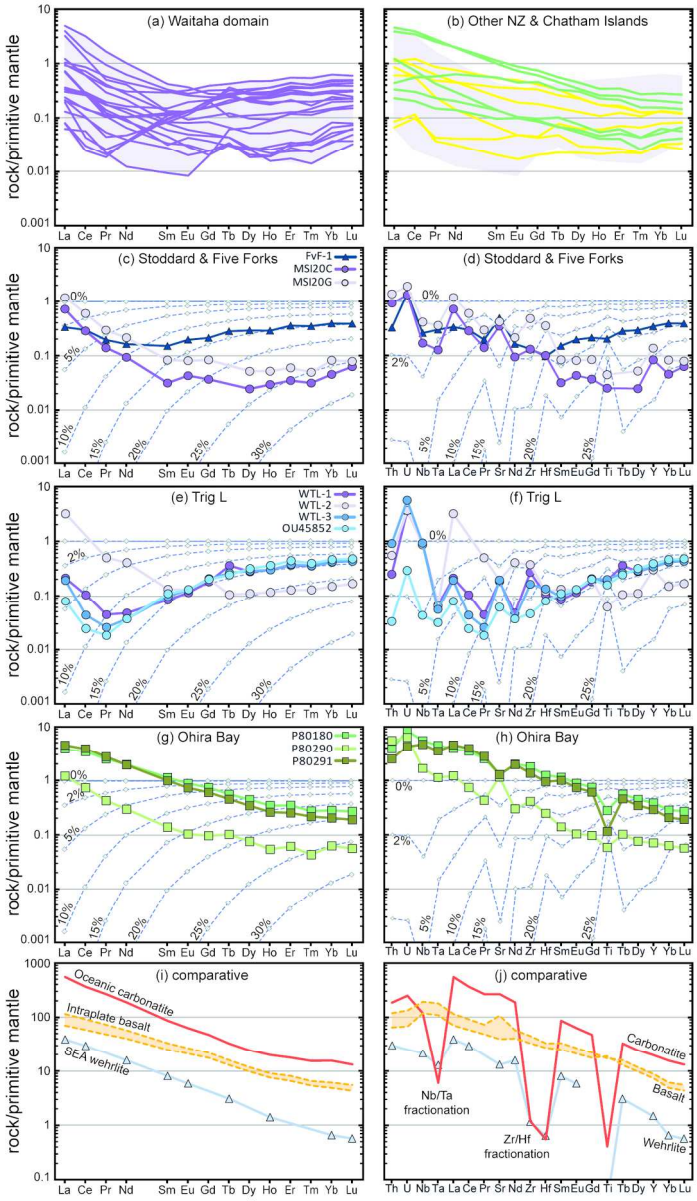


123x211mm (300 x 300 DPI)

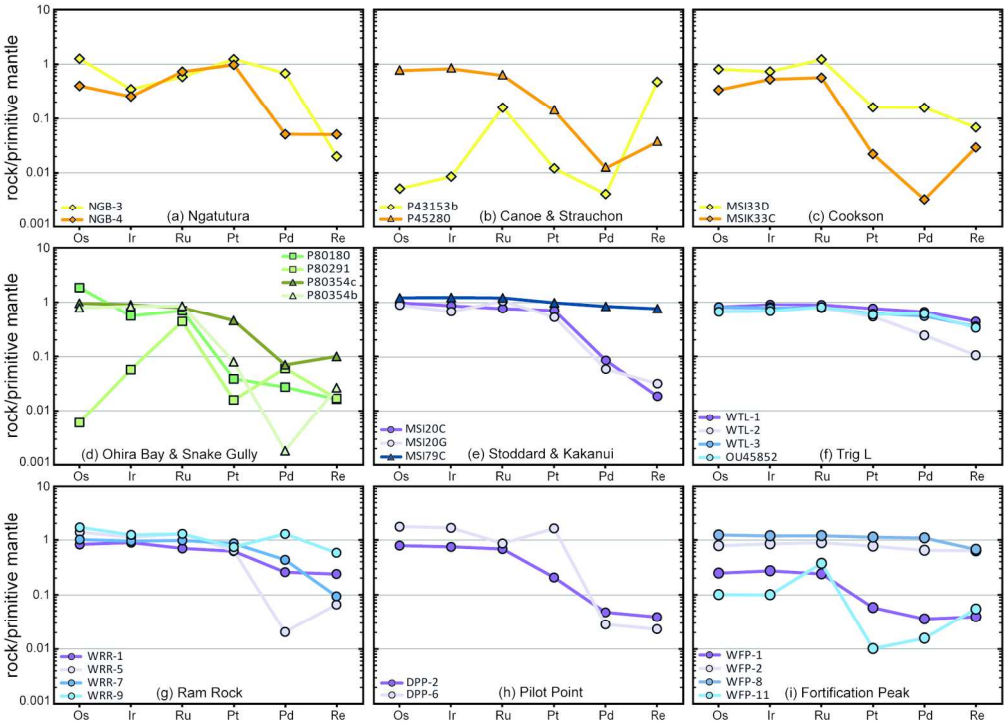


168x121mm (300 x 300 DPI)

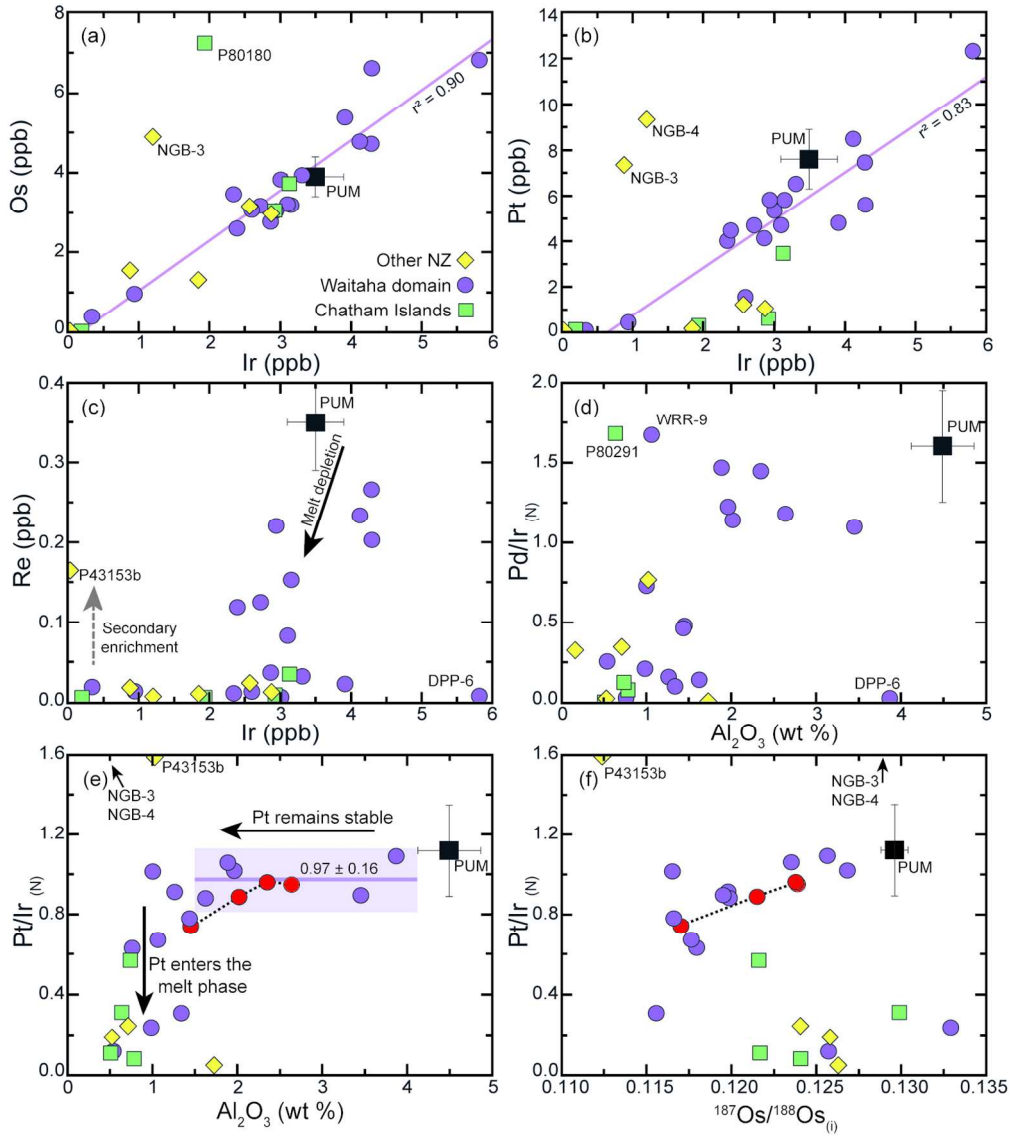


135x153mm (300 x 300 DPI)

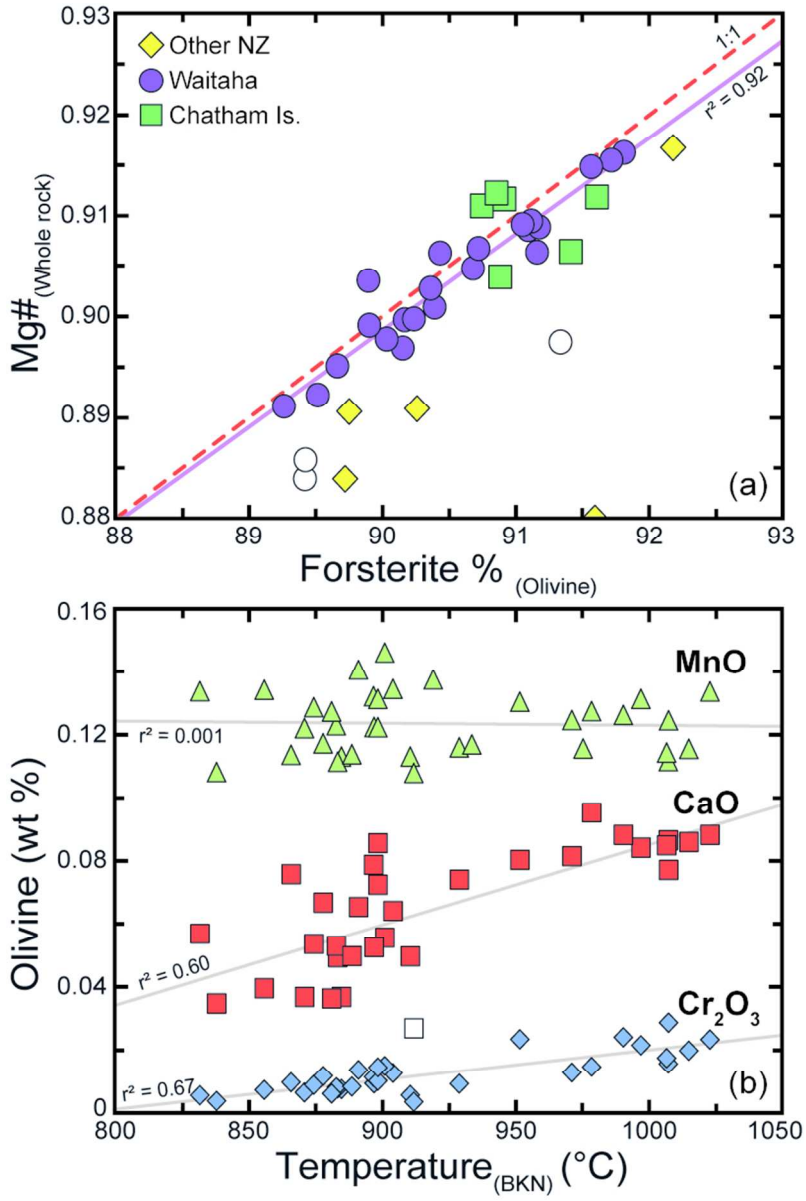


68x103mm (300 x 300 DPI)

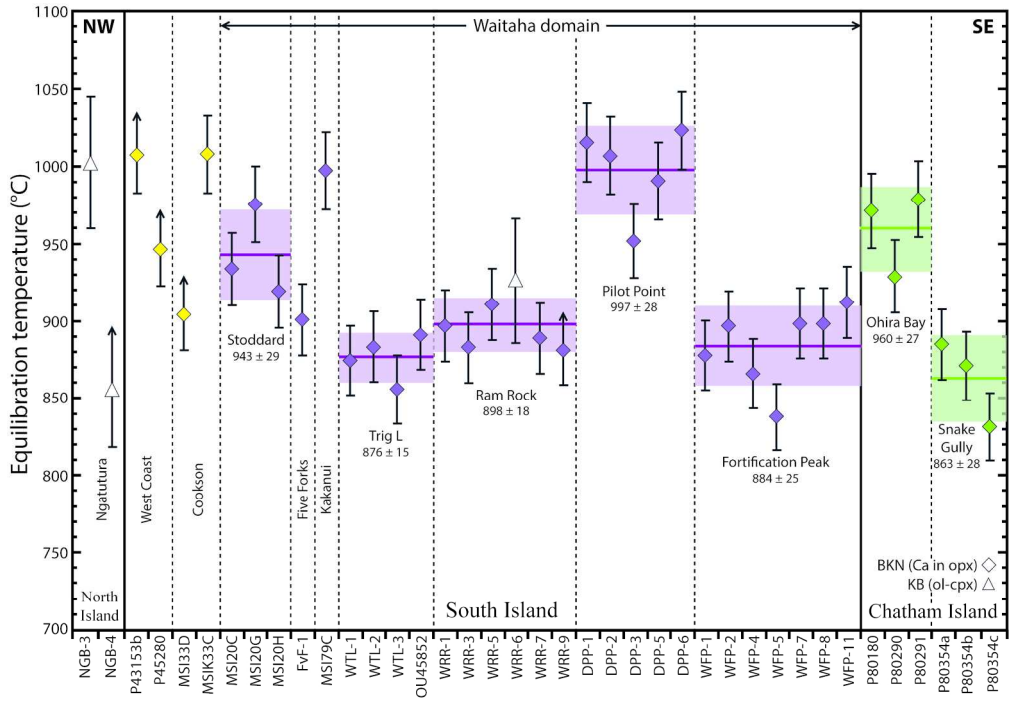


189x131mm (300 x 300 DPI)

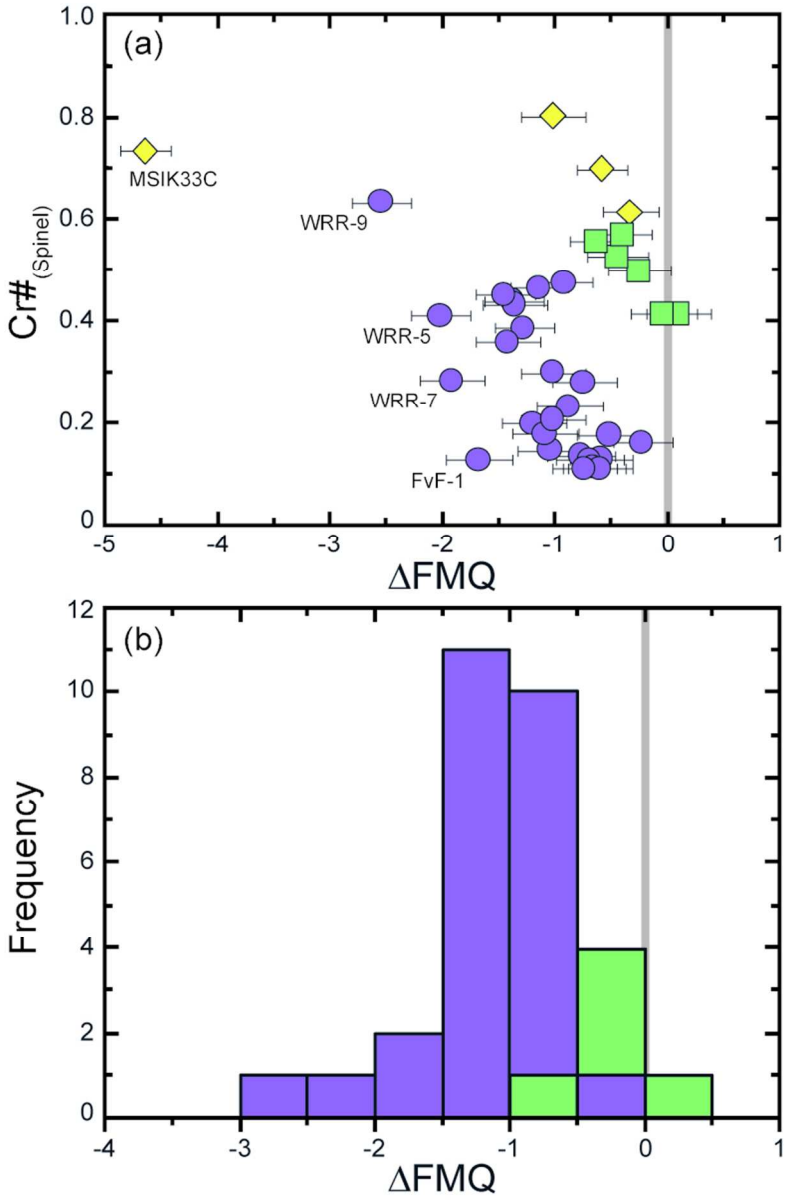


66x102mm (300 x 300 DPI)

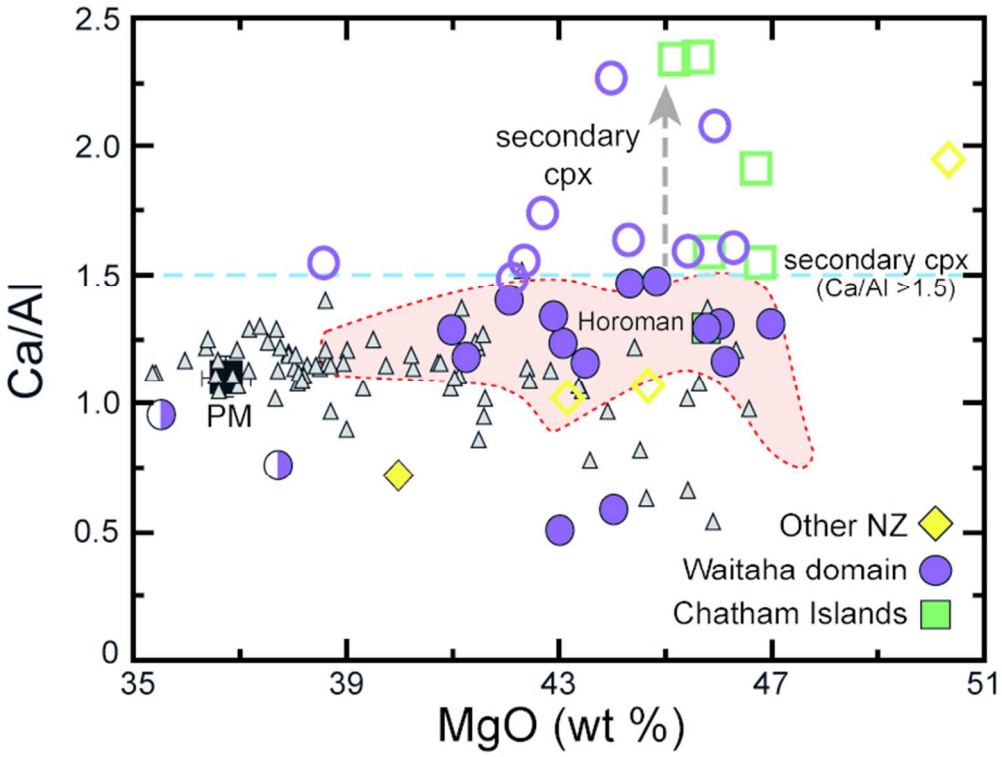


67x50mm (300 x 300 DPI)

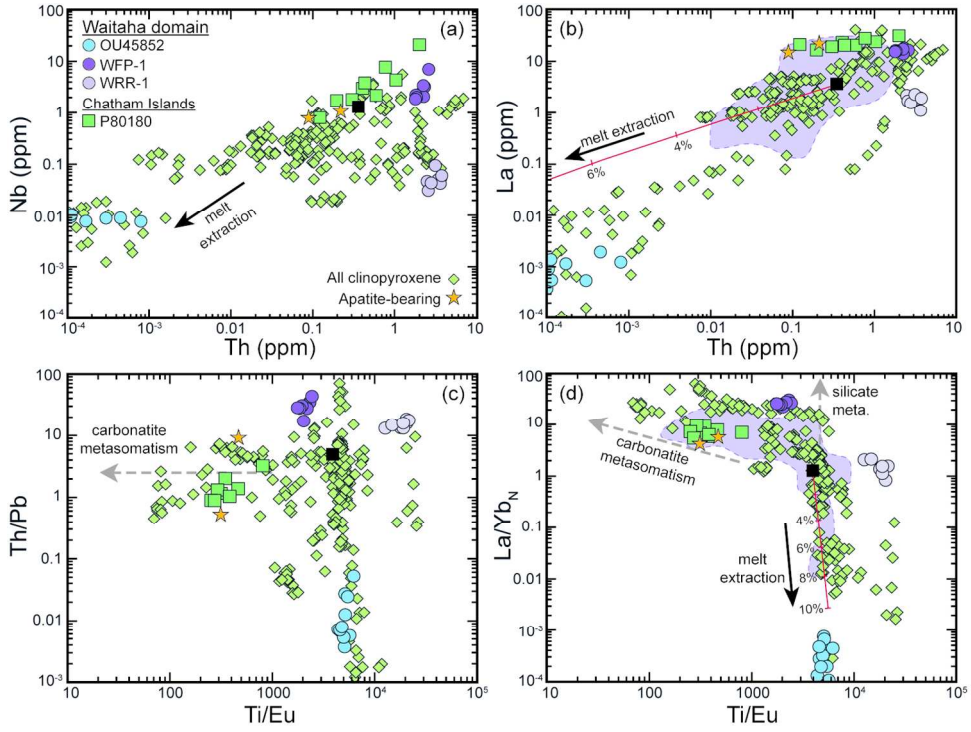


140x102mm (300 x 300 DPI)

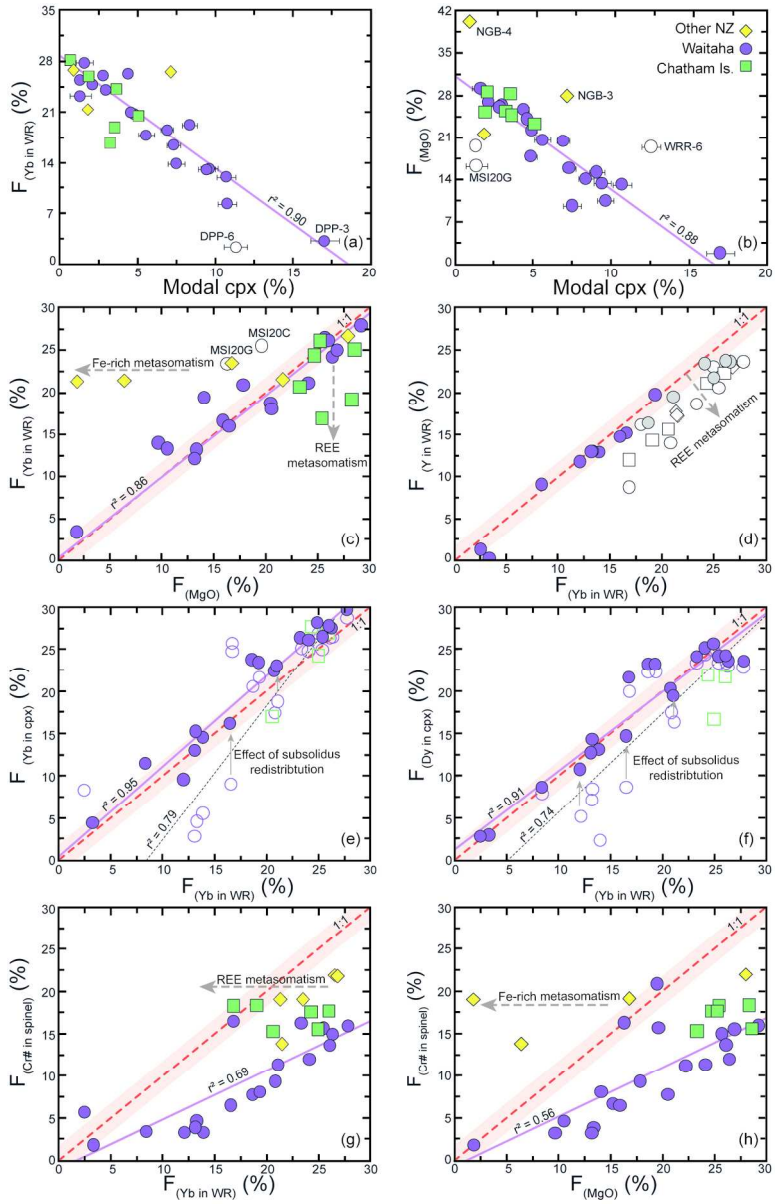


134x205mm (300 x 300 DPI)

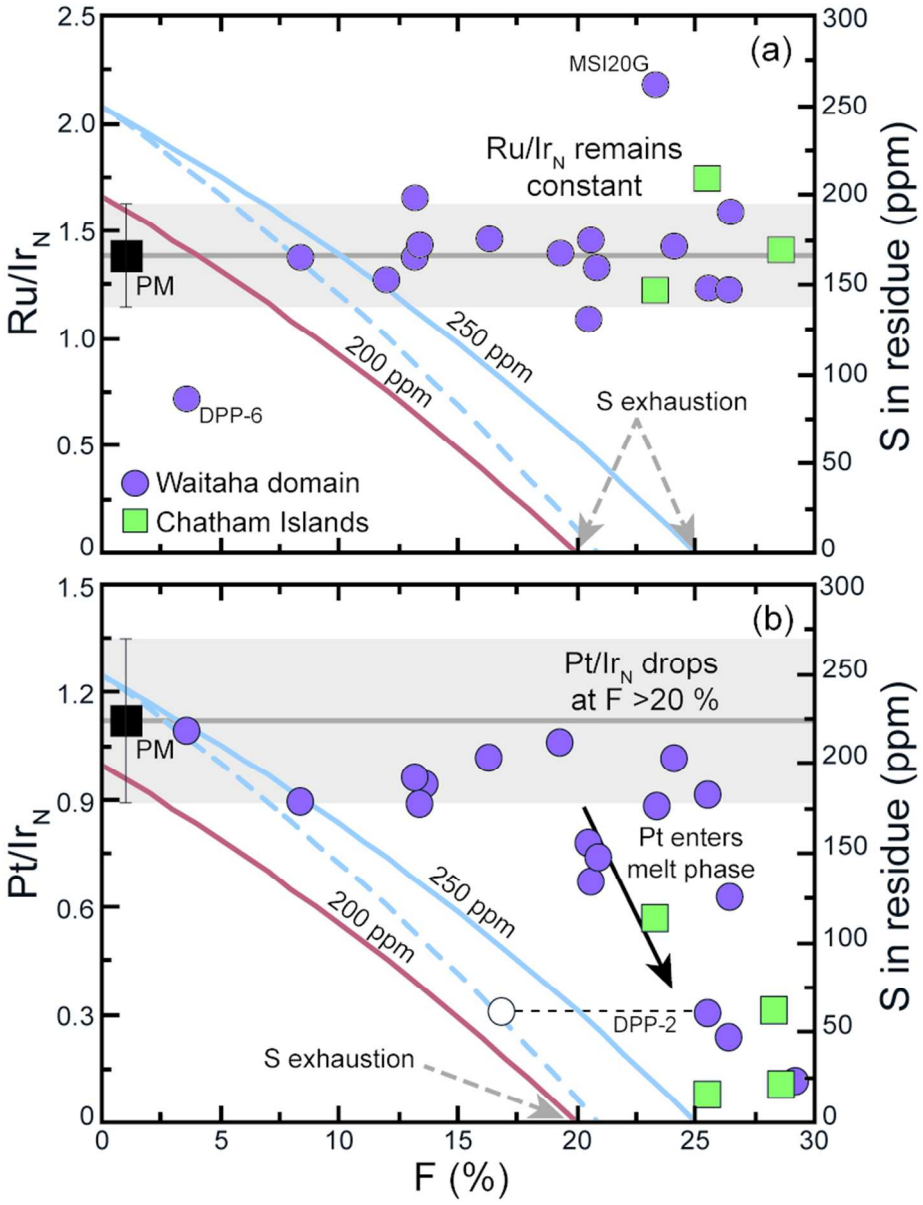


74x96mm (300 x 300 DPI)

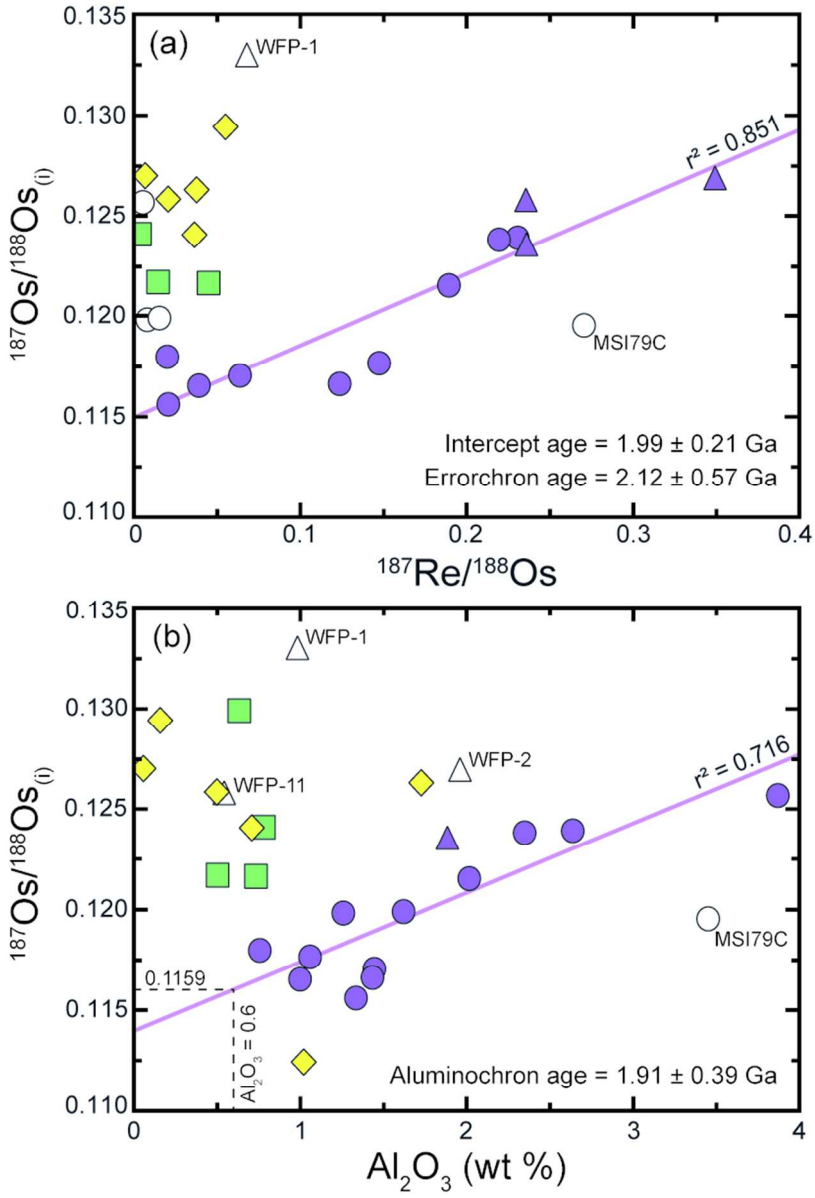


70x103mm (300 x 300 DPI)